Emission Spectroscopy of Wall Surface Temperature and Impurity Ion Flow in Tokamak Edge Plasmas

Nao Yoneda

Contents

1 Introduction 1
1.1 Background 1
1.2 Research Objectives 6
1.3 Outline of the Thesis 9
2 Emission Processes of Impurity Ions and Hydrogen Molecules in Edge Plasmas 10
2.1 Radiometric Quantities and Units 10
2.2 Energy Levels of C^{2+} Ions and Hydrogen Molecules 12
2.3 Collisional-Radiative Processes of C^{2+} Ions and Hydrogen Molecules 14
2.4 Coronal Model 17
3 Modeling of Increase in Rotational Temperature of Hydrogen Molecules Near Plasma-Facing Walls 18
3.1 Surface Thermometry of Plasma-Facing Walls 18
3.2 Translational, Vibrational, and Rotational Temperatures and Emission Spectrum of Hydrogen Molecules 21
3.3 Rotational Temperature of Hydrogen Molecules Near Plasma-Facing Walls 23
3.4 Modeling of Collisional Increase in Rotational Temperature of Hydrogen Molecules in Edge Plasma 24
3.4.1 Collisional-Radiative Processes Affecting Rotational Temperature 24
3.4.2 Evaluation of Spatial Distribution of Rotational Temperature 25
3.4.3 Code Benchmark 33
3.4.4 Calculation Results of Collisional Increase in Rotational Temperature 35
3.5 Conclusion 37
4 Thermometry of Plasma-Facing Surface using Rotational Temperature of Hydrogen Molecules 38
4.1 Experimental Setup 38
4.1.1 Experimental Devices 38
4.1.2 Plasma Discharges 41
4.1.3 Spectroscopic System 46
4.2 Experimental Results 48
4.2.1 Fulcher-α Band Emission Spectra of Hydrogen Molecule 48
4.2.2 Evaluation of Rotational Temperature 51
4.2.3 Estimation of Plasma-Facing Surface Temperature 59
4.3 Conclusion 66
5 Flow Measurement of Impurity Ions in Edge Plasmas using Emission Spectroscopy with Multiple

Viewing Chords 67
5.1 Ion Flow in Edge Plasmas 67
5.2 Spectral Profiles of Emission Lines 69
5.3 Experimental Setup 71
5.3.1 Experimental Simulation of Edge Plasmas using Three Types of Magnetic Configuration 71
5.3.2 Spectroscopic System with Multiple Viewing Chords 75
5.4 Inversion Method 78
5.4.1 Chord Integral of Spectra 80
5.4.2 Abel Inversion 81
5.4.3 Shell Model 82
5.4.4 Verification of the Inversion Methods using Model Data 84
5.5 Results 86
5.6 Conclusion 91
6 Conclusion 92
Reference 94
List of Publication 98

Acknowledgements

I am grateful to Prof. Masahiro Hasuo, Associate Prof. Taiichi Shikama, Lecturer Arseniy Kuzmin, and Assistant Prof. Keisuke Fujii for their encouragement and discussions. I would like to thank the members and graduates of Optical Engineering Laboratory for giving me fulfilling life there.

For the study in QUEST, I would like to thank the following members of Research Institute for Applied Mechanics, Kyushu University: Prof. Kazuaki Hanada, Prof. Hiroshi Idei, Prof. Takeshi Ido, Assistant Prof. Takumi Onchi, Dr. Kengoh Kuroda, and Ms. Kaori Kono. I also appreciate the support by the staff and students of the QUEST group, and the spare time spent with them. I am also thankful to Prof. Akira Ejiri of the University of Tokyo and students and graduates of his group for providing Thomson scattering data.

For the study in LTX-β, I am grateful to Dr. Filippo Scotti of Laurence Livermore National Laboratory (LLNL) for his encouragement, discussions, careful reading of my thesis, and support for my stay in Princeton. I would like to thank the following members working at the Princeton Plasma Physics Laboratory (PPPL): Dr. Dick Majeski, Dr. Masayuki Ono, Dr. Ron Bell, Dr. Anurag Maan, Dr. Dennis Boyle, Dr. Paul Hughes, Dr. Shota Abe, Dr. Shigeyuki Kubota, and Dr. Priya Sinha. The study is partly supported by Japan / U. S. Cooperation in Fusion Research and Development FP2-4 (National Institute for Fusion Science), and USDoE contracts DE-AC52-07NA27344 (LLNL) and DE-AC02-09CH11466 (Princeton University).

For the study in DIII-D, I thank Dr. Filippo Scotti for his suggestion of the collaboration and Dr. Adam McLean of LLNL and Prof. Mathias Groth of Aalto University for their discussions and for providing data.

I am grateful for the establishment of the scholarship and the financial support by Mori Manufacturing Research and Technology Foundation.

Lastly, I thank my family for their understanding and encouragement during my doctoral course.

1 Introduction

1.1 Background

Fossil fuels, such as coal, oil, and natural gas, are the world's largest energy sources, and more than 60% of the world's electricity is generated from them [1]. However, fossil fuels will run out in the near future, and reducing CO_2 emission is an urgent global requirement to reduce the impact on climate change [2]. Nuclear fusion power generation is being studied owing to its potential as a virtually limitless and CO_2-emission-free energy source [3].

Nuclear fusion is a nuclear reaction where two nuclei combine to form a heavier nucleus. One of the fusion reactions being considered for energy generation is that of deuteron and triton, the so-called DT reaction:

$$^{2}\mathrm{D} + {}^{3}\mathrm{T} \rightarrow {}^{4}\mathrm{He}\ (3.5\ \mathrm{MeV}) + \mathrm{n}\ (14.1\ \mathrm{MeV}). \qquad (1\text{-}1)$$

The DT reaction generates a helium nucleus and a neutron with a total kinetic energy of 17.6 MeV, and the energy is utilized to generate electricity. The reaction produces no CO_2 emission and the fuel is abundant: deuterium is available from seawater and tritium can be bred from naturally abundant lithium [4].

Magnetic confinement fusion is one of the methods under consideration to realize economically feasible power plants exploiting nuclear fusion. For magnetic confinement fusion, a deuterium and tritium mixed plasma is confined by a magnetic field and heated to increase the thermal motion and reaction rate. The tokamak is one of the leading configurations under consideration for magnetically confined fusion. ITER (International Thermonuclear Experimental Reactor) shown in Fig. 1-1 [5] is an example of a tokamak used for the study of magnetic confinement fusion. It is currently under construction in France under the international cooperation to achieve first plasma in 2025 [3]. The main components of ITER include the vacuum vessel, first wall, blanket, divertor, and three types of coil: toroidal field, poloidal field, and central solenoid coils. The plasma is generated inside the vacuum vessel and confined by the magnetic field. The vacuum vessel is covered with the first wall and divertor. The blanket is used to breed tritium from lithium and to convert the fusion

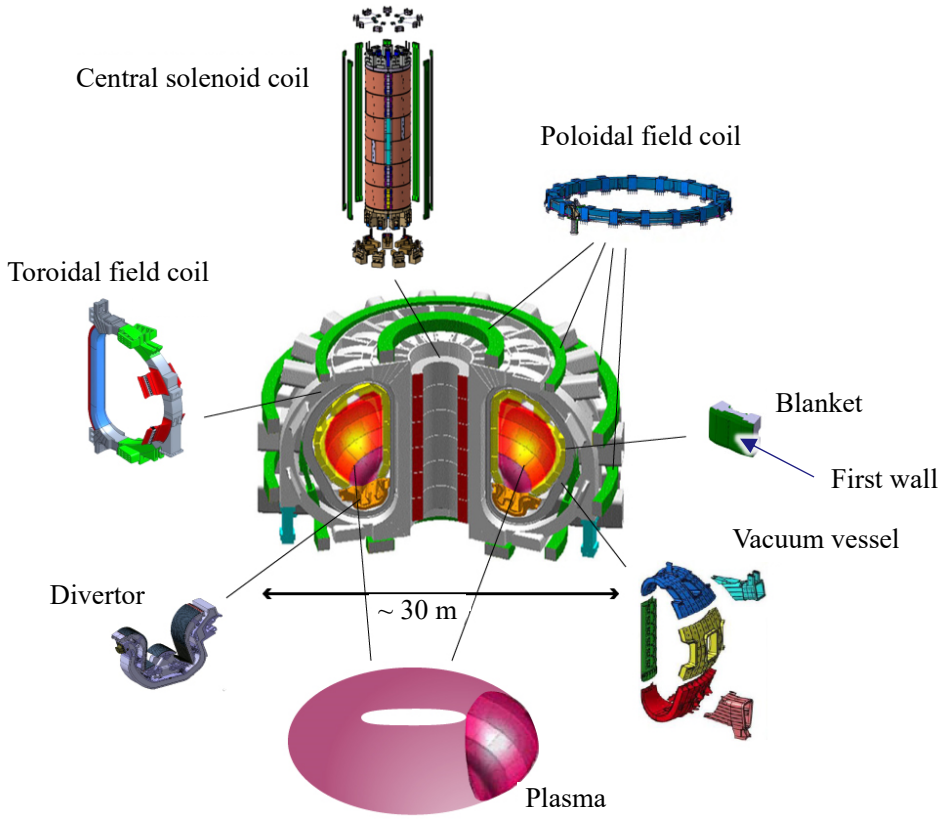

Fig. 1-1. Schematic illustration of ITER and its components [5].

energy into heat energy via neutron capture, and the divertor is used to control particles and the plasma–material interaction.

A torus plasma is confined in a tokamak. Fig. 1-2 shows a schematic illustration of the confined plasma. A cylindrical coordinate system (R, φ, z) is introduced to match the z-axis with the axis of symmetry. Cross sections parallel to the $R\varphi$-plane and Rz-plane are called toroidal and poloidal cross sections, respectively, as shown in Fig. 1-2. The direction of the φ-axis and the circumferential direction of the poloidal cross section are called the toroidal and poloidal directions, respectively. The circle consisting of the center of the poloidal cross section is called the magnetic axis, and the major radius is defined as its radius. The minor radius is defined as the radius from the magnetic axis in the poloidal cross section. Note that the ratio of the major to minor radii is defined as the aspect ratio and a tokamak with a small aspect ratio of ~1 is called a spherical tokamak. The plasma in a tokamak is confined by toroidal and poloidal magnetic fields. The toroidal field coils generate the toroidal field, and the central solenoid coil drives an electric current in the toroidal direction called the

plasma current, which generates the poloidal field. The poloidal field coils are used to shape the plasma. The surface consisting of magnetic field lines is called the magnetic flux surface.

A divertor configuration is the magnetic configuration that will be employed in ITER. The poloidal cross section of a tokamak plasma in the divertor configuration is shown in Fig. 1-3(a). Gray lines show magnetic flux surfaces, and the thick line represents the last closed flux surface (LCFS), which is the outermost closed surface. A null in the poloidal magnetic field (X-point) is generated to divert the location of the plasma–material interaction away from the confined plasma. The LCFS passes through the X-point and is also called the separatrix. Core and edge plasmas are defined as the plasmas on the inside and outside of the separatrix, respectively. Typical plasma parameters in ITER are shown in Fig. 1-3(a). In the core plasma, the electron density $n_e \approx 10^{20}$ m^{-3} and the electron temperature $T_e \approx 10$ keV are expected values for the plasma parameters [6]. For the edge plasma, three characteristic regions are shown by purple boxes in Fig. 1-3(a): (i) scrape-off layer (SOL), (ii) X-point, and (iii) divertor leg. Electron density and temperature are $\approx 10^{19}$ m^{-3} and ≈ 0.1 keV for the (i) SOL [7], and 10^{20}–10^{21} m^{-3} and < 30 eV for (iii) divertor leg [8], respectively. The SOL and divertor leg shown by purple boxes are respectively denoted as the "outer" SOL and divertor leg to distinguish them from the "inner" ones, which are on the side closer to the axis of symmetry of the

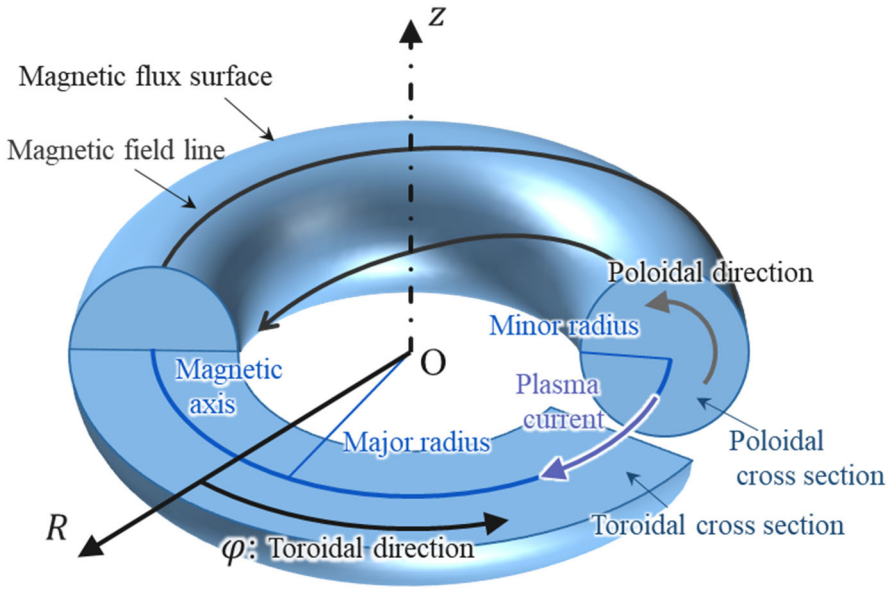

Fig. 1-2. Schematic illustration of a tokamak plasma. A cylindrical coordinate system (R, φ, z) is introduced to match the z-axis with the axis of symmetry.

plasma. Inboard and outboard sides are also respectively defined as the sides closer to and farther from the axis of symmetry.

The divertor and first wall are the components directly facing and receiving energy from the plasma. The divertor in ITER is schematically illustrated in Fig. 1-3(c) [9]. It consists of three plasma-facing components (inner vertical target, outer vertical target, and dome) and a cassette body made of stainless steel to house them. The vertical targets consist of tungsten monoblocks and CuCrZr cooling tubes to cool the plasma-facing components and are designed to handle steady heat flux of up to 10 MW m^{-2} [10]. The dome consists of tungsten tiles bonded to a CuCrZr heat sink with hypervapotron cooling and the tiles are designed to handle steady heat flux of up to 5 MW m^{-2} [11]. The first wall in ITER is made of a copper alloy and stainless steel and covered with beryllium tiles [12]. The inner and outer strike points are the locations where the separatrix intersects the inner and outer targets, respectively. Heat and particle fluxes from the core plasma concentrate at strike points, and Fig. 1-3(d) shows the calculated surface temperature variation along the outer vertical target of ITER [13].

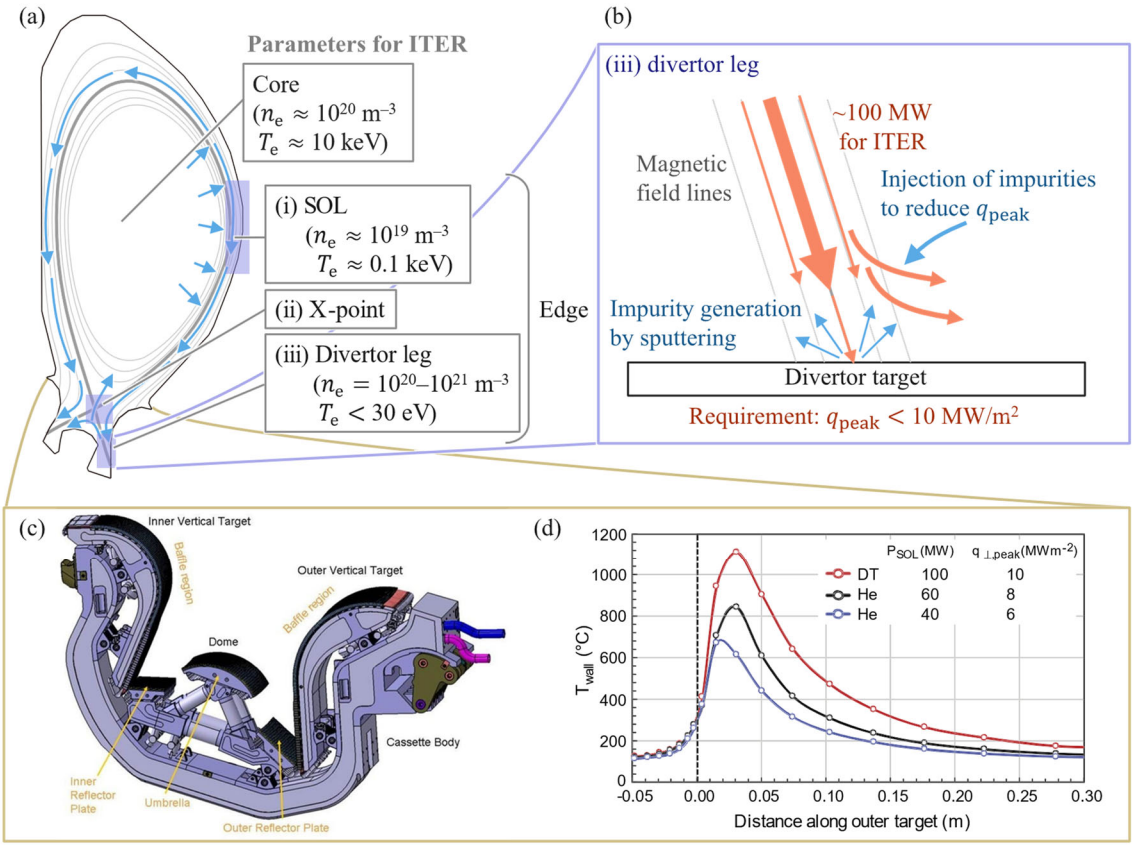

Fig. 1-3. (a) Electron density n_e and temperature T_e in core and edge plasmas of ITER [6, 7, 8] and schematic of impurity transport pathways. Purple boxes show characteristic regions of edge plasma: (i) SOL, (ii) X-point, (iii) divertor leg. Blue arrows indicate the flows in the tokamak projected on the poloidal cross section. (b) Impurity generation at the divertor target. Orange and blue arrows show the heat and particle fluxes, respectively. (c) Schematic illustration of divertor [9]. Inner and outer targets are armored by monoblocks of tungsten and receive heat and particles transported along the magnetic field. (d) Variation of calculated surface temperature T_{wall} along the outer target of ITER made of tungsten [13].

1.2 Research Objectives

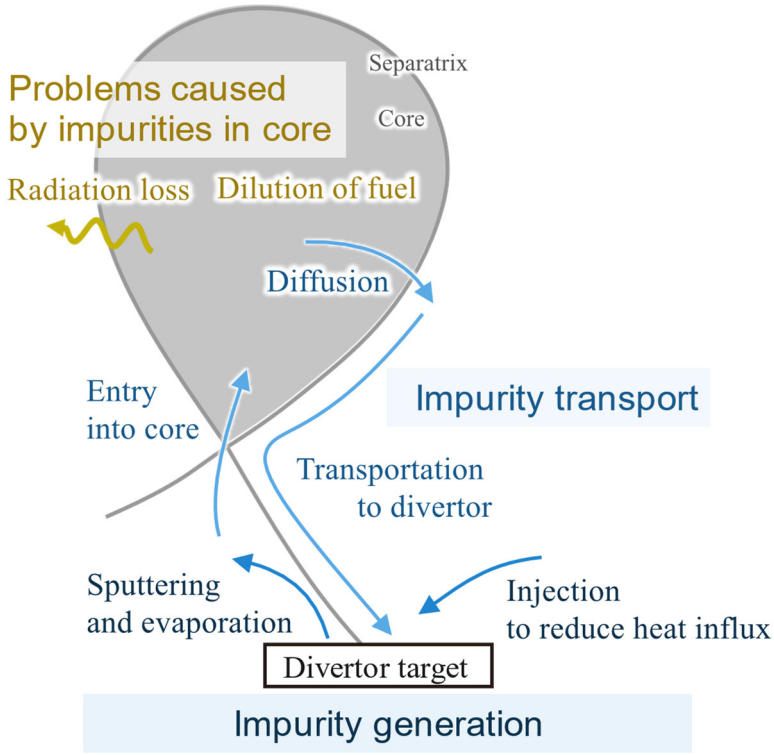

Fig. 1-4. Impurity generation and transport in a tokamak. Gray line shows the separatrix and shaded area shows the core plasma. Blue arrows indicate the impurity flow direction.

Impurities are generated by sputtering and intentional injection to reduce the peak heat flux on the divertor targets. Particles confined in the core plasma diffuse and are transported to the divertor along the magnetic field lines as shown in Fig. 1-4. The transported heat and particle fluxes impinging onto the divertor can result in the heating and sputtering of plasma-facing component materials and the generation of impurities (see Fig. 1-3(b)). In ITER, the power loads to the targets are expected to be ~100 MW [14]. The peak heat flux q_{peak} on the outer target can exceed the maximum heat flux allowed by the target of 10 MW m^{-2}; for the power exhaust to the SOL of 100 MW, q_{peak} is estimated as 15.4 MW m^{-2}, which results in the surface temperature increasing to 1900 K [8]. Impurity gas as such as neon and argon can be injected to exhaust heat by bremsstrahlung and spontaneous emission and reduce q_{peak} on the targets.

The generated impurities enter the core plasma, diffuse, and are transported around the

device through the edge plasma. They move along the magnetic field lines in the core plasma and are transported across the magnetic flux surfaces by the balance of diffusion and convection forces. The radial impurity ion fluxes to the edge plasma are largest at the outboard midplane owing to a local increase in the diffusion coefficient and the existence of non-diffusive transport [15]. This produces ion pressure gradients along the magnetic field lines from the outboard midplane to the inner and outer divertor targets in the edge plasma, and bifurcated ion flows are driven by the pressure gradient along the magnetic field lines. The ion flow perpendicular to the magnetic field is also driven by ion drift, but its velocity is lower than those of the parallel bifurcated flows. Therefore, particles in the SOL are transported to the divertor targets by flows nearly parallel to the magnetic field as schematically illustrated in Fig. 1-3(a). In the divertor leg, some impurity ions flow toward the divertor plates along the magnetic field lines and are evacuated, and the others reenter the core plasma by a flow directed from the divertor to the X-point produced by the ion pressure gradient and drift motions.

The impurity ion density in the core plasma must be minimized since the impurity ions can reduce the stored energy by bremsstrahlung and spontaneous emission (radiation loss) and reduce the fusion reaction rate by diluting the fuel (deuteron and triton) densities (see Fig. 1-4). Thus, the reduction in the impurity generation and the removal of impurities are important. The control of the divertor target surface temperature is a key to reducing the unintended impurity generation by sputtering, since the sputtering yield increases with the surface temperature. For tungsten, the sputtering yield from He^+ and Ar^+ bombardment increases with the surface temperature [16, 17], and the recrystallization further reduces the damage threshold [18]. For other materials such as lithium and carbon, the sputtering yield from D^+ bombardment depends on the surface temperature [19, 20]. Thus, the measurement of the surface temperature is important. In addition, to optimize the evacuation of impurities, understanding the impurity flow in the edge plasma will help to develop strategies to prevent their reentry to the core plasma. Thus, the measurement of the impurity ion flow is important.

For the measurements of the surface temperature and impurity ion flow, emission spectroscopy is being considered as standard diagnostics in ITER. The nuclear fusion device is operated under high neutron fluxes and gamma-ray dose rates, of up to 3×10^{18} m^{-2} s^{-1} and up to

2×10^{13} Gy s^{-1}, respectively, at the first wall of ITER [21]. In this respect, emission spectroscopy has an advantage of only requiring the installation of a metal mirror in the vicinity of the plasma and light can be transferred to a remotely located spectrometer . In this study, the surface temperature of the divertor target and the impurity ion flow were measured by emission spectroscopy, and this method is expected to contribute to accurate and reliable measurements in ITER and a demonstration fusion reactor (DEMO).

1.3 Outline of the Thesis

Chapter 2 introduces the fundamentals to required understand the contents of this thesis. Firstly, the radiometric quantities and units are explained. Then, the energy levels, the excitation and emission processes in plasmas, and the coronal model used to estimate the particle density from the line intensity are shown for C^{2+} ions and hydrogen molecules, which are the targets of this study.

Chapter 3 describes the construction of a model of the increase in the rotational temperature of ground-state hydrogen molecules in a plasma using a one-dimensional rate equation. Early studies of plasma-facing surface thermometry using the rotational temperature of hydrogen molecules are introduced. The translational, vibrational, and rotational temperatures of hydrogen molecules are defined. An assumption on the dynamics of hydrogen molecules near the plasma-facing walls is made and the factors that can affect the rotational temperature are explained. Among the factors, detailed explanations are given for the collisional-radiative processes in a plasma. Finally, the validity and limit of the applicability of the model are discussed.

Chapter 4 discusses experimental results of surface thermometry using the rotational temperature of hydrogen molecules in three tokamaks: LTX-β, QUEST, and DIII-D. The devices, experimental conditions, and spectroscopic systems are explained. The measured spectra are shown and the method used to evaluate the rotational temperature is described. Finally, the evaluated rotational temperature is compared with the calculation results of the model constructed in Chapter 3.

Chapter 5 is dedicated to spectroscopic measurements of the impurity ion flow. The three regions of the edge plasmas are defined and the flow distribution is explained. Then, the factors used to define the spectral shape and the method used to estimate the C^{2+} ion flow velocity from the Doppler shift are explained. Three types of plasma produced in QUEST, simulating the three regions of the edge plasmas, are explained. Then, a spectroscopic system with multiple viewing chords and its calibration methods are described. Inversion methods applied to derive the radially resolved distributions of emissivity, toroidal velocity, and temperature of ions are explained and the errors in the derived quantities are evaluated using synthesized spectra.

2 Emission Processes of Impurity Ions and Hydrogen Molecules in Edge Plasmas

2.1 Radiometric Quantities and Units

Plasma emission spectroscopy is a diagnostic method used to observe and analyze emission from a plasma. A typical setup for emission spectroscopy is schematically shown in Fig. 2-1. The emission from the plasma is collected by collection optics. The lens focuses the emission from the plasma onto an optical fiber. Gray lines show the solid angle where the optical fiber can collect the emission, which is called the viewing chord. In this study, the viewing chords are represented by their optical axes.

The intensity of the collected emission is described by radiometric quantities. The radiant flux in the unit of [W] is the energy emitted from a radiation source per unit time. The radiant flux received by a surface per unit area is defined as the irradiance and expressed in the units of [W m^{-2}]. The directional dependence of the radiant flux is expressed by the radiant intensity in the unit of [W sr^{-1}], which is defined as the radiant flux emitted in a specific direction per unit solid angle. The radiance [W sr^{-1} m^{-2}] and emissivity [W sr^{-1} m^{-3}] describe the radiant intensity emitted from a unit

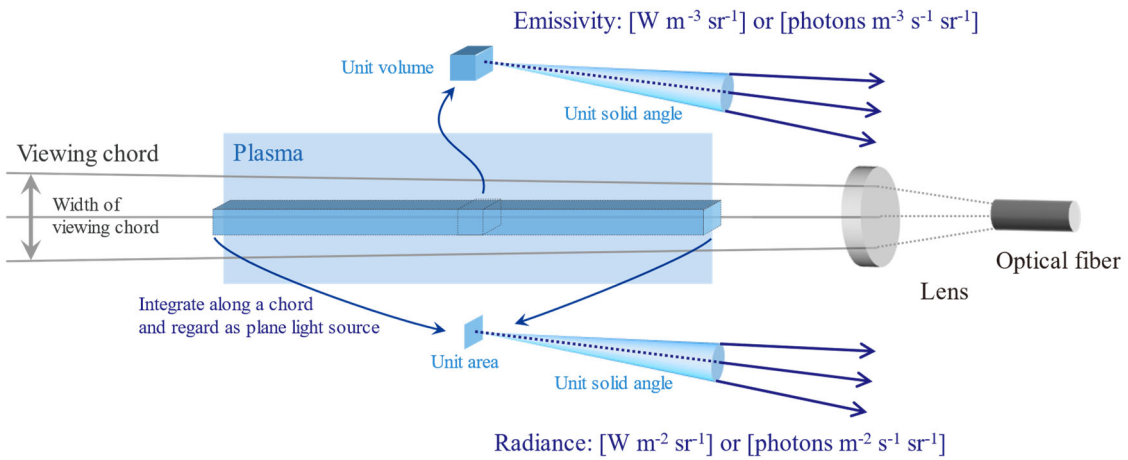

Fig. 2-1. Schematic illustration of setup for emission spectroscopy of plasma. Gray lines show the axis and width of the viewing chord, and blue rectangle represents the plasma. Emissivity is the radiant flux emitted from a unit volume in a specific direction per unit solid angle, and radiance is the radiant flux emitted from a unit area in a specific direction per unit solid angle.

area and a unit volume, respectively. Note that the radiance is expressed as the radiant intensity from a unit area perpendicular to the direction of the radiation. For the measurement shown in Fig. 2-1, the emission collected from the plasma per unit volume is expressed by the emissivity. The emission collected from a unit area of a plasma cross section can be considered as the emission from a plane radiation source and is expressed by the radiance.

In spectroscopy, the radiometric quantities per wavelength or frequency are generally utilized. These quantities are denoted as “spectral” radiometric quantities. In this study, the spectral radiometric quantities divided by the wavelength were adopted. The units of spectral radiance and spectral emissivity are [W sr^{-1} m^{-2} nm^{-1}] and [W sr^{-1} m^{-3} nm^{-1}], respectively. The quantities not divided by the wavelength or frequency are sometimes denoted as “integral” radiometric quantities.

2.2 Energy Levels of C^{2+} Ions and Hydrogen Molecules

Atoms, ions, and molecules have quantized internal energies known as “energy levels”. The radiation from particles in a plasma, which is used for spectroscopic measurements, results from the transition between energy levels.

Fig. 2-2 shows a subset of the energy levels of C^{2+} ions [22]. In the fusion plasmas, C^{2+} ions are produced by ionization from C atoms via ionization to C^{+} ions and are lost by ionization to C^{3+} ions. The ionization energy from C atoms to C^{2+} ions is 35.64 eV, and that from C^{2+} ions to C^{3+} ions is 47.89 eV [22]. In the figure, the indices on the horizontal axis denote the electronic configurations of the outermost shell.

The energy levels of hydrogen molecules are shown in Fig. 2-3 [23, 24, 25]. The horizontal axis shows the internuclear distance. The energy levels of hydrogen molecules consist of electronic, vibrational, and rotational levels. The electronic levels are determined by the configuration of electrons, which is similar to the energy levels in atoms and ions. The curves in Figs. 2-3(a) and (b) represent the potential curves of the electronic levels. The vibrational levels originate from the vibration of the nuclei, exist for each electronic level, and are shown as horizontal lines in Fig. 2-3(a). The rotational levels originate from the rotation of the molecules and exist for each vibrational level. They are shown as short horizontal lines in Fig. 2-3(c), an enlarged view of Fig. 2-3(a).

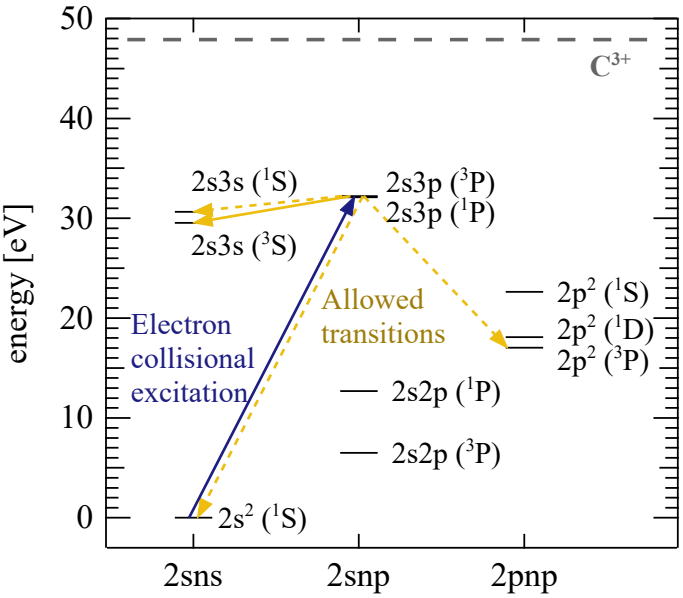

Fig. 2-2. Energy levels of C^{2+} (short horizontal lines). Dashed line shows the ground state of C^{3+} [22]. Yellow arrows show the allowed transitions and the solid arrow shows the target emission. Dark blue arrow shows the electron collisional excitation.

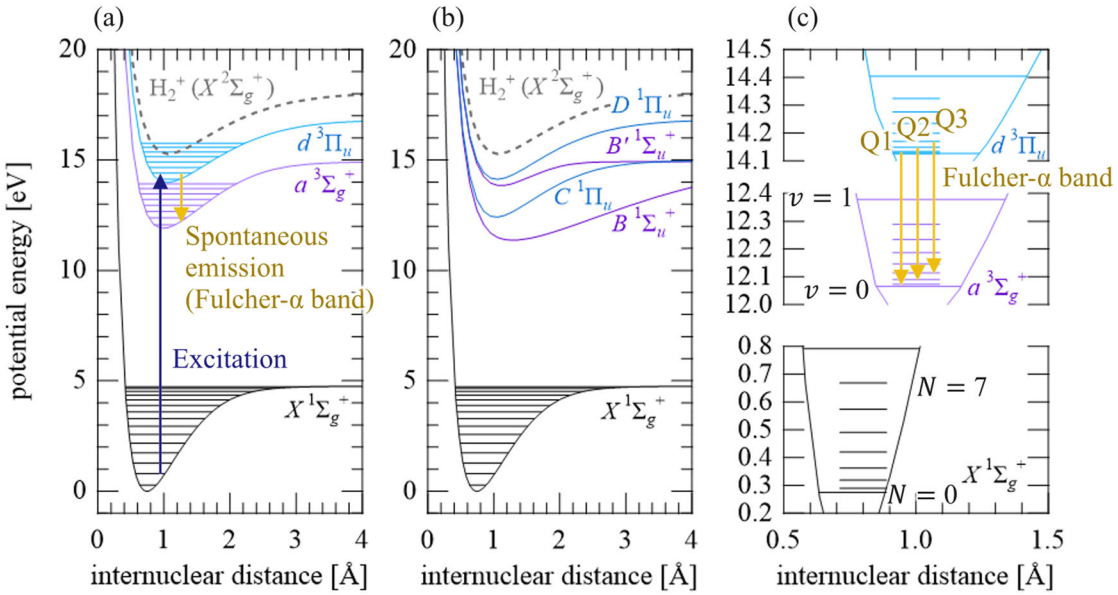

Fig. 2-3. (a) and (b) Potential curves of H_2 (solid lines) [23, 24, 25] and H_2^+ (dashed line) [26]. Vibrational levels for the X, d, and a states are shown by the horizontal lines [24]. Dark blue and yellow arrows respectively show the excitation and spontaneous emission. (c) Enlarged view of (a). Rotational energy levels are shown as short horizontal lines. Yellow arrows indicate the Fulcher-α band, the emission observed in this study.

2.3 Collisional-Radiative Processes of C^{2+} Ions and Hydrogen Molecules

Atoms, ions, and molecules in a plasma transit between their quantum states through collisional-radiative processes. The important processes for a fusion plasma are shown in Figs. 2-4(a) and (b) for ions and molecules, respectively. The dark blue and yellow arrows show the collisional and radiative processes, respectively. Horizontal lines show their quantum states. State p and q are the lower and upper states, respectively, and z is the ground state of the ions in the next ionization stages. In Fig. 2-4(b), the vibrational and rotational states are expressed by the dashed and dotted lines, respectively, and v and N denote the vibrational and rotational quantum numbers, respectively.

For ions, seven processes are shown in Fig. 2-4(a): collisional excitation and deexcitation, spontaneous transition, ionization, charge exchange, three-body recombination, and radiative recombination. The collisional excitation and deexcitation are caused mostly by collisions with electrons. The collisional excitation flux (population excited by electron collisions per unit time) is expressed as

$$C_{\mathrm{e}}(p,q)\, n(p)\, n_{\mathrm{e}}, \tag{2-1}$$

where p and q are the lower and upper states of the excitation process, respectively, $C_{\mathrm{e}}(p,q)$ is the excitation rate coefficient for the electron collision, $n(p)$ is the population of the lower state p, and n_{e} is the electron density. Similarly, the flux of deexcitation from state q to state p by electron collision is expressed as

$$F_{\mathrm{e}}(q,p)\, n(q)\, n_{\mathrm{e}}, \tag{2-2}$$

where $F_{\mathrm{e}}(p,q)$ is the deexcitation rate coefficient for the electron collision. These rate coefficients are functions of the electron temperature. The spontaneous transition is one of the radiative processes leading to emission of radiation whose energy is equal to the difference in energy level. The flux of the spontaneous emission is expressed as

$$A(q,p)n(q), \tag{2-3}$$

where $A(q,p)$ is the Einstein A coefficient for the transition from state q to state p. Absorption is the inverse process of spontaneous transition and can be neglected when the population of the upper

state is small. For the plasmas in this study, the population of the 2s3p ($^3P_2$) state was 10^7 times smaller than that of the ground state, and the absorption was negligible. The ionization is caused by collisions with electrons. The flux of the ionization is the product of the density of ionized particles, the electrons density, and the rate coefficient of the process. The charge exchange is the process by means of which an ion captures one or more electrons of an atom. The flux of the charge exchange is the product the density of ionized particles, the atomic density, and the rate coefficient of the process. For the plasmas in this study, the charge exchange between C^{2+} ions and hydrogen atoms was negligible because of the long mean free path. The three-body recombination is the inverse process of ionization by electron collisions: the ion recombines due to a collision with two electrons. The flux of the three-body recombination is the product of the density of the particles, the square of the electron density, and the rate coefficient of the process. The radiative recombination is another recombination process, during which the excess energy is emitted as radiation. The flux of the radiative recombination is the product of the density of the particles, the electron density, and the rate coefficient of the process.

For molecules, dissociation and electron attachment can also occurr in addition to the processes listed above. For an hydrogen molecule, two hydrogen atoms are produced by dissociation. The electron attachment process produces a negative molecular ion, whose ground state is shown as z^- in Fig. 2-4(b).

In this study, emission from C^{2+} ions and hydrogen molecules was analyzed. The C^{2+} ion has the electron configuration $1s^2\ 2s^2$, and one of the 2s electrons is excited by electron collision and radiatively deexcited in plasma. The yellow solid arrow in Fig. 2-2 shows the emission used for the measurement in this study: 2s3s ($^3S_1$) – 2s3p ($^3P_2$). The hydrogen molecules in the edge plasmas transit their rovibrational states in the electronic ground state by collision with electrons, ions, atoms, and molecules, and are electronically excited by electron collisions and deexcited by spontaneous transition. The radiation by the spontaneous transition from the $d\ ^3\Pi_u$ state to the $a\ ^3\Sigma_g^+$ state, called the Fulcher-α band, is used for the measurement in this work and shown by yellow arrow in Fig. 2-3(a). The Fulcher-α band contains the transitions between various rovibrational states. The transitions $v' = v'' = 0$ and $N' = N''$ were measured in this study, where v and N are the vibrational and

rotational numbers, and single and double primes are the states of the upper (d) and lower (a) states, respectively. The transition $N' = N''$ is called the Q-branch, and Q1, Q2, Q3, …, indicate the transitions $N' = N'' = 1, 2, 3, \ldots$, respectively (see yellow arrows in Fig. 2-3(c)).

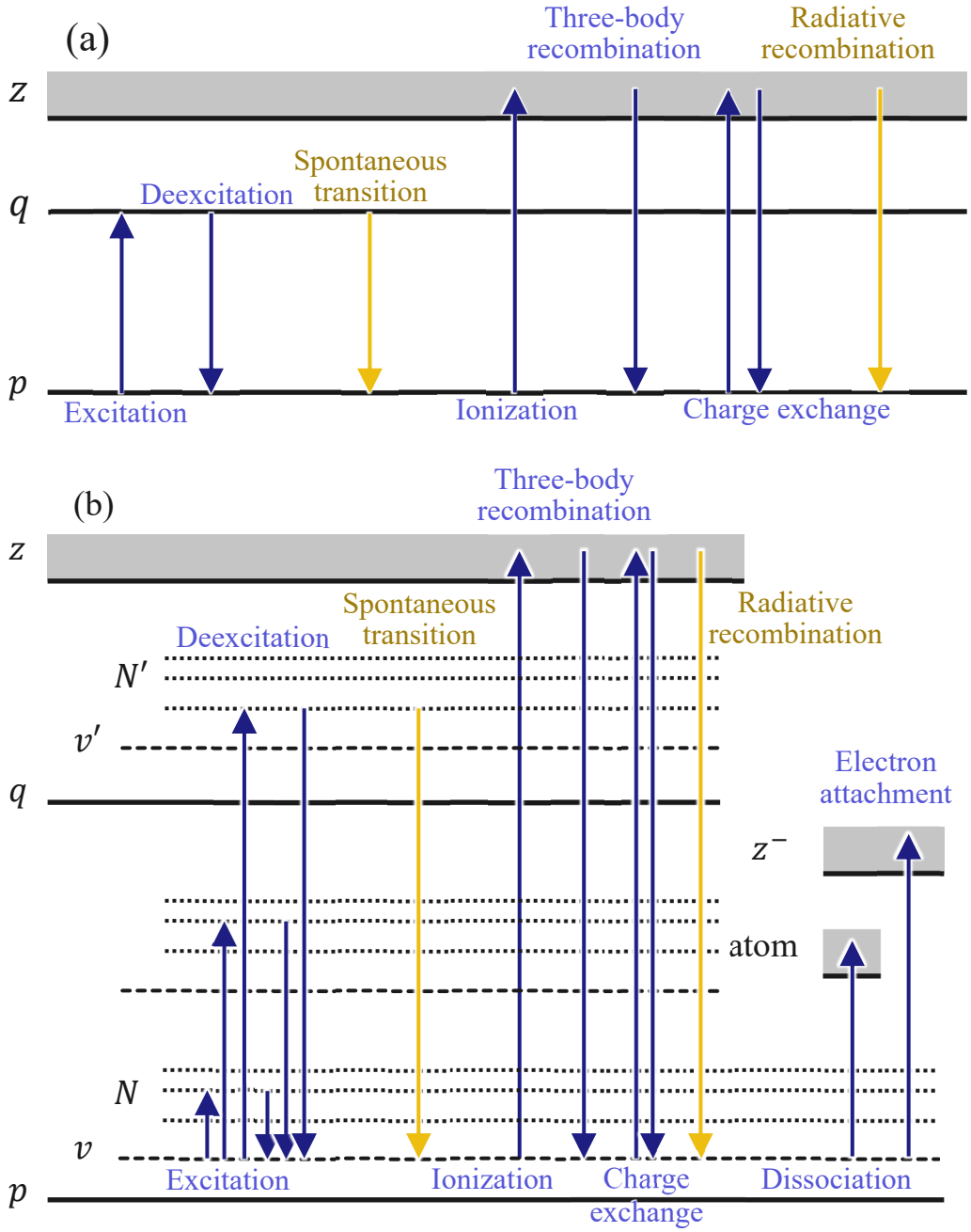

Fig. 2-4. Transition processes of the quantum states for (a) ions and (b) molecules. Dark blue and yellow arrows show the collisional and radiative processes, respectively.

2.4 Coronal Model

Under coronal equilibrium, the excitation flux due to electron collisions from ground state to state q is equal to the spontaneous emission from state q;

$$C_{\mathrm{e}}(1,q)\, n(1)\, n_{\mathrm{e}} = \sum_{p} A(q,p) n(q). \tag{2-4}$$

The summation on the right-hand side is the sum for all the allowed transitions from state q. The population of the ground state can be derived using Eq. (2-4) when the population of state p, n_{e}, and T_{e} are given.

For the C^{2+} ion, all the allowed transitions are shown by yellow arrows in Fig. 2-2. The sum of the fluxes for these transitions is equal to the excitation flux due to electron collisions from the ground state, which is indicated by the blue arrow in Fig. 2-2. The population of state p is derived from the emissivity of an allowed transition using the following equation:

$$\varepsilon_{qp} = \frac{h\nu}{4\pi} n(q) A(q,p), \tag{2-5}$$

where h and ν are Planck's constant and the frequency of the transition, respectively, and $h\nu$ is the difference in energy between states p and q. The population of the ground state of C^{2+} ions can then be estimated from Eq. (2-4).

For the hydrogen molecule, only the transition to the *a* state is allowed from the *d* state. Thus, the excitation flux from the ground state ($X\,{}^1\Sigma_g^+$ state) is balanced with the flux of the Fulcher-α band (see Fig. 2-3). The population of the ground state can also be estimated using Eqs. (2-4) and (2-5).

3 Modeling of Increase in Rotational Temperature of Hydrogen Molecules Near Plasma-Facing Walls

3.1 Surface Thermometry of Plasma-Facing Walls

Monitoring the surface temperature of plasma-facing components will be required in a fusion reactor to prevent damage to wall materials. In ITER, the maximum tolerable heat flux to the tungsten plasma-facing walls is 10 MW m^{-2}, and the surface temperature is expected to reach ~1600 K [10]. The surface temperature must be kept below the recrystallization temperature of tungsten (1300–1700 K) to avoid its recrystallization and lowering the damage threshold [18]. Infrared (IR) thermography and thermocouples are commonly used to monitor the surface temperature. These methods still have limitations in their application to a reactor environment. The thermocouples must be embedded in the side of the plasma-facing walls to avoid direct plasma irradiation, and the separation between the positions of the thermocouples requires additional modeling of the heat transport to estimate the peak temperature [27]. IR thermography measures the surface temperature using Planck's law considering the material dependence of the emissivity[†], which is the radiation intensity ratio with respect to that of blackbody radiation. IR thermography has high spatial resolution, but its accuracy can be reduced by changing the surface condition. Figs. 3-1(a) and (b) show the changes in emissivity due to the recrystallization of tungsten and the oxidation of iron, respectively. For tungsten, the irradiance at 4.495 μm was calculated using the emissivity in [28]. The orange and blue lines show the irradiance as the sample is heated from 200 to 2200 K and then cooled, respectively. The irradiation during heating is different from that during cooling at the same T_{wall}. The recrystallization of tungsten is suggested as the reason for this difference, which could result in a measurement error of $\approx$ 200 K. For iron, the irradiance at 4 μm during oxidation is calculated at $T_{\mathrm{wall}} = 753$ K using the emissivity in [29]. The irradiance increases with the formation of an oxide film, which suggest the change in

[†] This is different from the radiometric quantity described in Section 2.1. The "emissivity" in this section always means the radiation intensity ratio with respect to that of blackbody radiation.

chemical composition can reduce the accuracy of thermography.

In this study, a novel method of obtaining surface temperatures from the rotational temperature of hydrogen molecules is proposed. Hydrogen molecules have three degrees of freedom of kinetic motions: translational, vibrational, and rotational motions. The kinetic energies of these motions are represented by the translational, vibrational, and rotational temperatures, respectively, which are the energies of the motions of the center of the mass and two nuclei. Among these temperatures, the translational and rotational temperatures are known to become close to the wall temperature in a plasma near the plasma-facing walls. The translational temperature can be measured from the Doppler width of the molecular emission lines, but accurate evaluation of the width is not easy because of the small width (the full width at half maximum (FWHM) of the Doppler width is 4 pm for 1000 K). Thus, only the rotational temperature might be used to infer the wall temperature. In a tokamak, TEXTOR (Tokamak Experiment for Technology Oriented Research), the rotational temperature of deuterium molecules was estimated from Fulcher-α band spectra measured at the graphite test limiter [30]. The rotational temperature was found to increase with the injected gas temperature and the limiter surface temperature as shown in Fig. 3-2(a). Fig. 3-2(b) shows another measurement of the deuterium molecular rotational temperature near the graphite target plate in the divertor of another tokamak, DIII-D (Doublet III-D) [31]. The rotational temperature was found to increase with the local electron density. These results show a correlation between the rotational temperature and the wall surface temperature, and more detailed understanding of the processes that determine the rotational temperature may enable the evaluation of the surface temperature from the rotational temperature. In this chapter, the effects of collisional-radiative processes on the increase in rotational temperature are quantitatively evaluated. A comparison of experimental results with predictions from the model will be presented in Chapter 4.

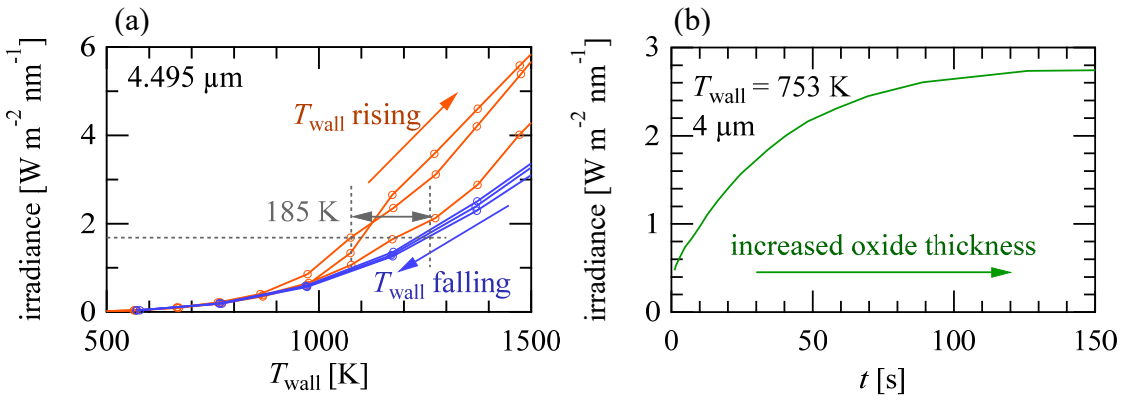

Fig. 3-1. (a) Irradiance at 4.495 µm from tungsten calculated using the emissivity in [28]. Orange and blue lines show the irradiance as the sample is heated to 2200 K and then cooled, respectively. (b) Irradiance at 4 µm from iron during oxidation at a constant surface temperature of 753 K calculated using the emissivity in [29].

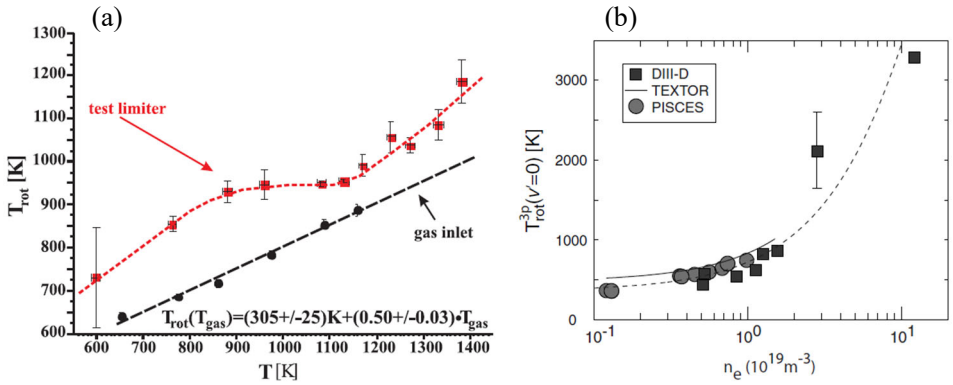

Fig. 3-2. Dependence of rotational temperature for *d* state of deuterium molecules on (a) gas temperature (black) and surface temperature of a graphite test limiter (red) in TEXTOR [30] and (b) electron density [31]. The rotational temperatures were measured using a viewing chord tangential to the test limiter in TEXTOR and viewing chords directed at the graphite divertor in DIII-D. The electron density was measured locally near the divertor by Thomson scattering.

3.2 Translational, Vibrational, and Rotational Temperatures and Emission Spectrum of Hydrogen Molecules

The energy distribution of hydrogen molecules is described by three temperatures: translational, vibrational, and rotational temperatures. The translational temperature describes the distribution of translational energies. The rovibrational temperatures are defined with the relative population distributions in the quantized energy states since the rovibrational energies are quantized. When the vibrational population distribution is determined by the Boltzmann distribution, the vibrational temperature T_{vib}^{X} is defined by

$$\begin{aligned} n(Xv) &= n(X) \cdot \frac{\exp\left[-\frac{G_X(v)}{k_{\mathrm{B}} T_{\mathrm{vib}}^{X}}\right]}{\sum_v \exp\left[-\frac{G_X(v)}{k_{\mathrm{B}} T_{\mathrm{vib}}^{X}}\right]} \\ &= n(X) \cdot C_X \exp\left[-\frac{G_X(v)}{k_{\mathrm{B}} T_{\mathrm{vib}}^{X}}\right], \end{aligned} \tag{3-1}$$

where X denotes the electronic ground state ($X\ ^1\Sigma_g^+$), v is the vibrational quantum number, $n(X)$ and $n(Xv)$ are the population of the X state and that of the X state in the vibrational state denoted by v, respectively, $G_X(v)$ is the vibrational energy, k_{B} is the Boltzmann constant, and C_X is the inverse of the partition function. The vibrational energy $G_X(v)$ is taken from [24]. Similarly, the rotational temperature T_{rot}^{Xv} is defined by the following relation of the rotational population $n(XvN)$:

$$\begin{aligned} n(XvN) &= n(Xv) \cdot \frac{g_N g_{\mathrm{as}}^N \exp\left[-\frac{F_X(v,N)}{k_{\mathrm{B}} T_{\mathrm{rot}}^{Xv}}\right]}{\sum_N g_N g_{\mathrm{as}}^N \exp\left[-\frac{F_X(v,N)}{k_{\mathrm{B}} T_{\mathrm{rot}}^{Xv}}\right]} \\ &= n(Xv) \cdot C_{Xv}\, g_N g_{\mathrm{as}}^N \exp\left[-\frac{F_X(v,N)}{k_{\mathrm{B}} T_{\mathrm{rot}}^{Xv}}\right], \end{aligned} \tag{3-2}$$

Where N is the rotational quantum number, $n(XvN)$ is the population of the X state in the vibrational and rotational states denoted by v and N, respectively, g_N is the multiplicity of the rotational state, g_{as}^N is the spin multiplicity of nuclei, $F_X(v,N)$ is the rotational energy, and C_{Xv} is the inverse of the partition function. The rotational energy $F_X(v,N)$ can be approximately obtained with the following polynomials [32]:

$$F_X(v,N) = B_v\,N(N+1) - D_v\,N^2(N+1)^2,$$
$$B_v = B_e - \alpha_e\left(v+\frac{1}{2}\right), \tag{3-3}$$
$$D_v = D_e,$$

Where B_e, α_e, and D_e are known as "molecular constants" and are unique for each electronic state. The values of the molecular constants have been compiled in a database [33].

In tokamak edge plasmas, owing to the relatively low frequency of intramolecular collisions, the translational and rovibrational temperatures are generally not in thermal equilibrium. In addition, the rovibrational population distributions deviate from the Boltzmann distribution. Fig. 3-3(a) shows an example of a rotational distribution measured for a plasma at 1 Pa [34] with the population of the high rotational states deviating from the Boltzmann distribution approximated by the population of the rotational states with $N \leq 5$. The rovibrational distributions measured near the divertor of DIII-D are plotted in Fig. 3-3(b), showing the difference between the vibrational (9840 K) and rotational (800–2300 K) temperatures of the *X* state [31]. In this study, the rotational temperature was evaluated by approximating the rotational population distributions in the states with $N \leq 5$ with Eq. (3-2).

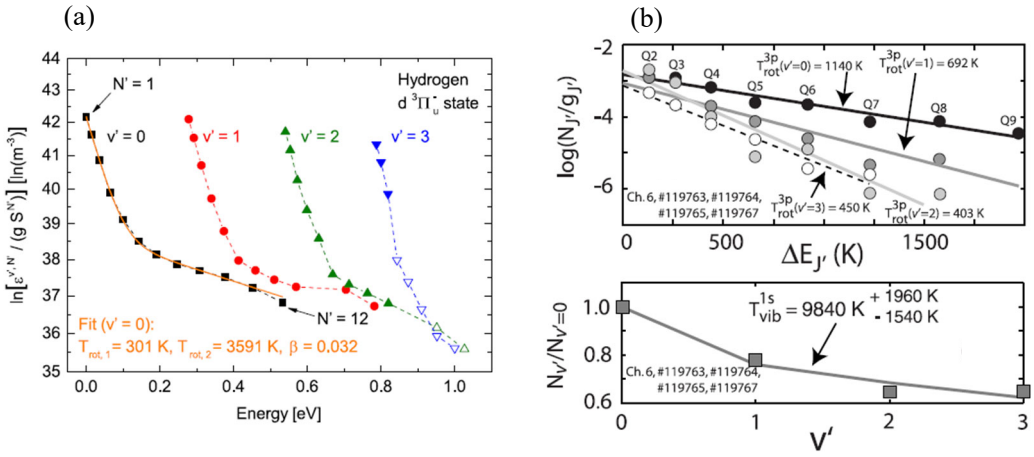

Fig. 3-3. (a) Rotational population divided by the statistical weight for multiple vibrational states of H_2 (*d* state) measured at 1 Pa [34]. (b) Rotational population of D_2 (*d* state) divided by the statistical weight and vibrational population of D_2 (*X* state) measured near the divertor of DIII-D [31]. The rotational temperature of the *d* state is expected to be half of that of the *X* state because of difference in molecular constants B_e.

3.3 Rotational Temperature of Hydrogen Molecules Near Plasma-Facing Walls

In this section, a mechanism relating the rotational temperature of hydrogen molecules to the surface temperature of plasma-facing walls is proposed. The main physical processes are illustrated in Fig. 3-4. In tokamak edge plasmas, hydrogen ions move along the magnetic field line and reach plasma-facing walls. The ions are charge-neutralized on the surface, diffuse, recombine at the surface, and are desorbed as molecules [35]. The rotational temperatures of the desorbed molecules are affected by both the surface temperature of the walls, T_{wall}, and the excitation due to recombination processes. The recombination processes can be endothermic or exothermic by a few eV, and basic experiments conducted using copper and tungsten surfaces suggested an increase in 'vibrational' temperature due to exothermic recombination [36]. The desorbed molecules move into the plasma and collide with electrons and protons. These collisions excite and deexcite the molecules rovibrationally and affect the rovibrational temperatures. Collisions with electrons and protons also lead to electronic excitation, and the excited molecules are deexcited by spontaneous emission. Experimentally, the rotational temperature is measured from the emission in the plasma, and thus the measured temperature is affected by the surface temperature, excitation due to recombination, and excitation due to collisions in the plasma. To derive surface temperatures from the measured rotational temperatures, the surface effects (surface temperature and excitation due to recombination) must be separated from the effects occurring in the plasma (excitation due to collisions). This chapter discusses a model constructed to describe the collisions in the plasma, which is used for the interpretation of the experimental data in Chapter 4.

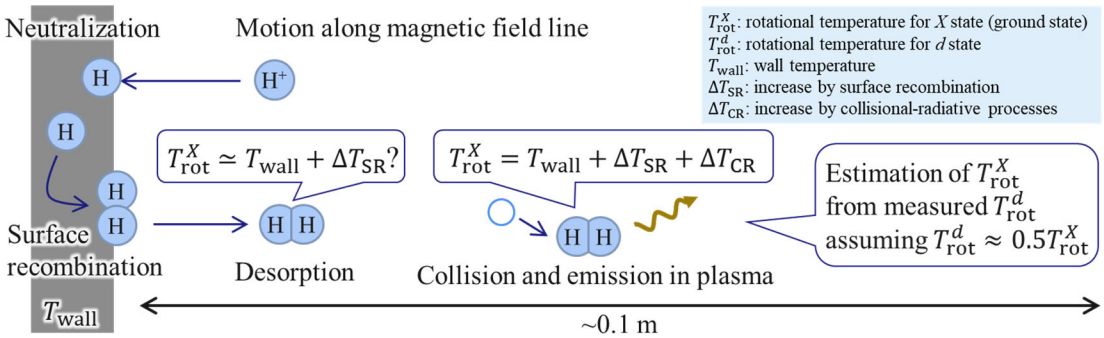

Fig. 3-4. Processes affecting the rotational temperature of hydrogen molecules near plasma-facing walls.

3.4 Modeling of Collisional Increase in Rotational Temperature of Hydrogen Molecules in Edge Plasma

3.4.1 Collisional-Radiative Processes Affecting Rotational Temperature

Several processes can affect the rotational population distribution for the ground state of hydrogen molecules including (i) excitation, (ii) deexcitation, (iii) spontaneous emission, (iv) dissociation, (v) ionization, (vi) the recombination of electron and hydrogen molecular ions, (vii) charge exchange, and (viii) electron attachment that produces negative hydrogen molecular ions. These processes can be expressed by the following reactions:

(i), (ii) $\mathrm{H}_2(X,v,N) + \mathrm{e/p/H/H}_2 \rightarrow \mathrm{H}_2(X,v,N') + \mathrm{e/p/H/H}_2$ ($|N-N'|$: even),

$\mathrm{H}_2(X,v,N) + \mathrm{e/p/H/H}_2 \rightarrow \mathrm{H}_2(X,v',N') + \mathrm{e/p/H/H}_2$ ($|N-N'|$: even),

$\mathrm{H}_2(X,v,N) + \mathrm{e/p/H/H}_2 \rightarrow \mathrm{H}_2(e,v',N') + \mathrm{e/p/H/H}_2$

($|N-N'|$: even or odd depending on e),

(iii) $\mathrm{H}_2(e,v',N') \rightarrow \mathrm{H}_2(X,v,N) + h\nu$,

(iv) $\mathrm{H}_2(X,v,N) + \mathrm{e/p} \rightarrow \mathrm{H} + \mathrm{H} + \mathrm{e/p}$,

(v) $\mathrm{H}_2(X,v,N) + \mathrm{e} \rightarrow \mathrm{H}_2^+ + \mathrm{e} + \mathrm{e}$,

(vi) $\mathrm{H}_2^+ + \mathrm{e} \rightarrow \mathrm{H}_2(X,v,N)$,

$\mathrm{H}_2^+ + \mathrm{e} + \mathrm{e} \rightarrow \mathrm{H}_2(X,v,N) + \mathrm{e}$,

(vii) $\mathrm{H}_2(X,v,N) + \mathrm{p} \rightarrow \mathrm{H}_2^+ + \mathrm{H}$,

(viii) $\mathrm{H}_2(X,v,N) + \mathrm{e} \rightarrow \mathrm{H}_2^-$,

where (X, v, N) denotes a set of the electronic state (X) and rovibrational quantum numbers (v and N), e in italics indicates an electronic state, and "e" and "p" represent electron and proton, respectively. The excitation and deexcitation, (i) and (ii), are mainly caused by electron and proton collisions and can be divided into three processes as shown by the three formulae above. They are referred to as pure rotational, rovibrational, and rovibronic excitations or deexcitations, respectively. For a rovibrational transition, a transition within the same electronic state, the symmetry of the nuclear spin requires the following selection rule for the initial and final rotational quantum numbers, N and N', respectively: $|\Delta N| = |N' - N| = 0,\ 2,\ 4, \ldots$. For a rovibronic transition, the selection rule requires that $|\Delta N|$ is either odd or even depending on the initial and final electronic states. There is no selection rule for the vibrational quantum number. Spontaneous emission is a transition between different electronic states since the transition electric dipole moment for diatomic molecules is large only for transitions between different electronic states. The selection rules for the rotational quantum number are the same as those for collisional excitation and deexcitation. The other reactions (iv)–(vii) reduce or increase the population in a rovibrational state.

3.4.2 Evaluation of Spatial Distribution of Rotational Temperature

The spatial distribution of the rovibrational population in the X state, $n(XvN)$, was derived by solving rate equations for evaluating the distribution of $T_{\mathrm{rot}}^{Xv=0}$. Assuming a steady state, the spatial derivative of $n(XvN)$ can be described by the temporal variation in $n(XvN)$ for molecules during their travel from the surface:

$$\frac{dn(XvN)}{dt} = v_{\mathrm{H_2}}(l) \cdot \frac{\partial n(XvN)}{\partial l}, \tag{3-4}$$

where l is the one-dimensional coordinate system perpendicular to the plasma-facing surface and directed toward the plasma, and $v_{\mathrm{H_2}}(l)$ is the velocity of the molecules, which is generally a function of l. The right-hand and left-hand sides are in Lagrangian and Eulerian forms, respectively. In this study, $v_{\mathrm{H_2}}$ was assumed to be constant since the mean free paths for the momentum transfer of the molecules by collisions with electrons, protons, hydrogen atoms, and hydrogen molecules in the

plasma are longer than the considered spatial lengths (10^{-2}–10^{-1} m). Therefore, the spatial distribution of $n(XvN)$ can be calculated by solving rate equations expressed in the form

$$\frac{dn(XvN)}{dt} = S_{\text{creation}} - S_{\text{annihilation}}, \tag{3-5}$$

where S_{creation} and $S_{\text{annihilation}}$ are respectively the fluxes created and annihilated to the state (XvN) due to the processes described in Subsection 3.4.1.

The creation and annihilation fluxes of the rate equations were determined by considering processes (i) and (ii) by electron and proton collisions and process (iii), and ignoring the other processes (iv)–(viii) in this study. For processes (i) and (ii), rovibrational excitation and deexcitation in the *X* state due to electron and proton collisions, and electronic excitation due to electron collisions were considered. The electronic excitation was considered as that to a virtual electronic excited state "e'". The e' state corresponds to the bundled $B\ ^1\Sigma_u^+$, $B'\ ^1\Sigma_u^+$, $C\ ^1\Pi_u$, and $D\ ^1\Pi_u$ states, which have the largest excitation fluxes from the *X* state [37]. Atomic and molecular collisional excitations were neglected because of the small fluxes. For instance, the fluxes of the pure rotational excitation by collisions with electrons, protons, hydrogen atoms, and hydrogen molecules are estimated to be ~10^{19}, 10^{18}, 10^{16}, and 10^{14} m^{-3} s^{-1}, when $n_e = n_p = 10^{17}$ m^{-3}, $n_H = 10^{16}$ m^{-3}, $n_{H_2} = 10^{16}$ m^{-3}, $T_e = 20$ eV, $T_p = 10$ eV, $T_H = 1.5$ eV, and $T_{H_2,\text{trans}} = 300$ K [38], where n and T are the density and temperature, the subscripts "e", "p", "H", and "H_2" indicate electrons, protons, hydrogen atoms, and hydrogen molecules, respectively, and $T_{H_2,\text{trans}}$ is the translational temperature of hydrogen molecules. Note that the atomic collisional excitation flux is comparable to the proton collisional excitation flux when $n_H/n_p \approx 10$. The rovibrational excitation and deexcitation in the e' state were ignored because of the short lifetime. Process (iv) contains the dissociation by rovibrational excitation in the ground state and that by excitation to the repulsive state $b\ ^3\Sigma_u^+$. The effect of the former was evaluated as the vibrational and rotational excitations from $v = 14$ and $N = 25$, respectively, which was negligible when $n_e = n_p \leq 10^{19}$ m^{-3}. Process (v) by electron collisions and process (vii) have cross sections comparable to those for the electron and proton collisional rovibrational excitations, respectively, and can affect the rotational population distribution [38, 39]. However, these processes

were ignored since the rotationally resolved cross section data is not available. The effects of processes (vi) and (viii) are unknown because of the lack of valid data. Thus, the rate equations used for the model are expressed as

$$\begin{aligned}
&\frac{dn(XvN)}{dt} \\
&= \sum_{v',N'} [A(e'v'N', XvN)\, n(e'v'N') - C_{\mathrm{e}}(XvN, e'v'N')\, n(XvN)\, n_{\mathrm{e}}] \\
&+ \sum_{(v',N')<(v,N)} [C_{\mathrm{e}}(Xv'N', XvN)\, n(Xv'N') - F_{\mathrm{e}}(XvN, Xv'N')\, n(XvN)]\, n_{\mathrm{e}} \\
&+ \sum_{(v',N')>(v,N)} [F_{\mathrm{e}}(Xv'N', XvN)\, n(Xv'N') - C_{\mathrm{e}}(XvN, Xv'N')\, n(XvN)]\, n_{\mathrm{e}} \\
&+ \sum_{(v',N')<(v,N)} \left[C_{\mathrm{p}}(Xv'N', XvN)\, n(Xv'N') - F_{\mathrm{p}}(XvN, Xv'N')\, n(XvN)\right] n_{\mathrm{p}} \\
&+ \sum_{(v',N')>(v,N)} \left[F_{\mathrm{p}}(Xv'N', XvN)\, n(Xv'N') - C_{\mathrm{p}}(XvN, Xv'N')\, n(XvN)\right] n_{\mathrm{p}},
\end{aligned} \tag{3-6}$$

where $A(e'v'N', XvN)$ is the Einstein A coefficient for the spontaneous transition from (e', v', N') to (X, v, N), and $C(XvN, Xv'N')$ and $F(XvN, Xv'N')$ are the rate coefficients for collisional excitation and deexcitation, respectively, from (X, v, N) to (X, v', N'). The subscripts "e" and "p" indicate the collisions with electrons and protons, respectively, and the rate coefficients depend on their temperatures. The first term on the right-hand side of Eq. (3-6) includes the spontaneous transition from the virtual electronic state e' and the excitation by electron collisions to the e' state. The second term is the electron collisional excitation from the lower states and deexcitation to the lower states. The third term is the electron collisional excitation to and deexcitation from the upper states. The fourth and fifth terms are excitation and deexcitation due to the proton collisions.

The rate equations were solved for the rovibrational states with $0 \leq v \leq 14$ and $0 \leq N \leq 25$ for the X state and the rovibrational states with $0 \leq v \leq 17$ and $0 \leq N \leq 25$ for the e' state; namely, 858 simultaneous differential equations were solved. The initial conditions were given as follows: $n(XvN)$ follows the Boltzmann distribution at $T_{\mathrm{rot}}^{Xv}(l = 0) = T_{\mathrm{vib}}^{X}(l = 0) = T_{\mathrm{wall}}$, and $n(e'v'N') = 0$. The velocity of the molecules $v_{\mathrm{H_2}}$ was given as the thermal velocity at T_{wall}: $v_{\mathrm{H_2}} =$

$\sqrt{k_{\mathrm{B}}T_{\mathrm{wall}}/m_{\mathrm{H_2}}}$, where $m_{\mathrm{H_2}}$ is the mass of a hydrogen molecule. The spatial profiles of $n_{\mathrm{e}}(l)$, $n_{\mathrm{p}}(l)$, $T_{\mathrm{e}}(l)$, and $T_{\mathrm{p}}(l)$ were also given, and their arguments were converted to time by using the relation $l = v_{\mathrm{H_2}}t$. The forward Euler and Runge–Kutta methods were used to solve the first term and the other terms of Eq. (3-6), respectively. The time step of $\Delta t = 10^{-9}$ s was adopted because the change in $T_{\mathrm{rot}}^{Xv=0}$ due to Δt was small.

The spatial distribution of $T_{\mathrm{rot}}^{Xv=0}$ was evaluated from the calculated $n(XvN)$ by fitting the populations in the states with $v = 0$ and $N \leq 5$ to Eq. (3-2) at every 100 time steps of the calculation. The spatial distribution of T_{vib}^{X} was also evaluated from the calculated $n(Xv)$ by fitting the populations in the states with $v \leq 4$ (containing all the rotational states) to Eq. (3-1).

A summary of the cross sections (also shown in Fig. 3-5) and Einstein A coefficients data is given in Table 3-1. The notation $(v,\ N) \rightarrow (v',\ N')$ represents the rovibrational state before (without prime) and after (with prime) the transition, and the symbol X is omitted when it represents the transition in the ground state. The notation without v and/or N, *e.g.* (B) and $(X,\ v)$, represents a rovibrationally or rotationally unresolved state. For the pure rotational excitation by electron collisions, the cross sections for $(v = 0,\ N = 0) \rightarrow (v' = 0,\ N' = 2)$ and $(v = 0,\ N = 1) \rightarrow (v' = 0,\ N' = 3)$ transitions were taken from [40]. The cross sections for $(v = 0,\ N \geq 2) \rightarrow (v' = 0,\ N' = N + 2)$ transitions were approximated to be the same as that for $(v = 0,\ N = 1) \rightarrow (v' = 0,\ N' = 3)$ transition, since the ratios between the cross sections for $(v = 0,\ N = 2, 3) \rightarrow (v' = 0,\ N' = N + 2)$ transitions and $(v = 0,\ N = 1) \rightarrow (v' = 0,\ N' = 3)$ transition are 0.7–0.9 and nearly equivalent [41]. The pure rotational excitation with $\Delta N \geq 4$ was neglected since the cross section for the excitation with $\Delta N = 4$ is 10^3 times smaller than that with $\Delta N = 2$ [41]. For the pure rotational excitation in the vibrational states with $v \geq 1$, *i.e.*, $(v \geq 1,\ N) \rightarrow (v' = v,\ N' = N + 2)$ transitions, the cross sections were considered to be the same as those for $(v = 0,\ N) \rightarrow (v' = 0,\ N' = N + 2)$ transitions.

For the vibrational excitation by electron collisions, the cross sections calculated by a method described in [42] were used. For transitions without available cross sections, the excitation cross sections were calculated from the deexcitation cross sections using the Klein–Rosseland relationship [43]. The cross sections for $(v,\ N > N_{\mathrm{max}}) \rightarrow (v' > v,\ N' = N)$ transitions were

approximated to be the same as that for $(v,\ N = N_{\max}) \rightarrow (v' > v,\ N' = N_{\max})$ transition, where $N_{\max}$ is the maximum quantum number of the available cross sections for $(v,\ N) \rightarrow (v' > v,\ N' = N)$ transitions. For the rovibrational excitation, *i.e.*, $(v,\ N) \rightarrow (v' > v, N' = N \pm 2)$ transitions, the cross sections were approximated to be the same as those for $(v,\ N) \rightarrow (v' > v, N' = N)$ transitions. Note that transitions were neglected when the cross sections were smaller than 10^{-23} m^{-3}.

The pure rotational and rovibrational excitations by proton collisions were considered using the cross sections in [44]. The cross sections for $(v = 0,\ N = 0) \rightarrow (v' = 0,\ N' = 2)$ and $(v = 0,\ N = 1) \rightarrow (v' = 0,\ N' = 3)$ transitions were taken from [44], and those for $(v = 0,\ N \geq 2) \rightarrow (v' = 0,\ N' = N + 2)$ transitions were assumed to be the same as that for the $(v = 0,\ N = 1) \rightarrow (v' = 0,\ N' = 3)$ transition. For the vibrational excitation, the cross sections for $(v = 0,\ N = 0) \rightarrow (v' = 1\text{–}3,\ N' = 0)$ transition were taken from [44]. For $(v = 1\text{–}5,\ N = 0) \rightarrow (v' = v + 1,\ N' = 0)$ transitions, the cross sections were scaled from that for $(v = 0,\ N = 0) \rightarrow (v' = 1,\ N' = 0)$ transition assuming that their ratios were the same as those for the electron collision excitation at 4 eV taken from [45], following the procedure adopted in [38]. The cross sections for $(v \geq 6,\ N = 0) \rightarrow (v' = v + 1,\ N' = 0)$ transitions were assumed to be the same as that for the $(v = 5,\ N = 0) \rightarrow (v' = 6,\ N' = 0)$ transition. The cross sections for pure rotational excitation in vibrational states with $v \geq 1$, *i.e.*, $(v \geq 1,\ N) \rightarrow (v' = v,\ N' = N + 2)$ transitions, were assumed to be the same as those for $(v = 0, N) \rightarrow (v' = 0,\ N' = N + 2)$ transitions. Also, the cross sections for the rovibrational excitation, *i.e.*, $(v,\ N) \rightarrow (v' > v, N' = N \pm 2)$ transitions, were approximated to be the same as those for $(v,\ N) \rightarrow (v' > v, N' = N)$ transitions.

For the transitions between the electronic states, the cross sections for the electron collisional excitation from $(X,\ v = 0)$ were taken from [46], and the rovibrationally resolved Einstein A coefficients were taken from [47]. The excitation cross sections for the transitions from the vibrational excited states ($v \geq 1$) were assumed to be the same as those for the ground state. These cross sections were rovibrationally resolved with respect to the upper states. The vibrational resolution was performed by multiplying the cross sections by the Franck–Condon factors taken from [24]. The rotational resolution was performed by assuming the same cross sections as for the transitions with

$\Delta N \leq 1$ following the procedure adopted in [38]. The excitation cross sections for $(X, v, N) \rightarrow (e', v', N')$ transitions were determined to be the sum of the cross sections for the adopted four electronic excited states. The Einstein A coefficients for $(e', v', N') \rightarrow (X, v, N)$ transitions were regarded as the weighted average of the coefficients for the transitions from the four adopted electronic excited states. The rovibrational populations in the four electronic excited states were estimated individually from the excitation fluxes to the states assuming the coronal equilibrium. Then, the proportions of the rovibrational population with (v', N') in the four electronic excited states were used as the weights.

For all the cross-section data, when the maximum energy range of the available data was less than 500 eV, the data were extrapolated up to 500 eV by fitting them to power functions of energy E. The extrapolated data are shown by dashed lines in Fig. 3-5.

The rate coefficients were calculated from the cross sections. For excitation due to electron collisions, the following equation was used [43]:

$$C_{\mathrm{e}}(XvN, Xv'N') = \int_0^\infty \sqrt{\frac{2E}{m}} \sigma_{XvN \rightarrow Xv'N'}(E)\, f(E)\, dE, \tag{3-7}$$

where $\sigma_{XvN \rightarrow Xv'N'}(E)$ is the cross section for the excitation from (X, v, N) to (X, v', N'), E is the kinetic energy of electrons relative to the target particle, m is the reduced mass, and $f(E)$ is the Maxwell energy distribution. The excitation rate coefficients were calculated using the cross section shown in Fig. 3-5, and then the deexcitation rate coefficients were derived using the Klein–Rosseland relationship [43].

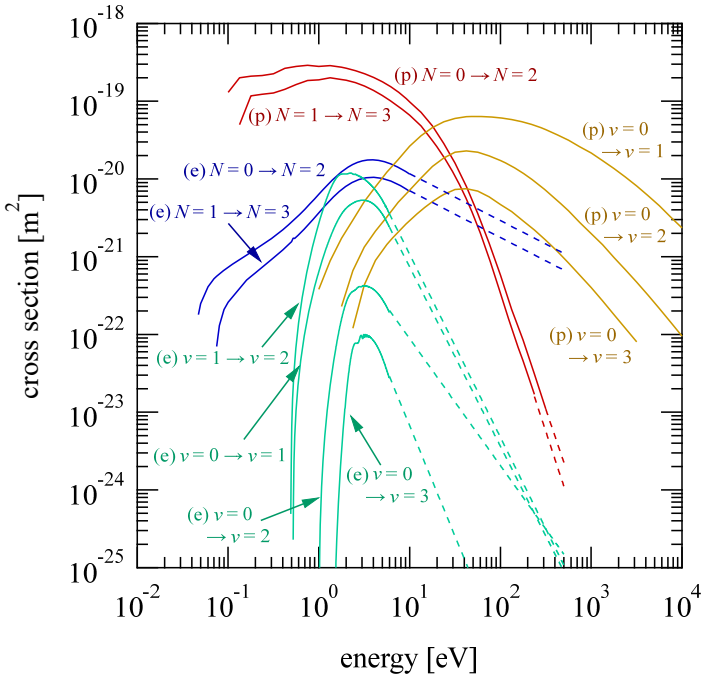

Fig. 3-5. Cross sections of rovibrational excitation of H_2 X state by electron (e) and proton (p) collisions [40, 42, 44]. The extrapolated data are shown by dashed lines.

Table 3-1. Summary of cross sections and Einstein A coefficients.

Pure rotational excitation by electron collisions	
$(v = 0,\ N = 0\text{–}1) \rightarrow (v' = 0,\ N' = N + 2)$	[40]
$(v = 0,\ N \geq 2) \rightarrow (v' = 0,\ N' = N + 2)$	Same as $(v = 0,\ N = 1) \rightarrow (v' = 0,\ N' = 3)$
$(v \geq 1,\ N) \rightarrow (v' = v,\ N' = N + 2)$	Same as $(v = 0,\ N) \rightarrow (v' = 0,\ N' = N + 2)$
Rovibrational excitation by electron collisions	
$(v = 0,\ N) \rightarrow (v' = 1\text{–}7,\ N' = N)$ $(v = 1\text{–}7,\ N) \rightarrow (v + 1 \leq v' \leq 8,\ N' = N)$ $(v = 9\text{–}13,\ N) \rightarrow (v + 1 \leq v' \leq 14,\ N' = N)$	Calculation by method in [42]
$(v = 1\text{–}8,\ N) \rightarrow (v' = 9\text{–}13,\ N' = N)$	Derived from deexcitation cross sections calculated by method in [42].
$(v,\ N > N_{\max}) \rightarrow (v' > v,\ N' = N)$, where $N_{\max}$ is maximum quantum number of provided cross sections for $(v,\ N) \rightarrow (v', N' = N)$	Same as $(v,\ N = N_{\max}) \rightarrow (v',\ N' = N_{\max})$
$(v,\ N) \rightarrow (v' \neq v,\ N' = N \pm 2)$	Same as $(v,\ N) \rightarrow (v',\ N' = N)$
Rovibronic excitation by electron collisions	

$(X,\ v=0) \rightarrow (B)$ $(X,\ v=0) \rightarrow (C)$ $(X,\ v=0) \rightarrow (B')$ $(X,\ v=0) \rightarrow (D)$	[46], vibrationally resolved by multiplying Franck–Condon factors given in [24] and rotationally resolved assuming no rotational dependence following procedure shown in [38]
$(X,\ v\neq 0) \rightarrow (B)$, (C), (B'), or (D)	Same as $(X,\ v=0) \rightarrow (B)$, (C), (B'), or (D) and rovibrationally resolved
Pure rotational excitation by proton collisions	
$(v=0,\ N=0\text{–}1) \rightarrow (v'=0,\ N'=N+2)$	[44]
$(v=0,\ N\geq 2) \rightarrow (v'=0,\ N'=N+2)$	Same as $(v=0,\ N=1) \rightarrow (v'=0,\ N'=3)$
$(v\geq 1,\ N) \rightarrow (v'=v,\ N'=N+2)$	Same as $(v=0,\ N) \rightarrow (v'=0,\ N'=N+2)$
Rovibrational excitation by proton collisions	
$(v=0,\ N=0) \rightarrow (v'=1\text{–}3,\ N'=0)$	[44]
$(v=1\text{–}5,\ N=0) \rightarrow (v'=v+1,\ N'=0)$	Scaled from cross section for $(v=0,\ N=0) \rightarrow (v'=1,\ N'=0)$ by multiplying ratio of electron collisional excitation cross section for $(v,\ N=0) \rightarrow (v'=v+1,\ N'=0)$ to that for $(v=0,\ N=0) \rightarrow (v'=1,\ N'=0)$ at 4 eV in [45] following procedure adopted in [38]
$(v,\ N) \rightarrow (v'\neq v,\ N'=N\pm 2)$	Same as $(v,\ N) \rightarrow (v',\ N'=N)$
Einstein A coefficient for rovibronic deexcitation	
$(B,\ v',\ N') \rightarrow (X,\ v,\ N=N'\pm 1)$ $(C,\ v',\ N') \rightarrow (X,\ v,\ \lvert N-N'\rvert \leq 1)$ $(B',\ v',\ N') \rightarrow (X,\ v,\ N=N'\pm 1)$ $(D,\ v',\ N') \rightarrow (X,\ v,\ \lvert N-N'\rvert \leq 1)$	[47]
$(D,\ v',\ N') \rightarrow (X,\ v,\ N=N'\pm 1)$ not given by [47]	Scaled from cross section for $(D, v', N') \rightarrow (X, v, N=N')$ by multiplying ratio of Hönl–London factors in [48, 49]

3.4.3 Code Benchmark

The benchmark of the calculation code was carried out using conditions of thermal equilibrium. Since only the electron and proton collisional processes were considered for the rovibrational excitation and deexcitation, T_{vib}^{X} and T_{rot}^{Xv} should converge to the electron/ion temperatures to equalize the excitation and deexcitation fluxes when the calculation is continued for a sufficiently long time. The initial rovibrational population distribution was given by the Boltzmann distribution with $T_{\mathrm{vib}}^{X} = T_{\mathrm{rot}}^{Xv=0} = 1000$ K, and the other parameters were kept constant: $n_{\mathrm{H_2}} = 10^{16}$ m^{-3}, $n_{\mathrm{e}} = 10^{18}$ m^{-3} or $n_{\mathrm{p}} = 10^{18}$ m^{-3}, and $T_{\mathrm{e}} = 10$ eV or $T_{\mathrm{p}} = 10$ eV. The results of the calculation for the model considering the rovibrational excitation are shown in Fig. 3-6. Figs. 3-6(a)–(c) show the results for the model considering only the electron collisional processes, and Figs. 3-6(d)–(f) show those for the model considering only the proton collisional processes. The temporal variation of the rotational population is shown in Figs. 3-6(a) and (d), and that of the vibrational population is shown in Figs. 3-6(b) and (e). The temporal variations of T_{vib}^{X} and $T_{\mathrm{rot}}^{Xv=0}$ are shown by black and green lines, respectively, in Figs. 3-6(c) and (f). Note that the calculations considering only the electron collisions converge more rapidly because of the larger excitation rates. It was confirmed that the vibrational temperature T_{vib}^{X} approached 10 eV, the value of T_{e} or T_{p} set for both models, but $T_{\mathrm{rot}}^{Xv=0}$ approached a temperature lower than 10 eV. The latter is due to the selection rules of $\Delta N = 0$ or 2, and $T_{\mathrm{rot}}^{Xv=0}$ derived for the population densities with odd or even N converged to 10 eV. The model considering the electronic excitation was verified by comparison with the result of a collisional-radiative model [37]. The sum of the populations for *B*, *B′*, *C*, and *D* states was comparable to the population of the e' state.

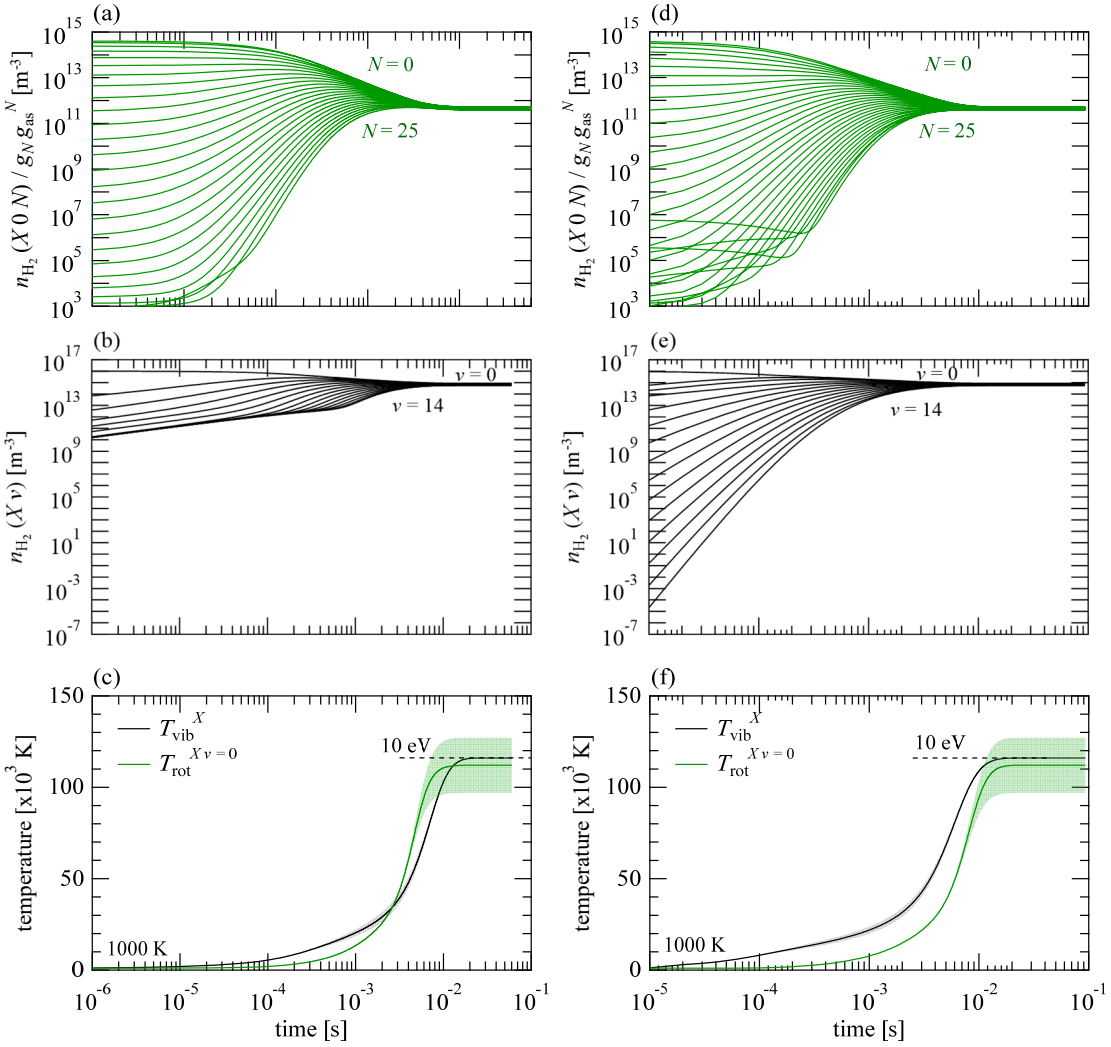

Fig. 3-6. Temporal variations of (a), (d) rotational population divided by the multiplicity, (b), (e) vibrational population, and (c), (f) T_{vib}^{X} (black) and $T_{\mathrm{rot}}^{Xv=0}$ (green) for the model considering the rovibrational excitation. Only the electron collisional processes are considered ($n_{\mathrm{p}} = 0$) in (a)–(c), and only the proton collisional processes are considered ($n_{\mathrm{e}} = 0$) in (d)–(f).

3.4.4 Calculation Results of Collisional Increase in Rotational Temperature

The increase in $T_{\mathrm{rot}}^{Xv=0}$ was calculated for spatially uniform profile of $n_{\mathrm{e}}(l)$, $n_{\mathrm{p}}(l)$, $T_{\mathrm{e}}(l)$, and $T_{\mathrm{p}}(l)$, and the dependences of the increase on the parameters and processes were examined. The results of the calculation are shown in Fig. 3-7. The left and right columns are the results of the model considering the electron and proton collisional processes separately, respectively. The dependences on (a) n_{e}, (b) T_{e}, and (c) T_{wall}, and those on (d) n_{p}, (e) T_{p}, and (f) T_{wall} are shown in Fig. 3-7. The values of the fixed parameters were set to $n_{\mathrm{e}} = 10^{18}$ m^{-3}, $n_{\mathrm{p}} = 10^{18}$ m^{-3}, $T_{\mathrm{e}} = 10$ eV, $T_{\mathrm{p}} = 10$ eV, and $T_{\mathrm{wall}} = 500$ K. The increase in $T_{\mathrm{rot}}^{Xv=0}$ is mostly sensitive and nearly proportional to n_{e} and n_{p}. The effect of T_{e} is small, which originates from small variations of the cross sections for $T_{\mathrm{e}} \geq 5$ eV. For the proton collisional processes, the cross sections for pure rotational excitation are more than 10 times larger than those for vibrational excitation when $T_{\mathrm{p}} \leq 10$ eV, and this results in the different effect of T_{p} when $T_{\mathrm{p}} \leq 10$ eV from that when $T_{\mathrm{p}} > 10$ eV. The increase in $T_{\mathrm{rot}}^{Xv=0}$ due to the collisional processes is also insensitive to the value of T_{wall}.

The effect of the processes on $T_{\mathrm{rot}}^{Xv=0}$ was compared for n_{e} and/or $n_{\mathrm{p}} = 10^{18}$–10^{20} m^{-3}. Fig. 3-8 shows the dependences of the calculated $T_{\mathrm{rot}}^{Xv=0}$ at $l = 10$ mm on n_{e} and n_{p}. The colors of the lines represent the results of the model considering the electron collision (blue), the proton collision (red), and both collisions (purple). The solid, dashed, and chain lines show the results of the model considering the rotational (Rot), rovibrational (wVib), and rovibronic (wEle) excitations and deexcitations, respectively. Among these reactions, the rovibronic and rovibrational transitions affect the increase in $T_{\mathrm{rot}}^{Xv=0}$ when the density exceeds 10^{19} m^{-3}.

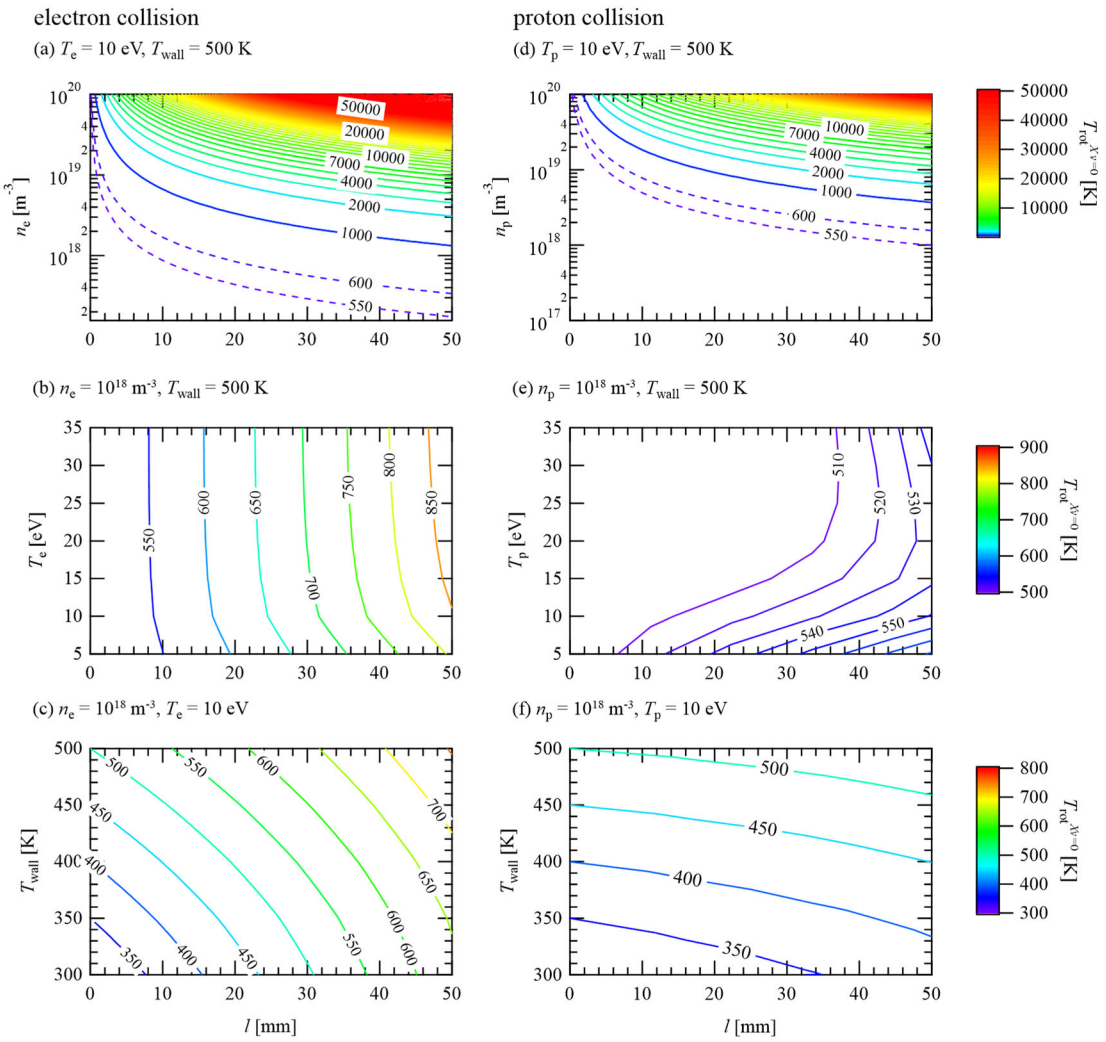

Fig. 3-7. Dependences of calculated $T_{rot}^{Xv=0}$ on (a) n_e, (b) T_e, and (c) T_{wall} and l for the model considering electron collisional processes ($n_p = 0$), and the dependences on (d) n_p, (e) T_p, and (f) T_{wall} and l for the model considering proton collisional processes ($n_e = 0$). The same color scale is used for the figures in the same row.

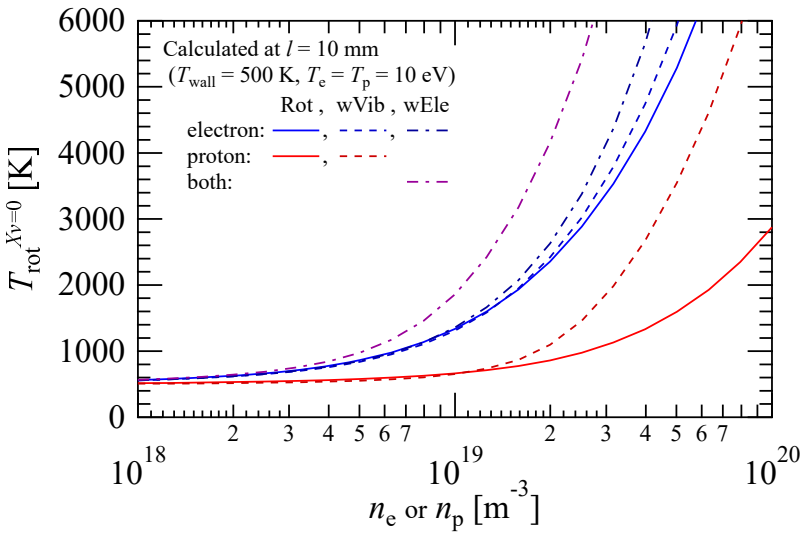

Fig. 3-8. Comparison of n_e and n_p dependences at distance l = 10 mm. The colors of the lines show the calculation results using the model considering the electron collision (blue), the proton collision (red), and both collisions (purple). The solid, dashed, and chain lines show the calculation results using the model considering only rotational, rovibrational, and rovibronic excitations, respectively.

3.5 Conclusion

The collisional increase in the rotational temperature of hydrogen molecules in tokamak edge plasmas was modeled using rate equations considering electron and proton collisional excitation and deexcitation and spontaneous emission from the electronic excited state to the ground state. The calculation using this model shows a nearly linear increase in $T_{rot}^{Xv=0}$ with n_e, n_p, and l. The other parameters, T_e, T_p, and T_{wall}, have no significant effect on the collisional increase in $T_{rot}^{Xv=0}$. By separately considering different processes in the calculations, it was shown that the electronic and vibrational transitions affect $T_{rot}^{Xv=0}$ when n_e or n_p exceeds 10^{19} m^{-3}. The measurements of n_e, n_p, and l are therefore required for the evaluation of the collisional increase in $T_{rot}^{Xv=0}$, and the model considering only pure rotational transitions is sufficient for the evaluation when n_e and n_p are less than 10^{19} m^{-3}.

4 Thermometry of Plasma-Facing Surface using Rotational Temperature of Hydrogen Molecules

Understanding collisional increase in rotational temperature of hydrogen molecules is required for the development of surface thermometry via Fulcher-α band spectroscopy. In the previous chapter, the electron and proton collisions and spontaneous emission that affect the increase in rotational temperature were evaluated, and a model including these processes was constructed. In this chapter, measurements of the rotational temperature in three tokamaks are reported. Then, the rotational temperature at the desorption location is deduced by evaluating the effect of the collisional increase using the model developed in Chapter 3.

4.1 Experimental Setup

4.1.1 Experimental Devices

The rotational temperature of hydrogen molecules was measured in three tokamaks: QUEST, LTX-β, and DIII-D. Their schematic illustrations are shown in Fig. 4-1. QUEST (Q-shu University Experiment with Steady-State Spherical Tokamak) is a spherical tokamak at Research Institute for Applied Mechanics, Kyushu University, whose major and minor radii are 0.64 and 0.46 m, respectively. LTX-β (Lithium Tokamak Experiment Beta) is a spherical tokamak at the Princeton Plasma Physics Laboratory, USA, whose major and minor radii are 0.40 and 0.26 m, respectively. DIII-D (Doublet III-D) is a tokamak at General Atomics in San Diego, USA, whose major and minor radii are 1.7 and 0.6 m, respectively.

A tokamak device consists of a vacuum vessel and three types of magnetic field coil: toroidal field, poloidal field, and central solenoid coils, as shown in Fig. 4-1 and in the poloidal cross-sectional views of the devices in Fig. 4-2. QUEST has eight toroidal field coils with a total of 16 turns (see Fig. 4-1(a)) and four pairs of poloidal field coils. The poloidal field and central solenoid coils are shown by the blue and gray boxes, respectively, in Fig. 4-2(a). The vacuum vessel and plasma-facing components are made of stainless steel. The plasma facing-components, called “hot walls”, are coated with atmospheric-plasma-sprayed tungsten (APS-W) and have heaters to control the surface

temperature [50]. LTX-β has 16 toroidal field coils with a total of 128 turns, shown in gray, and six pairs of poloidal field coils called yellow, green, orange, blue, red, and internal (purple) coils, shown with the corresponding colors in Fig. 4-2(b) [51]. The central solenoid coil is shown by the shaded box in Fig. 4-2(b). The plasma-facing components, called "shells", are in the vacuum vessel, are made of 1-inch-thick copper clad with stainless steel on the plasma-facing side and are conformal with the last closed flux surface (LCFS). The lithium plasma-facing surfaces are provided by coating lithium on the shells using evaporators at two toroidal locations, and the heaters on the shells enable the liquid lithium surface to be maintained. DIII-D has 24 toroidal field coils with a total of 144 turns, 18 poloidal field coils, and a central solenoid coil (see Figs. 4-1(c) and 4-2(c)). The vacuum vessel is made of Inconel and armored with ATJ graphite or carbon fiber composite tiles. Most of the plasma-facing components are ATJ graphite, and carbon fiber composite tiles are used for particularly demanding applications [52].

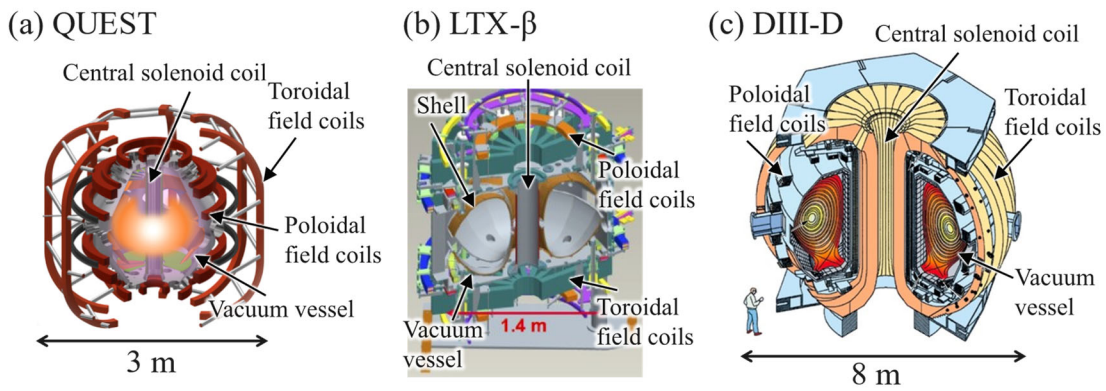

Fig. 4-1. Schematic illustrations of (a) QUEST, (b) LTX-β, and (c) DIII-D [53].

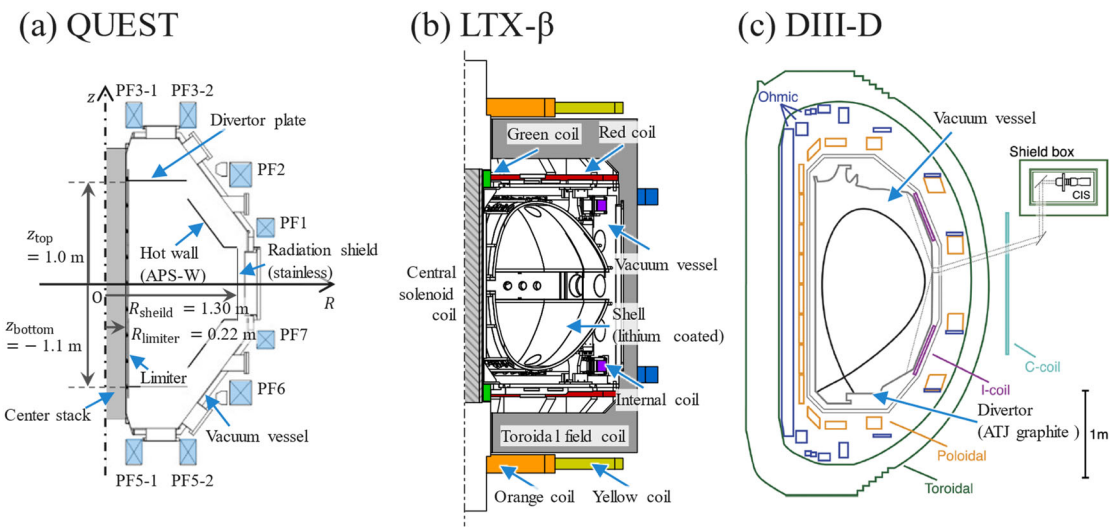

Fig. 4-2. Poloidal cross sections of (a) QUEST, (b) LTX-β, and (c) DIII-D [54]. Toroidal coils are shown in gray in (b) and in green in (c). Poloidal coils are shown by blue boxes in (a), in colors corresponding to their name in (b), and by orange boxes in (c). The central solenoid coil is in the center stack, shown by gray box in (a), shaded box in (b), and blue boxes in (c). For QUEST, hot walls and radiation shields are in the vessel and made of atmospheric-plasma-sprayed tungsten (APS-W) and stainless steel, respectively. The hot walls have heaters to control the wall temperature. For LTX-β, shells are plasma-facing components, are made of 1-inch-thick copper clad with stainless steel on the plasma-facing side, and are coated with lithium. They have heaters to provide a liquid lithium surface. For DIII-D, the divertor target is made of ATJ graphite, and the surface temperature is changed by heat from the plasma.

4.1.2 Plasma Discharges

The temporal evolutions of the parameters for typical discharges used in this work are shown for the three devices in Fig. 4-3. The magnetic equilibria of these plasmas are shown by contour plots in Fig. 4-4, and thick gray lines show the LCFSs. The LCFSs are tangential to the wall in QUEST and LTX-β, known as a limiter configuration. In DIII-D, a divertor configuration is employed. For all the devices, the toroidal magnetic field is generated by the toroidal field coils and was kept almost constant as shown in the first row of Fig. 4-3. In QUEST, the plasma current was driven by a 28 GHz microwave (electron cyclotron resonance heating: ECH) and the superposition of the vertical magnetic field by poloidal field coils [55]. The temporal evolutions of the poloidal field coils currents and the power meter for the ECH system are shown in the second and third rows of Fig. 4-3(a), respectively. In LTX-β, the plasma current is induced by changing currents of the central solenoid coil, and the plasma shape is controlled by the poloidal field coils (see the third and second rows of Fig. 4-3(b), respectively). In DIII-D, the plasma current was driven by the ohmic solenoid and neutral beam injection (NBI), as shown in the third row of Fig. 4-3(c). The second row of Fig. 4-3(c) shows the radial position of the outer strike point, which is the intersection of the separatrix and divertor target plate, and shows the temporal evolution of the magnetic configuration.

The surface temperatures of the plasma-facing components were measured with thermocouples in QUEST and LTX-β and by IR thermography in DIII-D. In QUEST and LTX-β, the spatial variation of the surface temperature is expected to be small, because they were heated for a sufficiently long time to make the distribution of the surface temperature uniform and because the heat fluxes from plasmas are small. Thus, the temperatures measured with thermocouples were regarded as those at the measurement points of the rotational temperatures. In DIII-D, the surface temperatures measured by IR thermography were used because the change in the emissivity, the radiation intensity ratio to the black body, is expected to be small. In QUEST, four thermocouples on the hot walls were used, as shown by blue diamonds in Fig. 4-4(a). Two thermocouples were used in LTX-β and were mounted in the stainless steel tubes which are welded to the shell, are on the outboard side, and are exposed to plasma. In DIII-D, the spatial distribution of the surface temperature of the lower divertor

target plate was measured with an IR camera directed at the lower divertor. The field of view is shown in blue in Fig. 4-4(c).

The electron density and temperature were measured with probes and/or by Thomson scattering. In QUEST, the radial profiles of n_e and T_e were measured in the outboard midplane by Thomson scattering [56], and the measurement positions are shown by green squares in Fig. 4-4(a). In LTX-β, a probe on the inboard side of the shells was used, which is shown by red circle in Fig. 4-4(b). In DIII-D, both methods were used, and the measurement positions of probes and Thomson scattering are shown by red circles and green squares, respectively in Fig. 4-4(c). Materials of the plasma-facing components, the surface temperature, and the plasma parameters are summarized in Table 4-1.

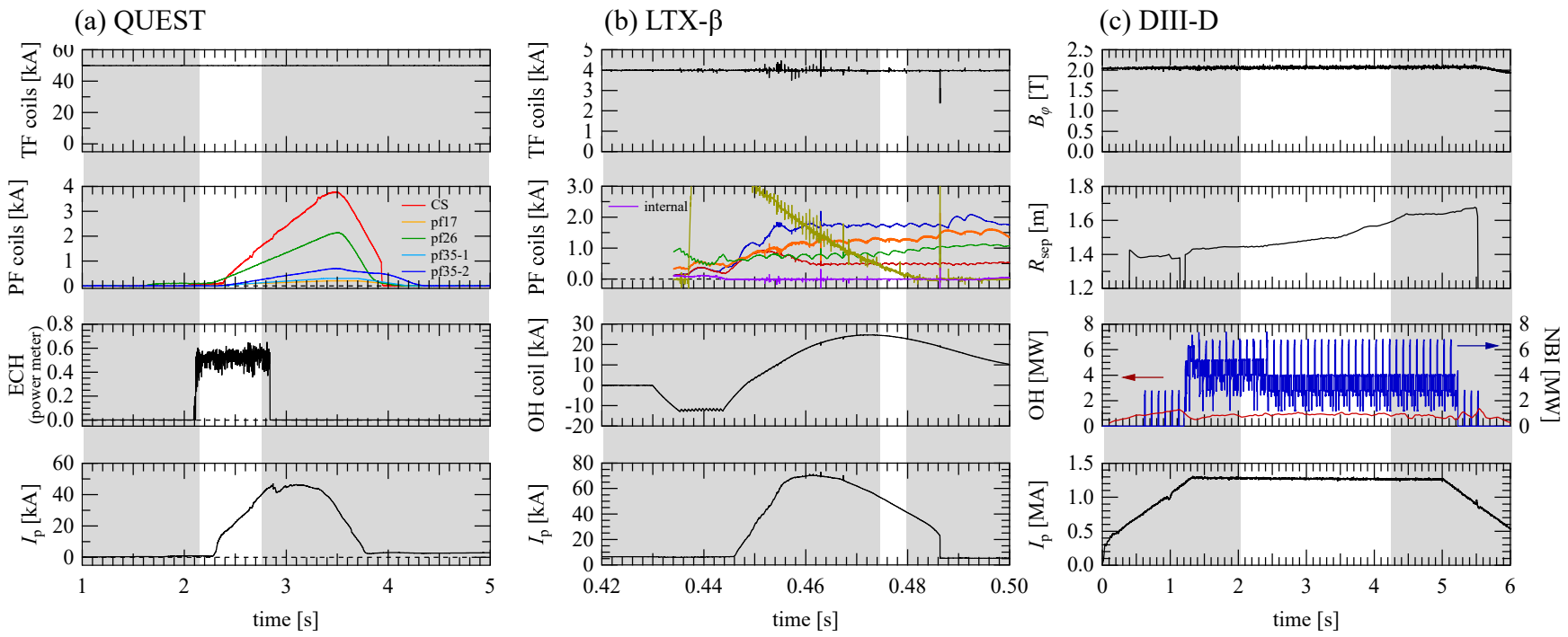

Fig. 4-3. Temporal evolutions of discharge parameters for (a) QUEST, (b) LTX-β, and (c) DIII-D. Unshaded areas show the times when the spectroscopic data was taken. (First row) Toroidal field coil currents (TF coils) or toroidal field (B_φ). (Second row) Poloidal field coil currents (PF coils) or radial position of outer strike point (R_{sep}). The colors of the lines for (b) correspond to the names of the coils. (Third row) Heating power. The signal of power meter for ECH system, the current of the central solenoid coil used for ohmic heating (OH), and the power of ohmic heating and neutral beam injection (NBI) are shown for (a), (b), and (c), respectively. (Bottom row) plasma current I_p.

Table 4-1. Discharge parameters for QUEST, LTX-β, and DIII-D. n_e and T_e are the electron density and temperature, respectively, in edge plasmas. Values of proton density n_p and temperature T_p, atomic density n_H, and molecular density n_{H_2} were used for the calculation using the model described in Chapter 3. l is the position or range of Fulcher-α band emission.

	QUEST	**LTX-β**	**DIII-D**
Shot numbers	#43773, #43774, #43776, #43935, #43942, #43945	#101749, #101763, #101865	#183555, #183557, #183558, #183561
Plasma-facing surface	Atmospheric-plasma-sprayed tungsten (APS-W) Stainless steel	Lithium (solid and liquid)	ATJ graphite Carbon fiber composite
T_{wall} [K]	370, 468	297, 466	400–500
n_e [$\times 10^{18}$ m^{-3}]	$\leq$ 0.4	0.2–1.2	10–100
T_e [eV]	5	20	10–20
n_p [m^{-3}]	$= n_e$ (assumption)	$= n_e$ (assumption)	$= n_e$ (assumption)
T_p [eV]	$= T_e/2$ (empirical scaling from results in Chapter 5)	$= T_e/2$ (empirical scaling in QUEST)	$= T_e$ (simulation for D_2 [57])
n_H [m^{-3}]	2×10^{16} (measurement with ionization gauge)	2×10^{16} (based on measurements in QUEST)	2×10^{19} (simulation for D_2 [57, 58])
n_{H_2} [m^{-3}]	10^{16} (measurement with ionization gauge)	10^{16} (based on measurements in QUEST)	10^{19} (simulation for D_2 [57, 58])
l [m]	0.38–0.57	0.03	0.01 (measured for D_2)

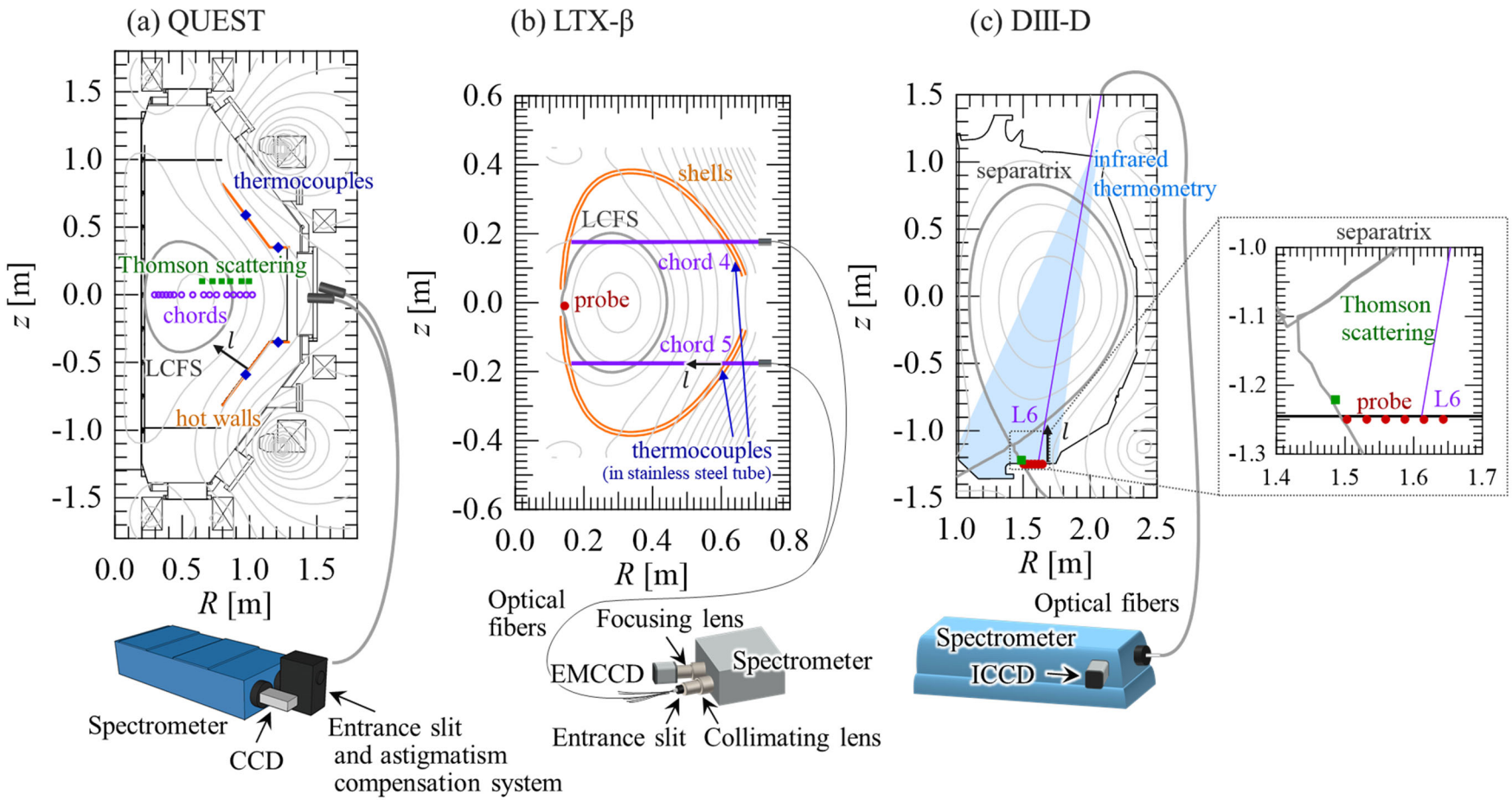

Fig. 4-4. Magnetic equilibria and the spectroscopic systems used for (a) QUEST, (b) LTX-β, and (c) DIII-D. Viewing chords are shown in purple. The measurement positions of Thomson scattering and probes are shown by green squares and red circles, respectively. Note that the green squares in (a) are shifted upward to avoid overlap with the other markers.

4.1.3 Spectroscopic System

For the measurement of the rotational temperature of hydrogen molecules, the emission from plasmas was collected by using optical fibers and lenses, and dispersed by using a spectrometer. Fig. 4-4 shows schematic illustrations of the spectroscopic systems used to measure the Fulcher-α emission lines of hydrogen molecules (600–608 nm) in the three devices. Each spectroscopic system consists of optical fibers, a spectrometer, and a CCD camera. The optical fibers were used with collimators and emission collected from plasmas. The collected emission entered the spectrometer through an entrance slit, and the dispersed spectra were recorded on the CCD camera.

For QUEST, 16 optical fibers from two optical fiber bundles were used. Each optical fiber bundle consisted of 15 optical fibers with a core diameter of 0.25 mm and was used with an achromatic lens (Edmund Optics, TS achromatic lens 15x15 MGF2; 15 mm focal length, 14 mm diameter). The fibers were connected to a Czerny–Turner spectrometer (Acton Research, AM-510; 1 m focal length, F/8.7, 1800 grooves/mm grating), and the spectra were recorded on a CCD camera (Andor Technology, DU440-BU2; 2048 × 512 pixels and 13.5 μm square pixels).

For LTX-β, two optical fibers with a core diameter of 0.6 mm were used with reflective collimators (Thorlabs, RC04SMA-F01; 15 mm focal length, clear aperture of 11 mm diameter). The optical fibers were connected to a lens-based spectrometer [59] that consisted of two camera lenses for collimating and focusing (Canon 200 mm f/1.8 EF) and a grating with 2160 grooves/mm. An electron-multiplying CCD camera (Princeton Instruments, ProEM 512; 512 × 512 pixels and 16 μm square pixels) was used to record the spectra [59].

For DIII-D, six optical fibers, part of the Multi-chord Divertor Spectrometer (MDS) system [60], with a core diameter of 0.6 mm were set with a lens to observe emission near the divertor, and one of them was used. The fibers were connected to a Czerny–Turner spectrometer (McPherson Corporation, Model 209; 1.33 m focal length, F/11.6, and 1200 grooves/mm grating) [60]. The dispersed spectra were recorded on an intensified CCD camera (Princeton Instruments, PI-MAX4 1024i; 1024 × 1024 pixels and 12.8 μm square pixels).

The viewing chords are shown in purple with the poloidal cross-sectional views of the devices in Fig. 4-4. In QUEST, the viewing chords were aligned on the midplane, and the distances of the viewing chords from the center of the device η are shown by purple markers. The diameters of the viewing chords were approximately 30 mm at the point where the distance from the center of the vessel is shortest. In LTX-β, two viewing chords were aligned horizontally to observe the emission from hydrogen molecules near the inboard side of the shells. The diameters of the viewing chords were approximately 30 mm on the shells. In DIII-D, the viewing chord named L6, which is shown by a purple line, was used. The diameter of the viewing chord was approximately 20 mm on the divertor.

Since the CCD cameras record the intensity of each pixel, calibration processes are required to convert the position of each pixel and the recorded intensity into the wavelength and radiometric quantity, respectively. The wavelength was calibrated by using known emission lines from a lamp. For the systems in QUEST and LTX-β, a He–Ne discharge tube and a mercury and neon lamp were used, respectively. For the system in DIII-D, the relationship between the wavelength and the pixels was derived from a measurement of spectra from a lamp. Sensitivity was calibrated by using a light source with known radiometric quantities. A xenon standard lamp (Hamamatsu Photonics, L7810-02) and a diffuse reflectance plate (Labsphere, SRT-99-050) were used for the system in QUEST. A uniform radiance source (Labsphere, Helios) was used for the system in LTX-β. For the system in DIII-D, a uniform radiance source (Optronics) was used.

The dispersed spectrum has a broadened profile even when monochromatic light enters a spectroscopic system. This profile is called an instrumental function. The instrumental functions of the systems were regarded as Gaussian functions, and their FWHMs were approximately 0.07, 0.07, and 0.04 nm for the systems in QUEST, LTX-β, and DIII-D, respectively.

In QUEST, the measurements were conducted at $T_{\mathrm{wall}} = 370$ and 468 K with the other parameters fixed. In LTX-β, the spectra were measured at $T_{\mathrm{wall}} = 297$ and 466 K, below and above the melting point of lithium of 453.65 K. The dependence of $T_{\mathrm{rot}}^{Xv=0}$ on n_{e} was also observed by changing n_{e} temporally. The electron temperature T_{e} was nearly constant. In DIII-D, T_{wall}, n_{e}, and T_{e} were varied temporally, and the ranges of the values are shown in Table 4-1.

4.2 Experimental Results

4.2.1 Fulcher-α Band Emission Spectra of Hydrogen Molecule

The Fulcher-α band consists of lines produced by the transition from the $d\,^3\Pi_u$ state to the $a\,^3\Sigma_g^+$ state, and the transition contains those between various rovibrational states. The vibrational and rotational states of the upper states are represented with the quantum numbers v' and N', and those of the lower states are represented with v'' and N'', respectively. In particular, the transition between the same rotational states, *i.e.*, $N' = N''$, is called the Q-branch, and those for $N' = N'' = 1, 2, 3\ldots$ are denoted as Q1, Q2, Q3…, respectively. The calculated Q-branch spectra of four vibrational bands ($v' = v'' = 0, 1, 2, 3$) for $T_{\mathrm{vib}}^{d} = 5000$ K and $T_{\mathrm{rot}}^{dv'} = 500$ K (corresponding to $T_{\mathrm{rot}}^{Xv=0} = 1000$ K) are shown in Fig. 4-5. The FWHM of the spectra was set at 0.05 and 10 nm for Figs. 4-5(a) and (b), respectively. In the former case, each rotational line is resolved as shown in Fig. 4-5(a). On the other hand, in the latter case, each rotational line is not resolved and rotational lines belonging to different vibrational bands are superposed as shown in Fig. 4-5(b). Therefore, a wavelength resolution of ~ 0.05 nm is required for the measurement of the rotational temperature.

The Q-branch rotational lines belonging to vibrational band $v' = v'' = 0$ were measured in the three devices. The measured spectra and their central wavelengths are respectively shown by black markers and blue vertical lines in Fig. 4-6. The latter were identified using a data table [61].

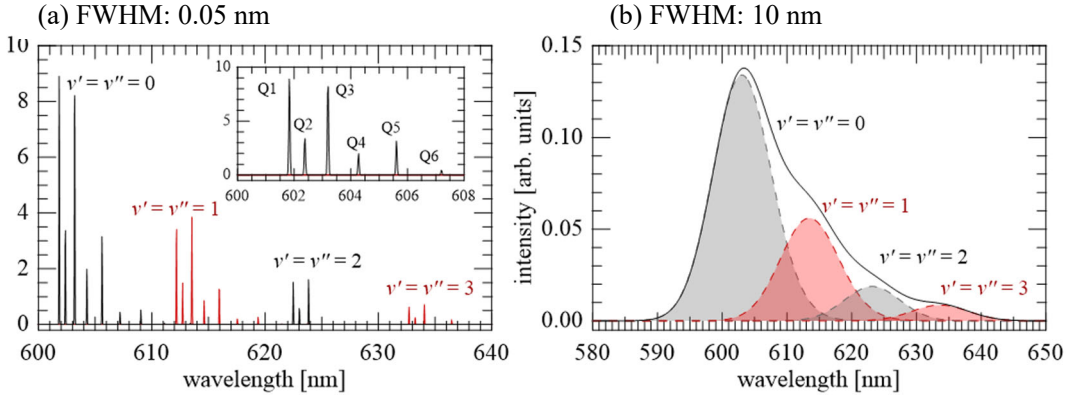

Fig. 4-5. Fulcher-α band spectra calculated for $T_{\mathrm{vib}}^{d} = 5000$ K and $T_{\mathrm{rot}}^{dv'} = 500$ K (corresponding to $T_{\mathrm{rot}}^{Xv=0} = 1000$ K), and the FWHM of the spectra set at (a) 0.05 nm and (b) 10 nm. Up to seven lines of Q-branches are plotted for four vibrational bands ($v' = v'' = 0, 1, 2, 3$). The inset of (a) shows an enlarged view of vibrational band $v' = v'' = 0$. The shaded regions with dashed lines in (b) show the spectra for each vibrational band and the solid line in (b) shows the sum of the vibrational bands.

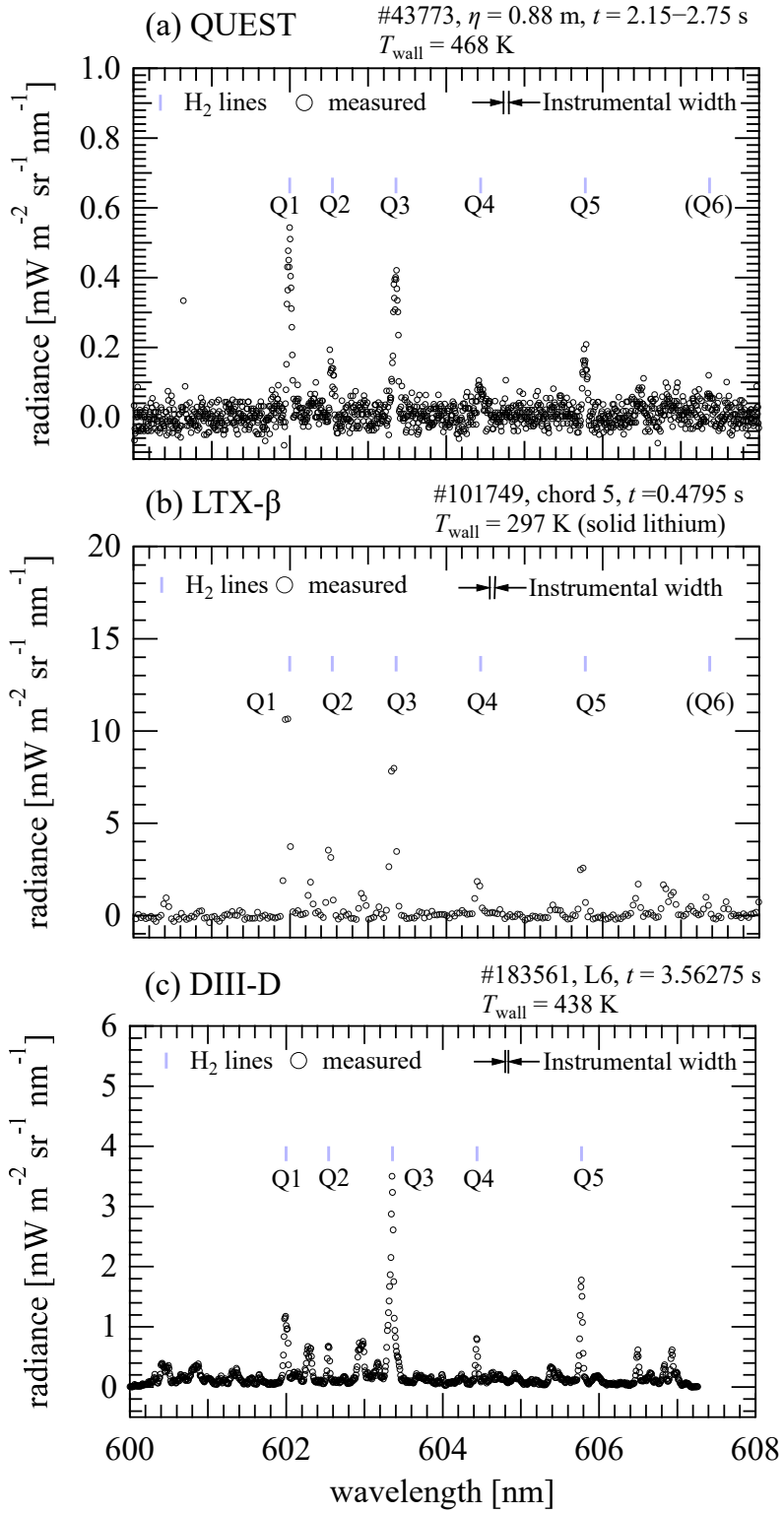

Fig. 4-6. Spectra measured in (a) QUEST, (b) LTX-β, and (c) DIII-D. Black markers and vertical blue lines show the measured spectra and the central wavelength for the lines of the Fulcher-α band (Q-branch, $v' = v'' = 0$), respectively.

4.2.2 Evaluation of Rotational Temperature

The rotational temperature was estimated from the relative intensity of the measured spectra using the coronal model. The Einstein A coefficient for Fulcher-α band $A(dv'N', av''N'')$ is expressed as

$$A(dv'N', av''N'') = \frac{16\pi^3\nu^3}{3\varepsilon_0 hc^3}|R_e|^2 q_{v'v''}\frac{S_{N'N''}}{g_{N'}}, \tag{4-1}$$

where ε_0 is the permittivity, ν is the frequency of transition, R_e is the electronic transition moment, $q_{v'v''}$ is the Franck–Condon factor, $S_{N'N''}$ is the Hönl–London factor, and $g_{N'}$ is the multiplicity of the rotational state. The Hönl–London factor $S_{N'N''}$ is given by $(2N'+1)/2$ for the Q-branch of the Fulcher-α band, and $g_{N'}$ is $(2N'+1)$ [48, 49]. When the rotational population distribution of the upper state $n(dv'N')$ is given by the Boltzmann distribution with $T_{\mathrm{rot}}^{d\,v'=0}$, $n(dv'N')$ follows the relation shown by Eq. (3-2). In other words, $n(dv'N')$ can be expressed as

$$\ln\left[\frac{n(dv'N')}{g_{N'}g_{as}^{N'}}\right] = -\frac{F_d(v',N')}{k_B T_{\mathrm{rot}}^{dv'}} + \text{const.} \tag{4-2}$$

The measured emissivity of each line is divided by $g_{N'}g_{as}^{N'}$ and $S_{N'N''}/g_{N'}$ with the latter being a component of the Einstein A coefficient and depends on the rotational state. The rotational temperature for the *d* state can be obtained from the slope of the logarithmic plot on the left-hand side of Eq. (4-2) versus the rotational energy $F_d(v',N')$. This plot is called a Boltzmann plot.

The population distribution for $v'=0$ and $N'=1$–5 states of the *d* state is derived from the emissivity of the rotational line spectra using Eq. (2-5). In QUEST, the radial profiles of Q1–Q5 line emissivities were evaluated assuming their toroidal symmetry. Firstly, the measured Q1–Q5 line spectra were fitted to Gaussian functions as shown by the magenta line in Fig. 4-7(a), and the chord-integrated radiance I_A of each line was derived. The measured I_A values are plotted versus the tangency radius of the viewing chord η and are shown by markers in Fig. 4-9(a). Then, their continuous η-directional profiles were evaluated by fitting to sigmoid functions, which well reproduce the η-dependence of the measured I_A in the region of interest $\eta > 0.7$ m. The fitted I_A profiles are shown by lines in Fig. 4-9(a). Next, the radial profiles of emissivity were derived from the fitted I_A profiles by Abel inversion:

$$\varepsilon(R) = -\frac{1}{\pi}\int_{R}^{R_{\mathrm{end}}} \frac{1}{\sqrt{\eta^2 - R^2}} \frac{dI_{\mathrm{A}}(\eta)}{d\eta} d\eta, \tag{4-3}$$

where ε, I_{A}, and R_{end} are the emissivity, measured radiance, and outer boundary of the emission, respectively (see Fig. 5-12). Lastly, the radial population distribution of the *d* state was derived from the emissivity profile. For the spectra measured in LTX-β and DIII-D, the emissivities of Q1–Q5 lines were evaluated assuming single point emissions because the Fulcher-α emission is localized near the plasma-facing walls owing to larger spatial gradients of n_{e} and T_{e}. The Q1–Q5 line spectra measured in LTX-β were fitted to Gaussian functions as shown by the magenta line in Fig. 4-7(b). For the spectra measured in DIII-D, Zeeman splitting was observed in the Q1 line spectrum (Fig. 4-8(a)) because of the magnetic field (~2 T) being larger than that of the other two devices, and a symmetric triple Gaussian function was used to approximate the spectrum. Additionally, the Q3 line spectrum overlapped with the other lines, one of which was a hydrogen molecular line at 603.1465 nm. Three overlapping lines were assumed, and the Q3 line spectrum was separated as shown in Fig. 4-8(b). The other line spectra were fitted to Gaussian functions as shown by magenta line in Fig. 4-7(c).

The localization of the Fulcher-α emission in LTX-β and DIII-D was confirmed by wavelength-filtered camera images. In LTX-β, the wavelength-integrated irradiance at $z = -0.176$ m, corresponding to the height of the viewing chord, was evaluated from the camera image (Fig. 4-10(a)) as shown in Fig. 4-10(b). The irradiance is localized and peaks near the wall. Since the peak position of the emissivity was expected to be ≈ 30 mm (≈ 10 px) away from the shell surface, the Fulcher-α emission was approximated as a point source at a distance of 0.03 m from the shell surface. In DIII-D, the emissivity distribution in a poloidal plane was reconstructed from the camera image as shown in Fig. 4-11(a). The emissivity profile along the adopted viewing chord (L6) as a function of z was calculated as shown in Fig. 4-11(b). The reconstructed emissivity is localized near the outer target plate, and the Fulcher-α emission was approximated as a point emission at a distance of 0.01 m from the surface of the target plate, where the emissivity has a peak.

The rotational temperature for the *d* state was derived from the relative intensities of the Q1–Q5 lines. Fig. 4-12 shows examples of Boltzmann plots for the three devices. The measured values (markers) were fitted to the black line, and the rotational temperature $T_{\mathrm{rot}}^{d\,v'=0}$ was estimated from the

slope of the fitted line. The estimated $T_{\mathrm{rot}}^{dv'=0}$ was converted to $T_{\mathrm{rot}}^{Xv=0}$ assuming the following three conditions [62]:

- The rotational population distribution of the electronic and vibrational ground state $n(X0N)$ is given by the Boltzmann distribution.
- The coronal model is applicable to the *d* state.
- No change in rotational state occurs through the electron collisional excitation from the *X* state to the *d* state $(N = N')$, and the excitation cross sections are equal for all the rotational states.

Note that the last assumption agrees with $|\Delta N| \leq 1$ for the electronic excitation processes assumed in Chapter 3, since the transition with $|\Delta N| = 1$ is forbidden between the *X* state and the $d\ ^3\Pi_u^-$ state, which is the upper state for Q-branches of the Fulcher-α band. Thus, the population distribution of the *d* state is expressed as

$$n(dv'N) \propto n(X0N) = C_{Xv=0}\, g_N g_{\mathrm{as}}^N \exp\left[-\frac{F_X(0,N)}{k_{\mathrm{B}} T_{\mathrm{rot}}^{Xv=0}}\right], \tag{4-4}$$

and the distribution $n(dv'N)$ also follows the Boltzmann distribution. This leads to the following relation:

$$T_{\mathrm{rot}}^{dv'=0} = \frac{F_d(0,N)}{F_X(0,N)} T_{\mathrm{rot}}^{Xv=0} = \frac{B_{v'=0}(d)}{B_{v=0}(X)} T_{\mathrm{rot}}^{Xv=0}, \tag{4-5}$$

where the rotational energy $F_X(v,N) \approx B_v\, N(N+1)$ is assumed, and $B_v(X)$ and $B_{v'}(d)$ are the rotational constants for the *X* and *d* states, respectively. The ratio of the rotational constants $B_{v'=0}(d)/B_{v=0}(X)$ is approximately 0.5 [33].

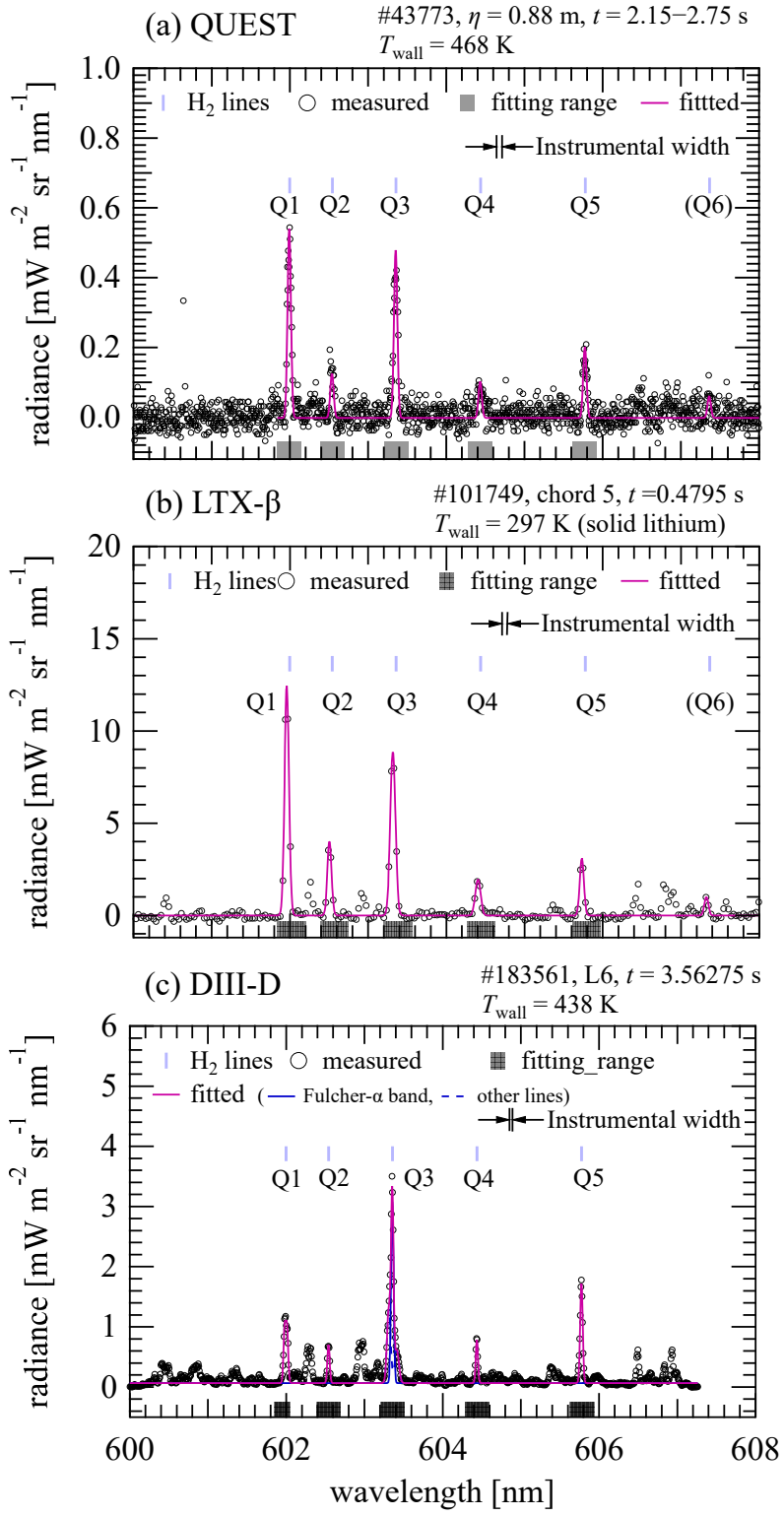

Fig. 4-7. Fitting of spectra measured in (a) QUEST, (b) LTX-β, and (c) DIII-D. Black markers and magenta lines show the measured spectra and those fitted to Gaussian functions, respectively. Gray boxes show the fitting range. For the Q3 line of DIII-D, the three overlapping lines were assumed to separate the Q3 line spectrum (see Fig. 4-8). Blue solid and dashed lines show the separated Q3 line spectrum and the other line spectra, respectively.

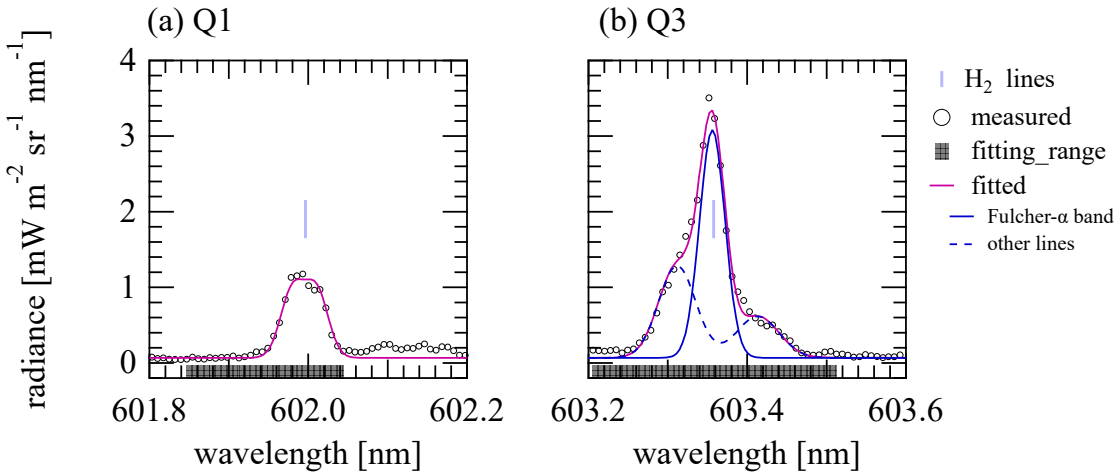

Fig. 4-8. Enlarged spectra near the central wavelength of (a) Q1 and (b) Q3 lines measured in DIII-D. For Q1 line, broadening by Zeeman splitting was observed. For Q3 line, the three overlapping lines were separated by fitting to a triple Gaussian function. The separated Q3 line spectrum and the other line spectra are shown by blue solid and dashed lines, respectively.

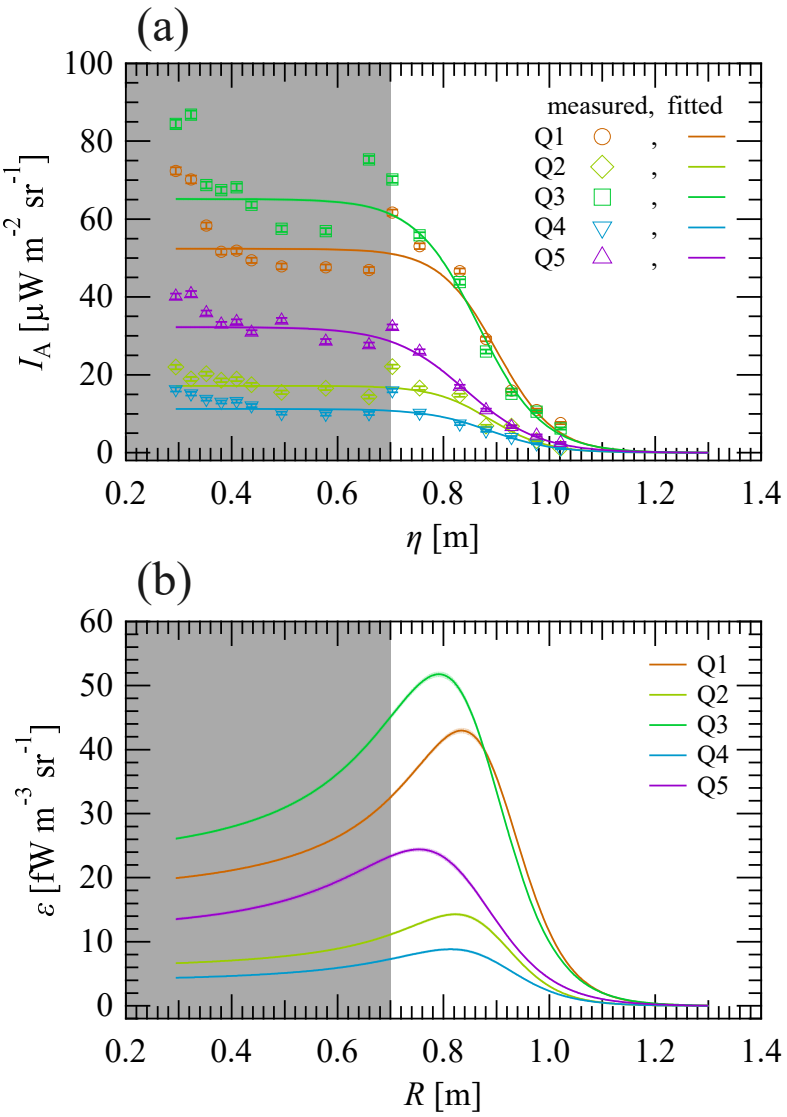

Fig. 4-9. (a) Chord-integrated radiance I_A and (b) emissivity ε of the Q1–Q5 lines evaluated from the spectra measured in QUEST. The data in the shaded ranges was not used for the analysis.

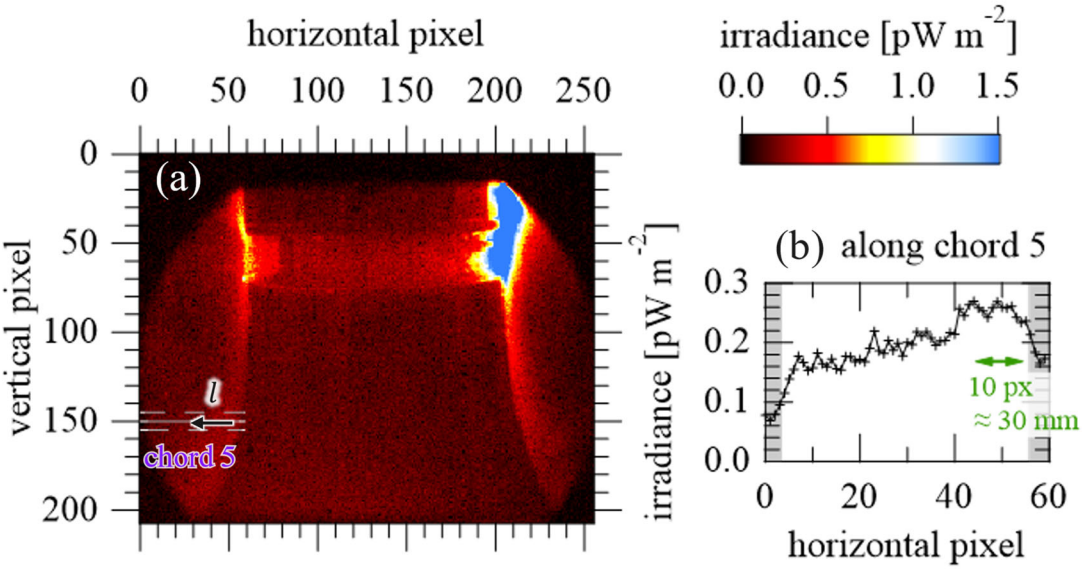

Fig. 4-10. (a) Irradiance distribution of Fulcher-α band measured in LTX-β with a wavelength-filtered camera (602.36 nm central wavelength and 2.43 nm FWHM) for T_{wall} = 297 K (solid lithium surface). (b) Irradiance distribution along chord 5, the horizontal solid line shown in (a), considering the width of the chord shown by the horizontal dashed lines. The viewing chords in the range of 0–3 horizontal pixels are disturbed by the edge of the window and those in the range of 56–60 horizontal pixels are terminated by the center stack.

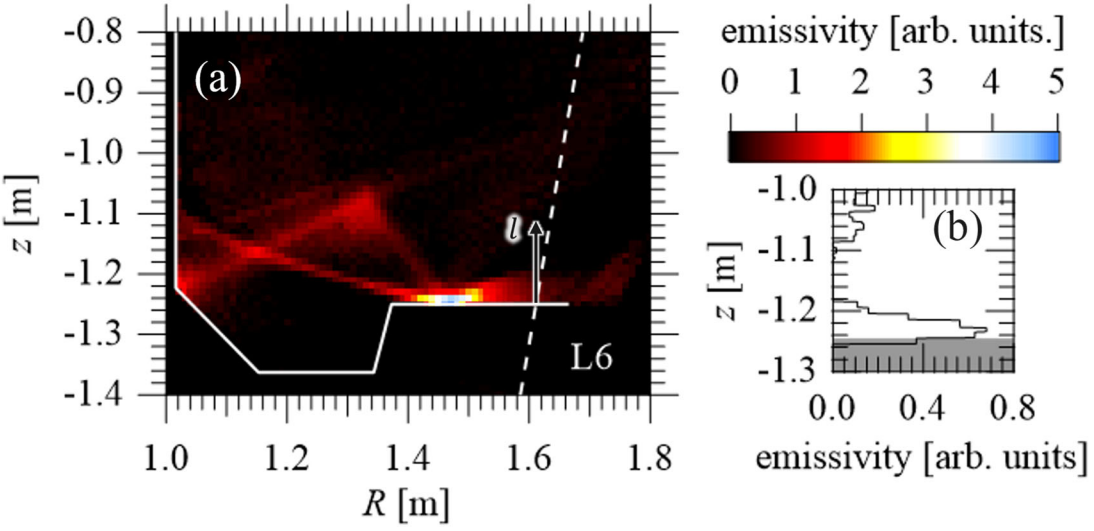

Fig. 4-11. (a) Emissivity distribution of Fulcher-α band obtained in DIII-D from inversion of a wavelength-filtered camera image (601.8 nm central wavelength and 2.8 nm FWHM). (b) Emissivity distribution along viewing chord L6 as a function of z.

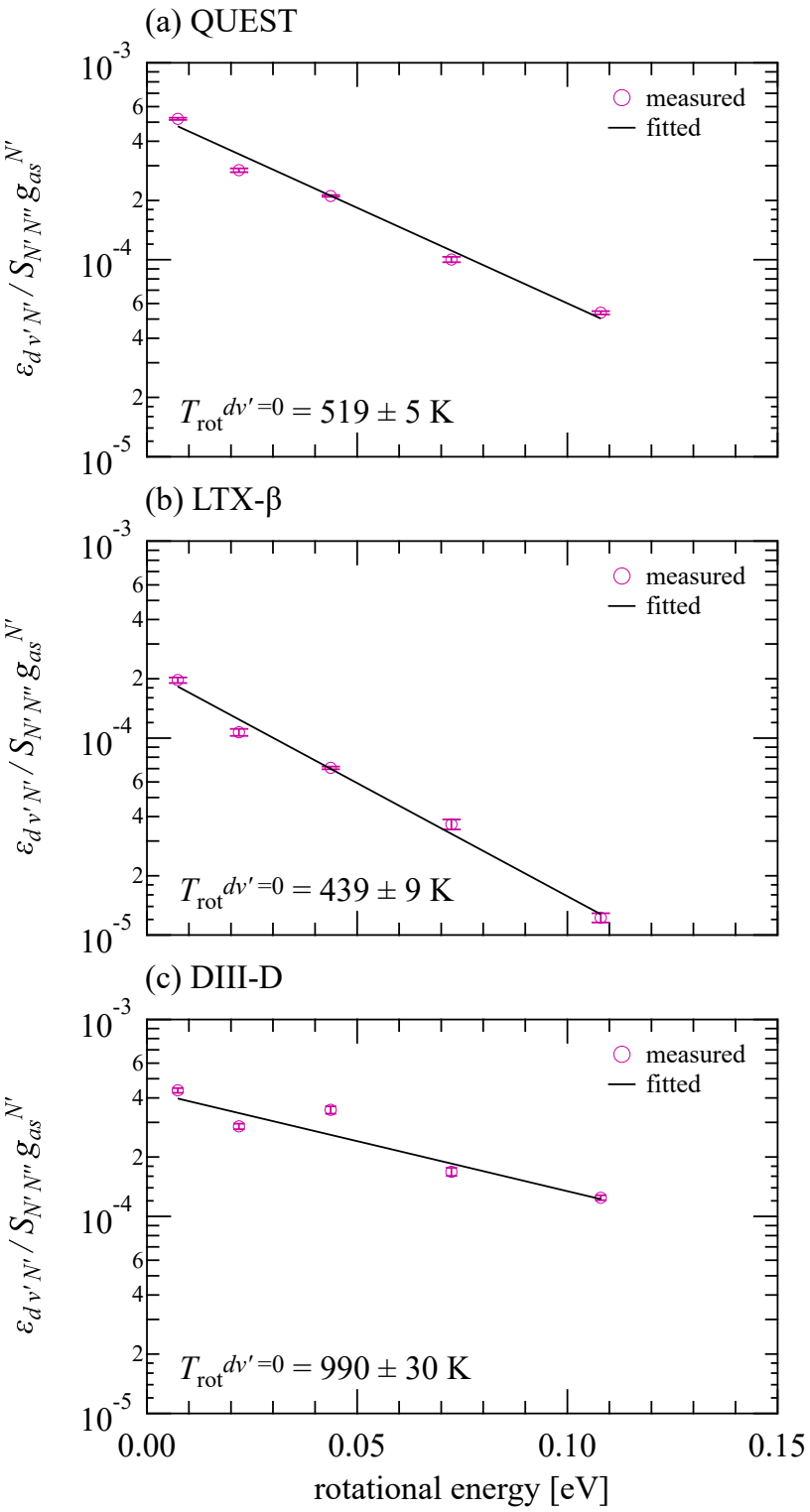

Fig. 4-12. Boltzmann plots for the measured emissivity in (a) LTX-β, (b) QUEST, and (c) DIII-D. The emissivity at $R = 0.9$ m was used for (a). For (b) and (c), the plots were derived from the spectra in Fig. 4-7.

4.2.3 Estimation of Plasma-Facing Surface Temperature

Surface effects and the effects of collisional-radiative processes in plasmas on $T_{\mathrm{rot}}^{Xv=0}$ were examined by measurements in the three tokamaks. The rotational temperature $T_{\mathrm{rot}}^{Xv=0}$ was measured near the plasma-facing walls whose surface temperatures are changeable: the hot walls (APS-W), the inboard side of the shells (lithium), and the outer divertor (ATJ graphite) for QUEST, LTX-β, and DIII-D, respectively.

In QUEST, the spatial profiles of $T_{\mathrm{rot}}^{Xv=0}$ were evaluated and compared with those calculated using the model described in Chapter 3. The evaluated radial profiles of $T_{\mathrm{rot}}^{Xv=0}$ are shown by solid lines in Fig. 4-13(c). The l-axis was defined as perpendicular to the hot wall as illustrated in Fig. 4-4(a), with l equal to the distance from the hot wall, *i.e.*, $l = 0$ on the surface. The evaluated radial profiles of $T_{\mathrm{rot}}^{Xv=0}$ in the range of $R = 0.7$–1.0 m were converted to l-directional profiles in the range of $l =$ 0.38–0.57 m. Monotonic increases in $T_{\mathrm{rot}}^{Xv=0}$ with l were observed for the two T_{wall} values and compared with those calculated using the model. Figs. 4-13(a) and (b) shows the l-directional profiles of n_{e} and T_{e} used for the calculation (lines), which were given on the basis of their radial profiles measured by Thomson scattering (markers) in the range of $R = 0.73$–1.09 m. The l-directional profile of n_{e} was approximated by a linear function of l, and that of T_{e} was approximated by a constant because of the small radial gradient of T_{e} and the small T_{e} dependence on the calculation results as shown in Subsection 3.4.4. The values for the other plasma parameters were determined from experimental results and are summarized in Table 4-1. The calculation was conducted at the same T_{wall} values as the measurement, and the initial values $T_{\mathrm{rot}}^{Xv=0}(l = 0)$ were set at T_{wall}. The calculation results are shown by dashed lines in darker colors in Fig. 4-13(c). Since the calculated $T_{\mathrm{rot}}^{Xv=0}$ are smaller than the measurements by approximately 450 K, $T_{\mathrm{rot}}^{Xv=0}$ was recalculated with the initial values $T_{\mathrm{rot}}^{Xv=0}(l = 0)$ increased by 454 K. The results are plotted with the dashed lines in lighter colors in Fig. 4-13(c). For both T_{wall} values, the calculated increases in $T_{\mathrm{rot}}^{Xv=0}$ with l have comparable magnitudes to the measured increases. An increase in $T_{\mathrm{rot}}^{Xv=0}$ with T_{wall} was also observed. The difference between the measured $T_{\mathrm{rot}}^{Xv=0}$ near the hot wall of $\approx$ 150 K is close

to that between the predetermined hot wall temperatures of 98 K. These results suggest that the increase in $T_{\mathrm{rot}}^{Xv=0}$ in the plasma is due to the collisional-radiative processes and that T_{wall} affects $T_{\mathrm{rot}}^{Xv=0}$ near the plasma-facing wall. The difference of 454 K between estimated $T_{\mathrm{rot}}^{Xv=0}(l=0)$ and T_{wall} may be attributable to the effect of the rovibrational excitation accompanying the surface recombination [36].

In LTX-β, $T_{\mathrm{rot}}^{Xv=0}$ was observed for different n_{e} and T_{wall} values. The l-axis was defined in the radial direction with the same height as chord 5, and its origin was on the surface of the shell (see Figs. 4-4(b) and 4-10(b)). The rotational temperature $T_{\mathrm{rot}}^{Xv=0}$ evaluated at $l = 0.03$ m is plotted by markers in Fig. 4-14(b) and is higher than T_{wall} for all conditions. They were compared to those calculated to estimate the increase with l. Two types of n_{e} profile were used for the calculation, as shown by magenta lines in Fig. 4-14(a), and they are given on the basis of n_{e} measured with the probe. A constant T_{e} was assumed since its variation was small. The values for the other plasma parameters were determined on the basis of measurements in QUEST because of the similar size of the device and similar values of n_{e} and T_{e} (see Table 4-1). The calculation was conducted at the same T_{wall} values as the measurement, and the initial values $T_{\mathrm{rot}}^{Xv=0}(l=0)$ were set at T_{wall}. The calculation results are shown by dashed lines in darker colors in Fig. 4-14(b), which are smaller than the measurement results by ≈ 450 K. Then, they are plotted versus n_{e} in Fig. 4-15. Increases in $T_{\mathrm{rot}}^{Xv=0}$ with n_{e} were observed for both the measurement and calculation results. The calculation results are smaller than the measurement results by 456 K, and the difference is comparable to that observed in QUEST. Therefore, $T_{\mathrm{rot}}^{Xv=0}$ were recalculated with the initial values $T_{\mathrm{rot}}^{Xv=0}(l=0)$ increased by 456 K, and the results are plotted by dashed lines in lighter colors in Figs. 4-14 (b) and 4-15. Assuming $T_{\mathrm{rot}}^{Xv=0}(l=0) \approx T_{\mathrm{wall}} + 450$ K, as observed in QUEST, the increase in $T_{\mathrm{rot}}^{Xv=0}$ with n_{e} is comparable to the increase due to collisional-radiative processes.

In DIII-D, $T_{\mathrm{rot}}^{Xv=0}$ was observed for different n_{e}, T_{e}, and T_{wall} values. The l-axis was defined as perpendicular to the divertor target as illustrated in Figs. 4-4(c) and 4-11(b), with l equal to the distance from the divertor target. The rotational temperature $T_{\mathrm{rot}}^{Xv=0}$ evaluated at $l = 0.01$ m is plotted by markers in Fig. 4-16 in colors corresponding to n_{e} measured with probes or by Thomson

scattering. The measured $T_{\mathrm{rot}}^{Xv=0}$ were higher than T_{wall} for all conditions, and the differences between the measured $T_{\mathrm{rot}}^{Xv=0}$ and T_{wall} are largest among the three tokamaks. The increase with l was estimated by comparing the measurement results to the calculation results. Constant n_{e} and T_{e} were assumed because small spatial variations were expected where $l \leq 0.01$ m, and their values were determined from those measured with the probes and by Thomson scattering. Note that the values of T_{e} and T_{p} were set at multiples of 5 eV because of the small dependence of the calculation results on them. The values of the other parameters were determined from simulations [57, 58] and are summarized in Table 4-1. The calculation was conducted at the same T_{wall} values as the measurement with $T_{\mathrm{rot}}^{Xv=0}(l = 0)$ set at T_{wall}. The calculation results are shown by dashed and chain lines in Fig. 4-16. The shading shows the uncertainty originating from that for n_{e}. Note that $T_{\mathrm{rot}}^{Xv=0}$ calculated with $n_{\mathrm{e}} \approx 10^{18}$ m^{-3} may be underestimated because the effects of atomic collisional processes ignored in this model are expected to be comparable to those of proton collisional processes. The calculated increase in $T_{\mathrm{rot}}^{Xv=0}$ due to the collisional-radiative processes is larger than those for the other two tokamaks owing to the larger n_{e}, which is consistent with the larger differences in the measured $T_{\mathrm{rot}}^{Xv=0}$ from T_{wall}. The calculated collisional increases match the measured increases within a factor of three. This difference between the calculation and measurement may become small by determining the location of emission more precisely and calculating the increase considering the spatial distribution of n_{e}. The increase in $T_{\mathrm{rot}}^{Xv=0}$ with T_{wall} was not observed.

The little dependence of $T_{\mathrm{rot}}^{Xv=0}$ on the surface material is implied from the results in QUEST and LTX-β. The plasma-facing walls of the three tokamaks are made of different materials as shown in Table 4-1. The increase due to the surface recombination is expected to be comparable (≈ 450 K) in QUEST and LTX-β. The increase in DIII-D can be evaluated by improving the estimation of the increase in $T_{\mathrm{rot}}^{Xv=0}$ due to the collisional-radiative processes, which will help to examine the dependence on the surface material.

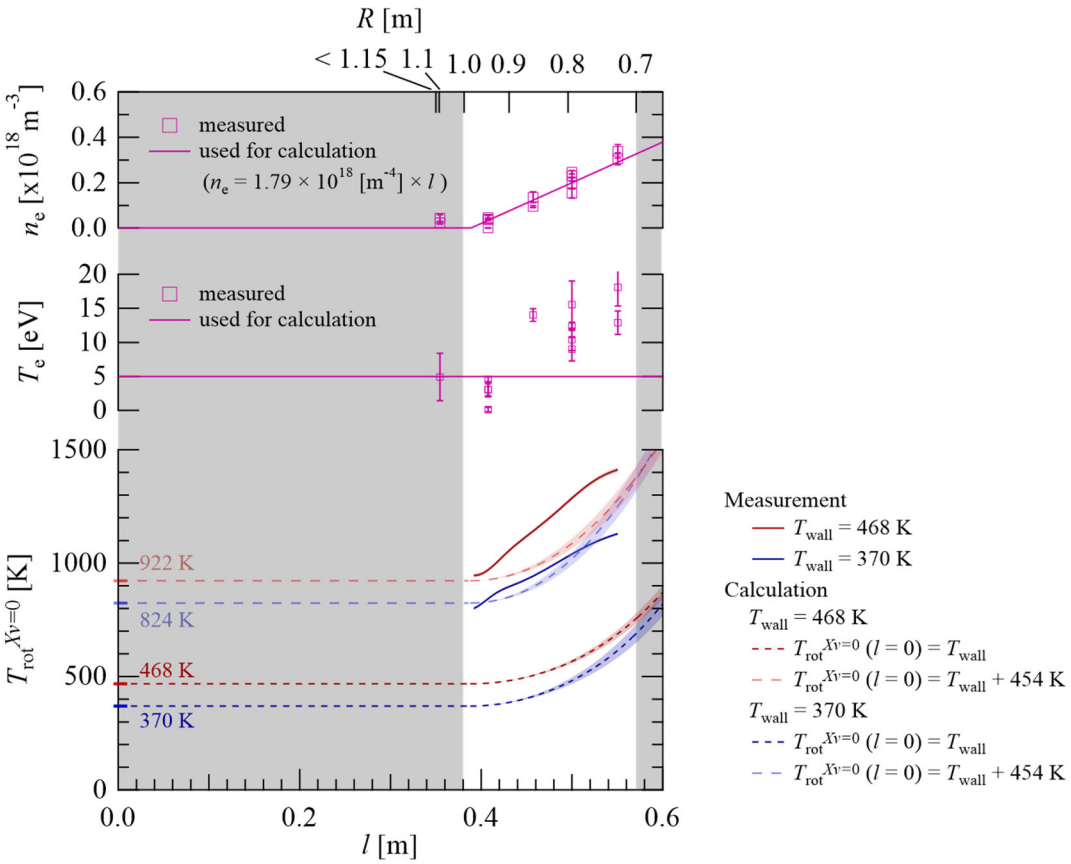

Fig. 4-13. Measurement and calculation results in QUEST. (a) n_e, (b) T_e, and (c) $T_{rot}^{Xv=0}$ plotted versus (top) R and (bottom) l. Markers in (a) and (b) show the values measured by Thomson scattering for both T_{wall} conditions. Lines show the profiles used for the calculation. (c) Comparison of measured and calculated $T_{rot}^{Xv=0}$ plotted versus l. Lines in red correspond to the calculation or measurement results for the higher T_{wall}, and those in blue correspond to the results for the lower T_{wall}. The solid and dashed lines respectively show the measured $T_{rot}^{Xv=0}$ and that calculated considering only the rotational excitation/deexcitation processes. The dashed lines shown in darker and lighter colors represent $T_{rot}^{Xv=0}$ calculated with $T_{rot}^{Xv=0}(l = 0) = T_{wall}$ and $T_{wall} + 454$ K, respectively.

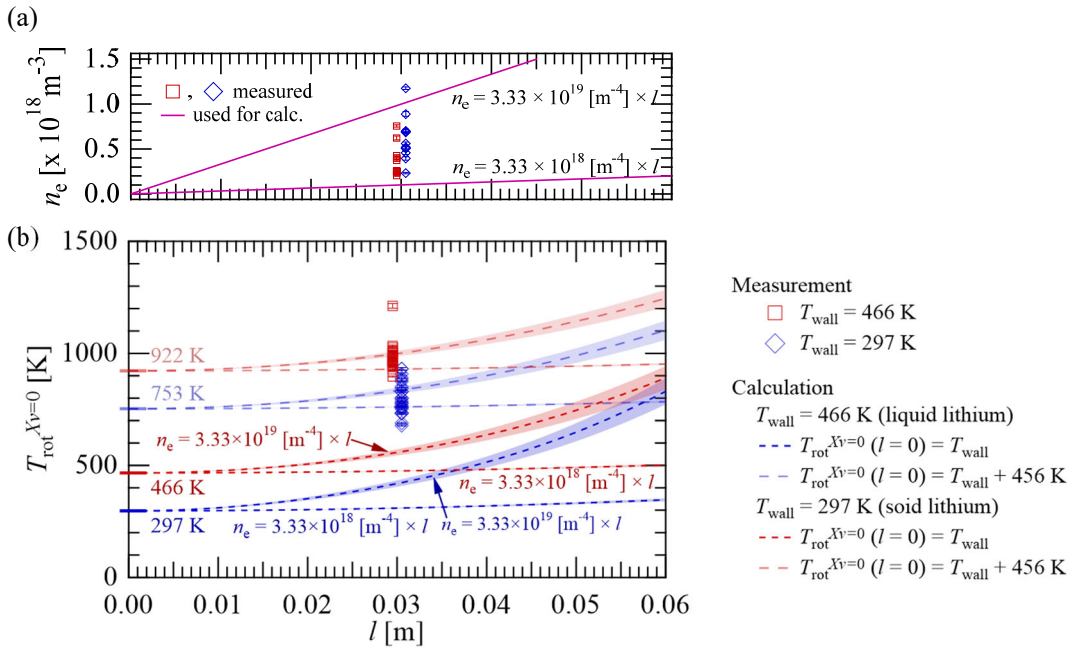

Fig. 4-14. Measurement and calculation results in LTX-β. (a) Measured and interpolated n_e versus l_{wall}. Markers show the n_e measured with the probe, and their colors indicate T_{wall} values. Lines show the profiles used for the calculation. (b) Comparison of measured and calculated $T_{rot}^{Xv=0}$ plotted versus l. Lines and markers in red correspond to the calculation or measurement for higher T_{wall}, and those in blue correspond to those for lower T_{wall}. The markers show the measured $T_{rot}^{Xv=0}$. The dashed lines show $T_{rot}^{Xv=0}$ calculated considering only the rotational excitation/deexcitation processes. Those in darker and lighter colors represent $T_{rot}^{Xv=0}$ calculated with $T_{rot}^{Xv=0}(l = 0) = T_{wall}$ and T_{wall} + 456 K, respectively.

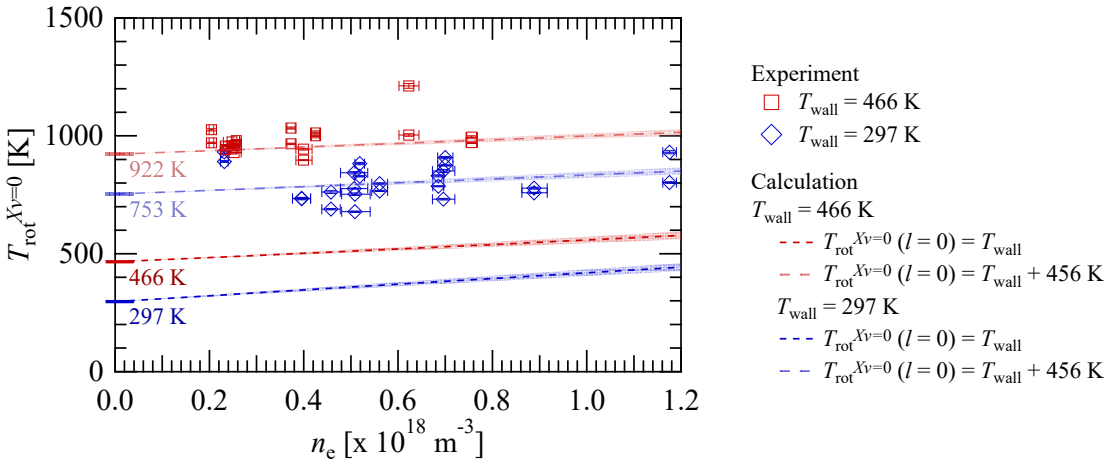

Fig. 4-15. Comparison of measured and calculated $T_{rot}^{Xv=0}$ at $l = 0.03$ m plotted versus n_e in LTX-β. Lines and markers in red correspond to the calculation or measurement results for higher T_{wall}, and those in blue correspond to the results for the lower T_{wall}. The measured $T_{rot}^{Xv=0}$ is represented by markers and plotted versus n_e measured with the Langmuir probe. The dashed lines show $T_{rot}^{Xv=0}$ calculated considering only the rotational excitation, and those in darker and lighter colors represent $T_{rot}^{Xv=0}$ calculated with $T_{rot}^{Xv=0}(l = 0) = T_{wall}$ and T_{wall} + 456 K, respectively.

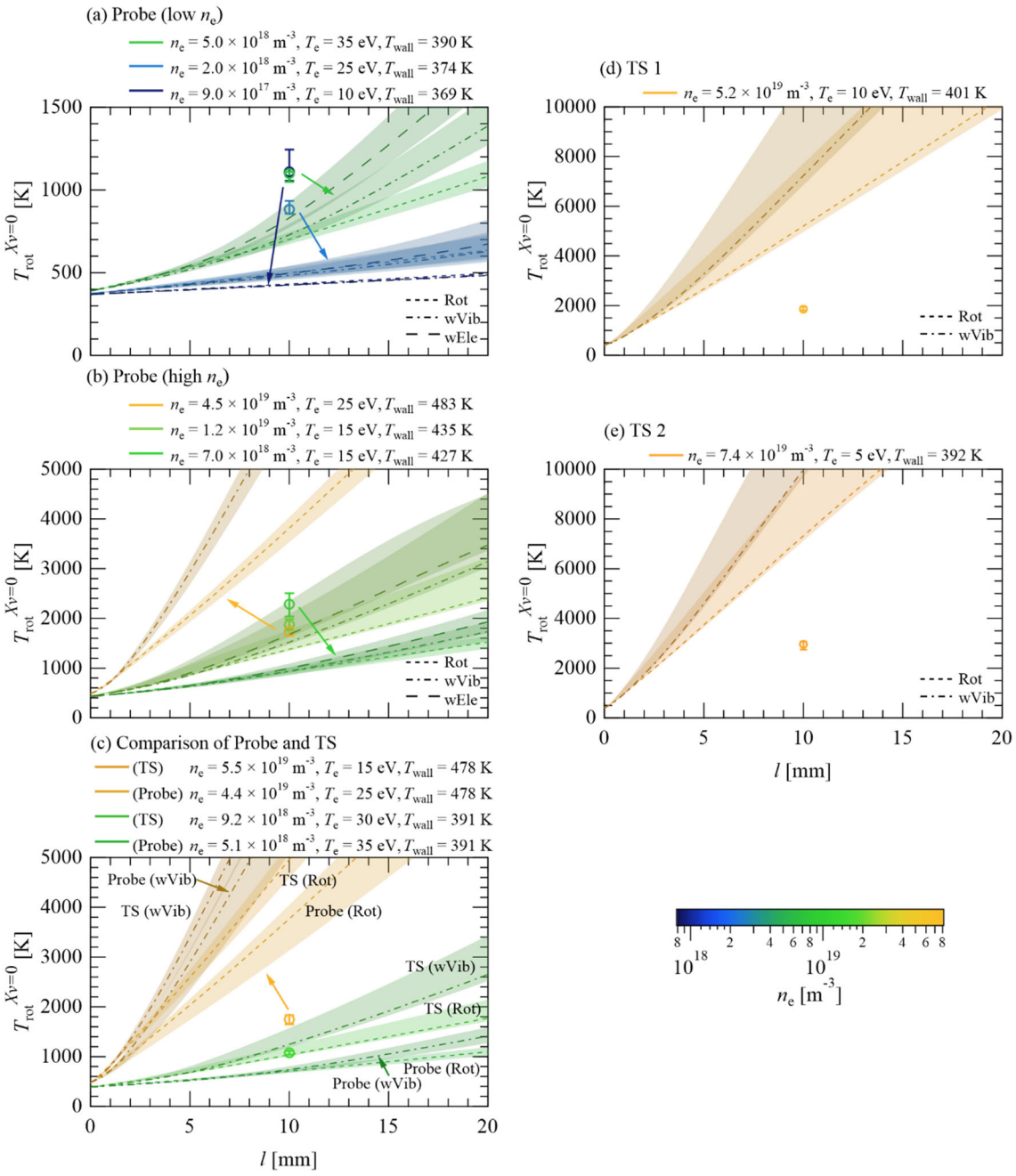

Fig. 4-16. Comparison of measured (markers) and calculated (lines) $T_{rot}^{Xv=0}$ plotted versus l in DIII-D. The short dashed, chain, and long dashed lines show the $T_{rot}^{Xv=0}$ calculated considering only the rotational excitation (Rot), rovibrational excitation (wVib), and electronic excitation (wEle), respectively. $T_{rot}^{Xv=0}$ was calculated using n_e and T_e measured with probes in the (a) low-n_e, and (b) high-n_e cases. (c) Comparison of $T_{rot}^{Xv=0}$ calculated using n_e and T_e measured with probes (Probe) and by Thomson scattering (TS). $T_{rot}^{Xv=0}$ was calculated using n_e and T_e measured by TS for (d) and (e).

4.3 Conclusion

For the development of surface thermometry, the effect occurring in the plasma on $T_{\mathrm{rot}}^{Xv=0}$ was separated from the measured $T_{\mathrm{rot}}^{Xv=0}$ by comparing it with $T_{\mathrm{rot}}^{Xv=0}$ calculated using the model described in Chapter 3. The Fulcher-α emission lines of hydrogen molecules (600–608 nm) were measured to estimate $T_{\mathrm{rot}}^{Xv=0}$ in three tokamaks with different plasma-facing materials: QUEST (atmospheric-plasma-sprayed tungsten), LTX-β (solid and liquid lithium), and DIII-D (ATJ graphite). The rotational temperature for the d state, $T_{\mathrm{rot}}^{dv'=0}$, was derived from the relative intensity of the measured spectra, and $T_{\mathrm{rot}}^{Xv=0}$ was estimated using the ratio of molecular constants ($B_{v'=0}(d)/B_{v=0}(X) \approx 0.5$) [62]. For the evaluation of their dependences on T_{wall}, n_{e}, and T_{e}, thermocouples or IR thermography was used to measure T_{wall}, and probes and/or Thomson scattering was used to measure n_{e} and T_{e}. In QUEST, increases in $T_{\mathrm{rot}}^{Xv=0}$ with l and T_{wall} were observed, and the measurement results agree well with the calculated profile when $T_{\mathrm{rot}}^{Xv=0}(l=0) = T_{\mathrm{wall}} + 454$ K. These results suggest that the collisional-radiative processes cause the increases in $T_{\mathrm{rot}}^{Xv=0}$ in the plasma and that $T_{\mathrm{rot}}^{Xv=0}$ near the plasma-facing wall depends on T_{wall}. In LTX-β, increases in $T_{\mathrm{rot}}^{Xv=0}$ with n_{e} and T_{wall} were observed. The results agree with the suggestion and imply the increase of ≈ 450 K on the surface. In DIII-D, $T_{\mathrm{rot}}^{Xv=0}$ was measured with various n_{e}, T_{e}, and T_{wall} values. The measured $T_{\mathrm{rot}}^{Xv=0}$ is consistent with the calculation results, which indicates the collisional increase in plasma. The effects of T_{wall} and the surface recombination on $T_{\mathrm{rot}}^{Xv=0}$ were unclear. The results in QUEST and LTX-β imply that the little dependence of $T_{\mathrm{rot}}^{Xv=0}$ on the surface material. These results show the increase in T_{wall} can be estimated from $T_{\mathrm{rot}}^{Xv=0}$, and the evaluation of the surface effect may enable to estimate the absolute value of T_{wall}.

5 Flow Measurement of Impurity Ions in Edge Plasmas using Emission Spectroscopy with Multiple Viewing Chords

5.1 Ion Flow in Edge Plasmas

Impurity ions play an important role in the radiation cooling of plasmas near the plasma-facing walls. However, the accumulation of impurity ions in the core plasma causes radiation loss and dilution of the fuel, and reduces the fusion reaction rate. The measurement of impurity ion flow velocities in the edge plasma is important in understanding the impurity ion circulation through the core and edge plasmas. As reported in this chapter, a method of deriving radial profiles of the impurity ion flow was developed and applied to the three types of edge plasma.

Impurity ions are generated in the divertor leg, enter in the core region, and are transported to the divertor as shown in Chapter 1. The structure of the edge plasma considered in this chapter can be approximately categorized into three regions: (i) SOL (scrape-off layer), (ii) X-point, and (iii) divertor leg. Fig. 5-1 shows the differences in the flow driving mechanisms in the three regions where the toroidal magnetic field and plasma current are directed in the counterclockwise and clockwise direction, respectively. The velocity of ions in the plasma can be expressed as the sum of the velocity components parallel and perpendicular to the magnetic field. The perpendicular flows are driven by the electric field and the gradient of the magnetic field, which are called $E \times B$ and $B \times \nabla B$ drifts, respectively. A pressure gradient along the magnetic field line is generated by these drifts and drives a return parallel flow called Pfirsch–Schlüter flow to balance these drifts. These flows are schematically illustrated in Fig. 5-1.

In the SOL (i), the $B \times \nabla B$ drift is directed upward and generates a pressure gradient directed upward along the magnetic field line. This pressure gradient drives the Pfirsch–Schlüter flow, and its toroidal component is parallel to the plasma current, *i.e.*, in the co-I_p direction. In the divertor leg (iii), the upward/downward $E \times B$ drift is driven by the electric field away from the separatrix. owing to the upward $E \times B$ drift, the Pfirsch–Schlüter flow in the co-I_p direction is driven by the

upward pressure gradient as shown in Fig. 5-1. In the region near the X-point (ii), the parallel flow is driven by both mechanisms; the Pfirsch–Schlüter flow is driven by $B \times \nabla B$ and $E \times B$ drifts except at the X-point.

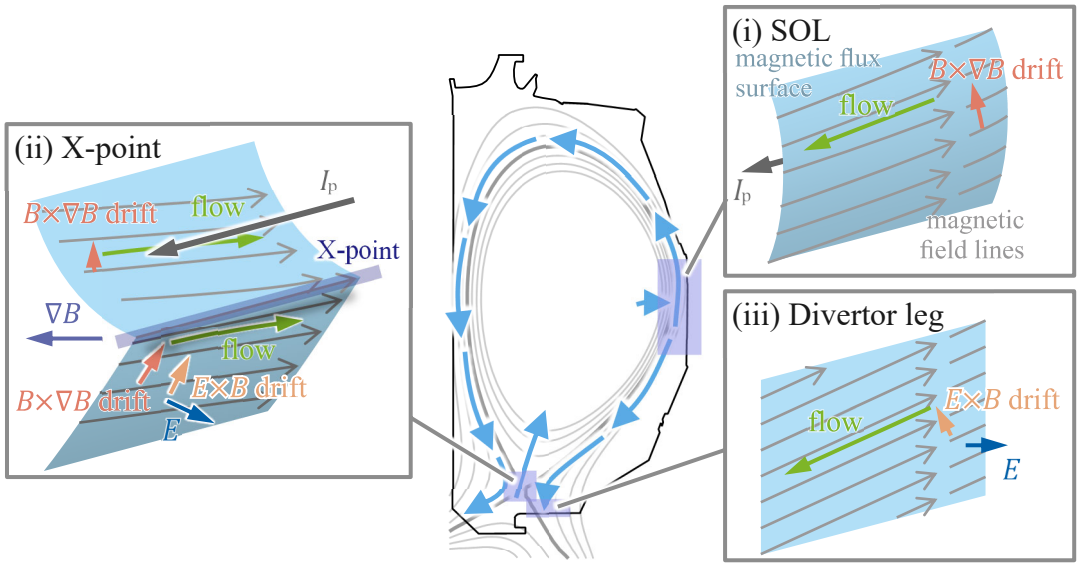

Fig. 5-1. Driving mechanisms of impurity ion flows (i) in SOL, (ii) near X-point, and (iii) near divertor. Gray, red, and green arrows respectively show the magnetic field lines, drift, and flow driven in the plasma.

5.2 Spectral Profiles of Emission Lines

The spectral profile of an emission line is characterized by the broadening and shift of the line. In the tokamak edge plasma, the broadening can be produced by three factors: natural, pressure, and Doppler broadenings. Natural broadening is caused by the time–energy uncertainty relation, and its FWHM is proportional to the Einstein A coefficient of the transition. For the CIII 2s3p (^{3}P)–2s3s (^{3}S) transition, the width is approximately 10^{-2} pm. Natural broadening is negligible since it is much smaller than the typical wavelength resolution of spectroscopic systems. Pressure broadening is caused by collisions between the emitting particles and the other particles and consists of collisional, resonance, and Stark broadenings. Collisional broadening is produced by collisions with neutral particles. Resonance broadening is produced by collisions with the particles of the same species as the emitting particles in the ground electronic state. Stark broadening is produced by collisions with charged particles. For the discharges in QUEST, contributions from the pressure broadening are estimated to be less than 10^{-2} pm [63, 64] and negligible. Doppler broadening reflects the velocity distribution of the emitting particles. When a particle moves with velocity v, the wavelength of the emission line, λ_0, is shifted by $\Delta\lambda = \lambda_0 \cdot v/c$, where c is the speed of light. When the velocity distribution of the particles follows a Maxwell distribution, the distribution function can be expressed as

$$f(v,T) = \sqrt{\frac{m}{2\pi k_\mathrm{B} T}} \exp\left(-\frac{mv^2}{2k_\mathrm{B}T}\right), \tag{5-1}$$

where T and m are the temperature and mass of the particle, respectively, and k_B is the Boltzmann constant. Since the velocity of the particle causes the wavelength shift of the emission line, the spectral profile becomes the Gaussian profile

$$\begin{aligned} g(\lambda,T) &= \frac{c}{\lambda_0}\sqrt{\frac{m}{2\pi k_\mathrm{B} T}} \exp\left[-\frac{mc^2}{2k_\mathrm{B}T}\left(\frac{\Delta\lambda}{\lambda_0}\right)^2\right] \\ &= \frac{1}{\sqrt{2\pi}w} \exp\left[-\frac{(\lambda-\lambda_0)^2}{2w^2}\right], \end{aligned} \tag{5-2}$$

where $w = \lambda_0\sqrt{k_\mathrm{B}T/mc^2}$.

The spectral shift of the emission line can be produced by Doppler, Stark, and Zeeman shifts. The Doppler shift is produced by the velocity of the emitting particle. For particles with a mean

velocity v_{m}, the velocity distribution can be expressed as the shifted Maxwell distribution

$$f_{\mathrm{m}}(v,T) = \sqrt{\frac{m}{2\pi k_{\mathrm{B}}T}} \exp\left[-\frac{m(v-v_{\mathrm{m}})^2}{2k_{\mathrm{B}}T}\right], \tag{5-3}$$

and the spectral profile can be expressed as

$$g_{\mathrm{m}}(\lambda,T) = \frac{1}{\sqrt{2\pi}w} \exp\left[-\frac{(\lambda-\lambda_0-\Delta\lambda_{\mathrm{m}})^2}{2w^2}\right], \tag{5-4}$$

where $\Delta\lambda_{\mathrm{m}} = \lambda_0 \cdot v_{\mathrm{m}}/c$ is the Doppler shift. The Stark shift is produced by the interaction of the external electric field and the dipole moment of the emitting particle. The Zeeman shift is produced by the external magnetic field and the magnetic dipole moment of the emitting particle. These interactions shift the energies of the degenerated magnetic sublevels and produce wavelength splitting of the transitions among the magnetic sublevels. For the discharges in QUEST, the Stark and Zeeman shifts are negligible.

5.3 Experimental Setup

5.3.1 Experimental Simulation of Edge Plasmas using Three Types of Magnetic Configuration

The impurity ion flow was measured by emission spectroscopy for three types of plasma simulating the three regions of the edge plasma. The three discharges were generated in QUEST at Research Institute for Applied Mechanics, Kyushu University (see Figs. 4-1(b) and 4-2(b)) by changing the magnetic configuration. Fig. 5-2 shows the magnetic flux surfaces of the three types of discharge plotted on the poloidal cross section of QUEST: (i) the inboard limiter configuration (IL), (ii) the inboard poloidal null configuration (IPN), and (iii) the open field configuration (toroidal electron cyclotron resonance (ECR)). Note that indices (i)–(iii) of the discharges correspond to those of the three regions in the edge plasmas shown in Fig. 5-1. The red and green lines show the last closed flux surfaces (LCFSs) and the resonance layer, respectively. The visible images of these discharges are shown in Fig. 5-3. Table 5-1 shows the parameters of the discharges. The toroidal velocities were measured during the flat-top phases. The LCFS for discharge (i) is limited onto the inboard limiter and that for discharge (ii) has an X-point at the inboard midplane. Discharge (iii) has no closed flux surfaces and has a vertically elongated cylindrical shape because of the heating at the resonance layer. The radial profiles of the electron density n_e and temperature T_e were measured at the midplane during the flat-top phase and are shown by markers in Fig. 5-4. For discharges (i) and (ii), they were measured by Thomson scattering. For discharge (iii), they were estimated from the measurement using probes on the upper and lower divertors.

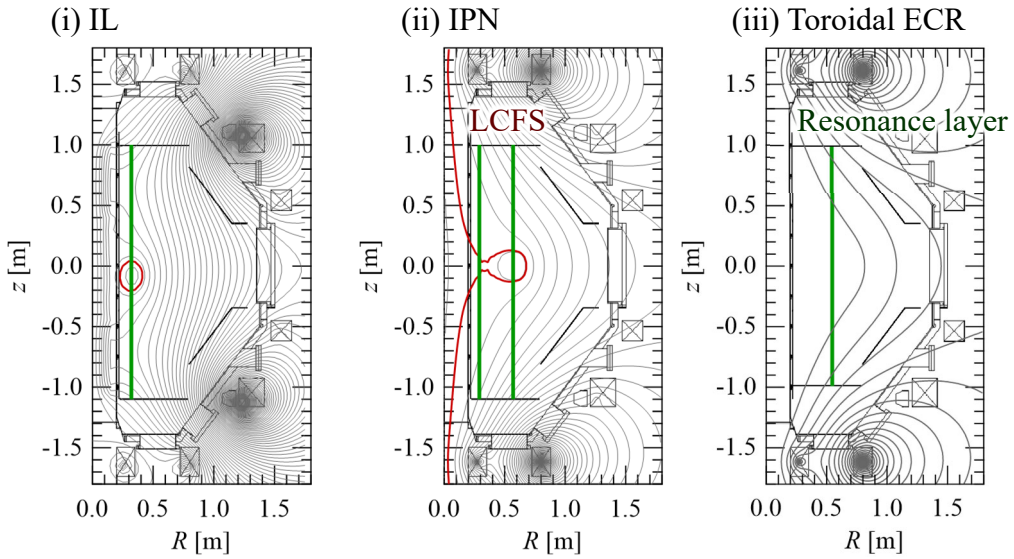

Fig. 5-2. Magnetic flux surfaces of (i) IL, (ii) IPN, and (iii) toroidal ECR. Red and green lines show the LCFSs and the resonance layer, respectively.

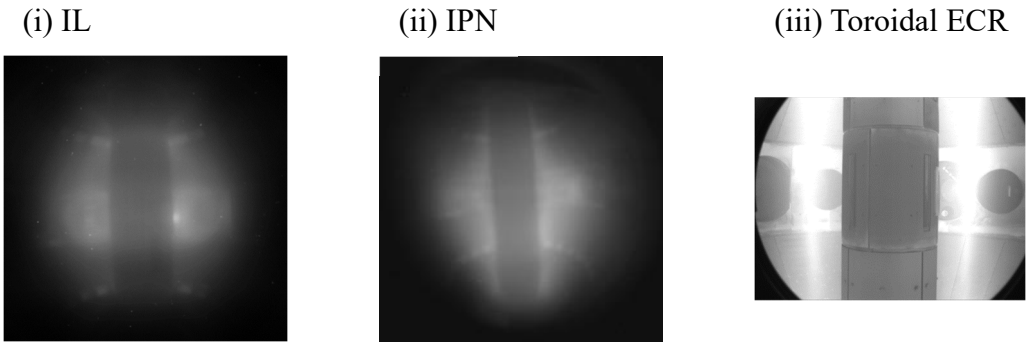

Fig. 5-3. Visible images of (i) IL, (ii) IPN, and (iii) toroidal ECR.

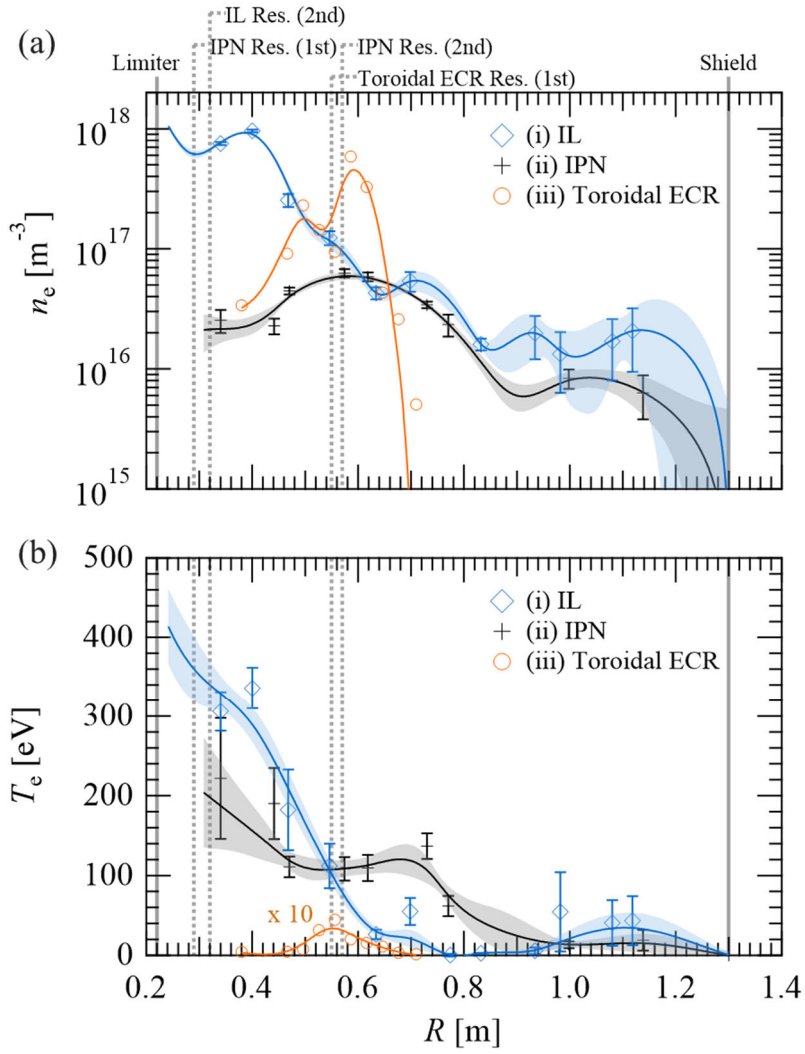

Fig. 5-4. Radial profiles of (a) electron density n_e and (b) electron temperature T_e measured in the three plasmas. Markers show the values measured by Thomson scattering for discharges (i) and (ii) and by those measured with probes for discharge (iii). Curves show the interpolation by a smoothing spline [65]. Long vertical lines show the positions of the inboard limiter and radiation shield. Dotted vertical lines show the position of the resonance layer for 28 GHz ECH in discharge (i) (IL Res. (2nd)), that for 8.2 GHz ECH in discharge (ii) (IPN Res. (1st) and (2nd)), and that for 8.2 GHz ECH in discharge (iii) (Toroidal ECR Res. (1st)).

Table 5-1. Parameters of (i) IL, (ii) IPN, and (iii) toroidal ECR discharges. t_{plasma} is the plasma duration, and the time of the flat-top phase is shown in parentheses. The following plasma parameters are for the flat-top phase. P_{ECH} is the ECH power, B_φ is the toroidal field strength at the magnetic axis, and I_p is the plasma current. R_{res}, R_{axis}, and R_{LCFS} are the radial positions of the resonance layer, magnetic axis, and LCFS, respectively. n_e and T_e are the electron density and temperature measured by Thomson scattering, respectively [56]. η is the tangency radius of each viewing chord, and its range is shown in each column. The number of viewing chords is also shown in parentheses. t_{exp} is the exposure time of the CCD.

	(i) IL	(ii) IPN	(iii) Toroidal ECR
Shot number	41176	37707	33681
t_{plasma} **[s]**	1.3 (0.2)	15 (15)	--- (3)
P_{ECH} **[kW]**	120	50	40
B_φ **@axis [T]**	0.5	0.1	0.3 (@R_{res})
I_p **[kA]**	25.4	7	1
R_{res} **[m]**	0.32 (2nd)	0.29 (1st), 0.57 (2nd)	0.55 (1st)
R_{axis} **[m]**	0.3	0.6	---
R_{LCFS} **[m]**	0.4	0.7	---
n_e **@axis [m^{-3}]**	1×10^{18}	5×10^{16}	4×10^{17} (@R_{res})
T_e **@axis [eV]**	300	100	4 (@R_{res})
η **[m]**	0.24–1.01 (24 chords)	0.31–0.95 (24 chords)	0.42–0.84 (14 chords)
t_{exp} **[s]**	0.13	1	1

5.3.2 Spectroscopic System with Multiple Viewing Chords

A schematic illustration of the spectroscopic system is shown in Fig. 5-5. The spectroscopic system consists of optical fiber bundles, a spectrometer, and a CCD camera. Multiple optical fiber bundles enable the system to simultaneously collect emission from plasma and from a lamp used as a wavelength reference. The emission from the plasma was collected onto the optical fiber bundle by means of an achromatic lens. The collected emission entered a Czerny–Turner spectrometer (Acton Research, AM-510; 1 m focal length, F/8.7, 1800 grooves/mm grating) through a slit of 50 μm width and an astigmatism compensation system, which consists of two concave mirrors (Tokyo Instruments; 0.3 m focal length). The dispersed spectra were recorded using a CCD camera (Andor Technology, DU440-BU2; 2048 × 512 pixels and 13.5 μm square pixels). The central wavelength of the spectrometer was set to 468 nm. The reciprocal linear dispersion was 6.4 pm/pixel, and the recorded wavelength range was 461.2–474.2 nm. The viewing chords were aligned at the midplane, and the tangency radius, *i.e.*, the distance from the center of the vessel to a viewing chord, is indicated as η. Fig. 5-5 shows the setup for the measurement taken in (ii) IPN discharge. Twenty-four viewing chords were aligned at the midplane using two optical fiber bundles with η ranging from 0.31 to 0.95 m.

The wavelengths of the observed spectra were absolutely calibrated using Th I and/or Ne I emission lines of known wavelengths [22] from a Th–Ne hollow cathode lamp (PerkinElmer Atomax) or a He–Ne discharge tube (NEC, GLG5000). Fig. 5-6 shows the spectra measured for the He–Ne discharge tube, where black arrows represent the identified Ne I emission lines. The Gaussian fitting to each emission line spectrum determined the central pixel. The central pixel was plotted versus the wavelength of each emission line and fitted to a quadratic function to derive the wavelength calibration curve, as shown in Fig. 5-6.

A change in room temperature can change the position of the recorded spectra on the CCD by up to 0.5 pixel. To evaluate the shift due to a change in room temperature, the emission lines from the reference lamp were measured immediately after each discharge and compared with those measured in advance using all optical fibers. A comparison of the wavelength corresponding to pixel 549 is shown in Fig. 5-7. For this discharge, the shift due to the change in room temperature was

evaluated as 1.5 pm, which corresponds to a toroidal velocity of 0.9 km/s.

The instrumental function was estimated from the profile of a Th I or Ne I emission line, assuming the negligible Doppler broadening. The profile was wider and more asymmetric in the upper part of the CCD, which corresponds to viewing chords at a smaller η, as shown in Fig. 5-8. To approximate the instrumental function, a double Gaussian function with the same width was used. The instrumental width was 20.2–43.9 pm in FWHM depending on the viewing chord.

The intensity was absolutely calibrated using the continuum spectrum from a standard tungsten-halogen lamp (Ushio Lighting, 212012) or a xenon lamp (Hamamatsu Photonics, L7810-02). Fig. 5-9 shows the setup for the calibration. A diffuse reflectance plate (Labsphere, SRT-99-050) was placed at a specified distance from the standard lamp since the spectral irradiance of the reflected light is known. Optical fibers were used to collect the reflected light through a UV sharp-cut filter.

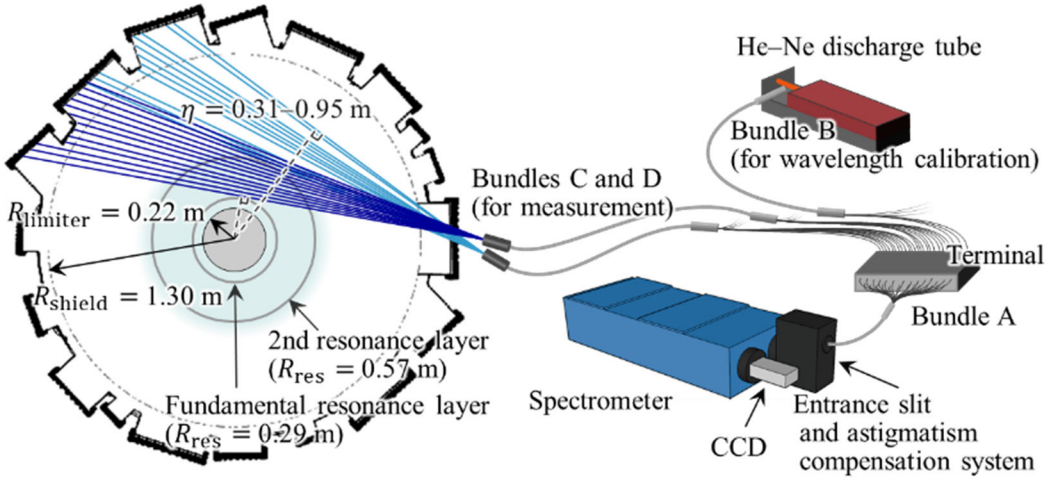

Fig. 5-5. Schematic illustration of the spectroscopic system. The viewing chords used for the measurements of (ii) IPN discharge are shown within the midplane of QUEST. The light blue and blue lines correspond to viewing chords of bundles C and D, respectively. η is the tangency radius of each viewing chord.

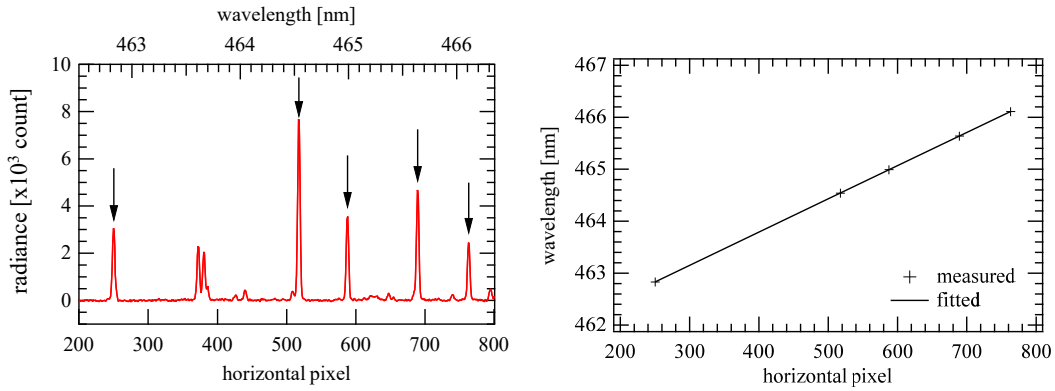

Fig. 5-6. (Left) Spectra of He-Ne discharge tube measured with chord 1. (Right) Relationship between wavelength and horizontal pixel (chord 1).

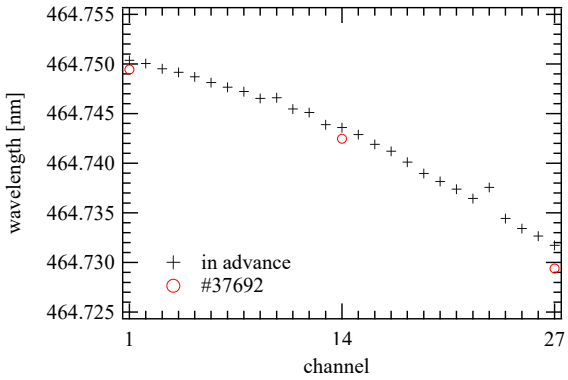

Fig. 5-7. Wavelength corresponding to pixel 549 of each channel of CCD.

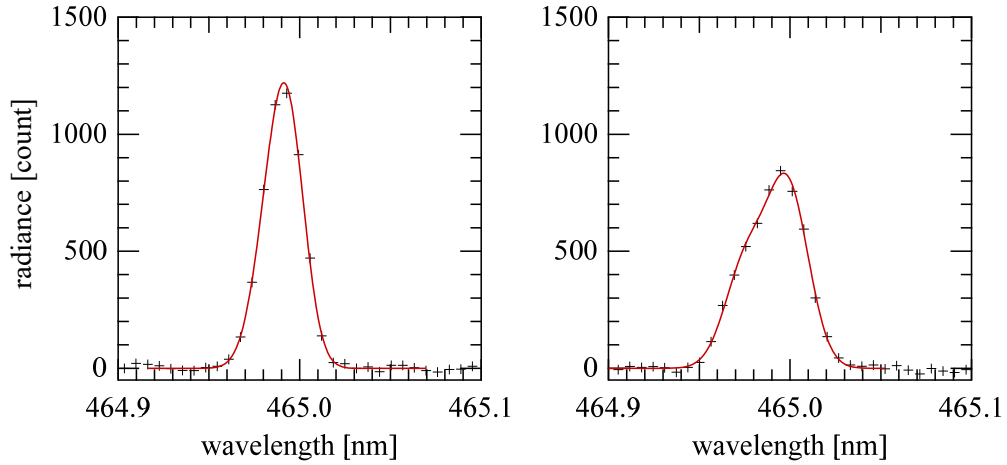

Fig. 5-8. Ne I emission line spectra measured with (left) chord 1 and (right) chord 24. Red curves show the double Gaussian fit used to determine the instrumental function.

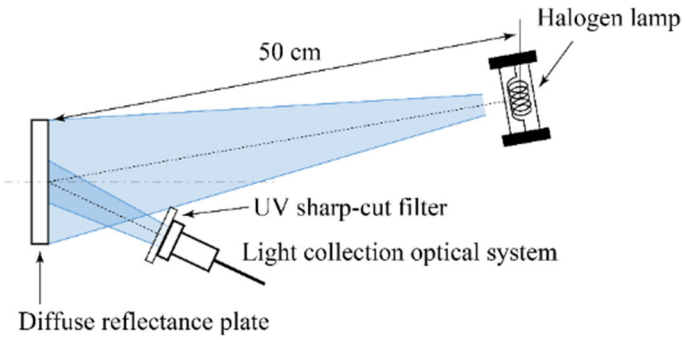

Fig. 5-9. Setup for sensitivity calibration using halogen lamp.

5.4 Inversion Method

Measured spectra for the three types of discharge are shown in Fig. 5-10. From the measured spectra, the following parameters were derived: chord-integrated radiance I_A, emissivity-weighted velocity V, emissivity ε, toroidal velocity V_φ, ion temperature T_i, and ion density n_i. Fig. 5-11 illustrates the process by which these parameters are derived. The chord-integrated radiance I_A and the emissivity-weighted velocity V were derived from the area and shift of the measured spectra, respectively. Since the measured spectra are the integrals of the emission spectra along the viewing chords, inversion methods were applied to derive radial profiles of ε, V_φ, T_i, and n_i under the assumption of axisymmetry. First, Abel inversion was applied to derive ε from I_A. Radial profiles of V_φ and T_i were derived from the ε profile and the measured spectra using the "shell model". The radial n_i profile was derived from ε using a coronal model.

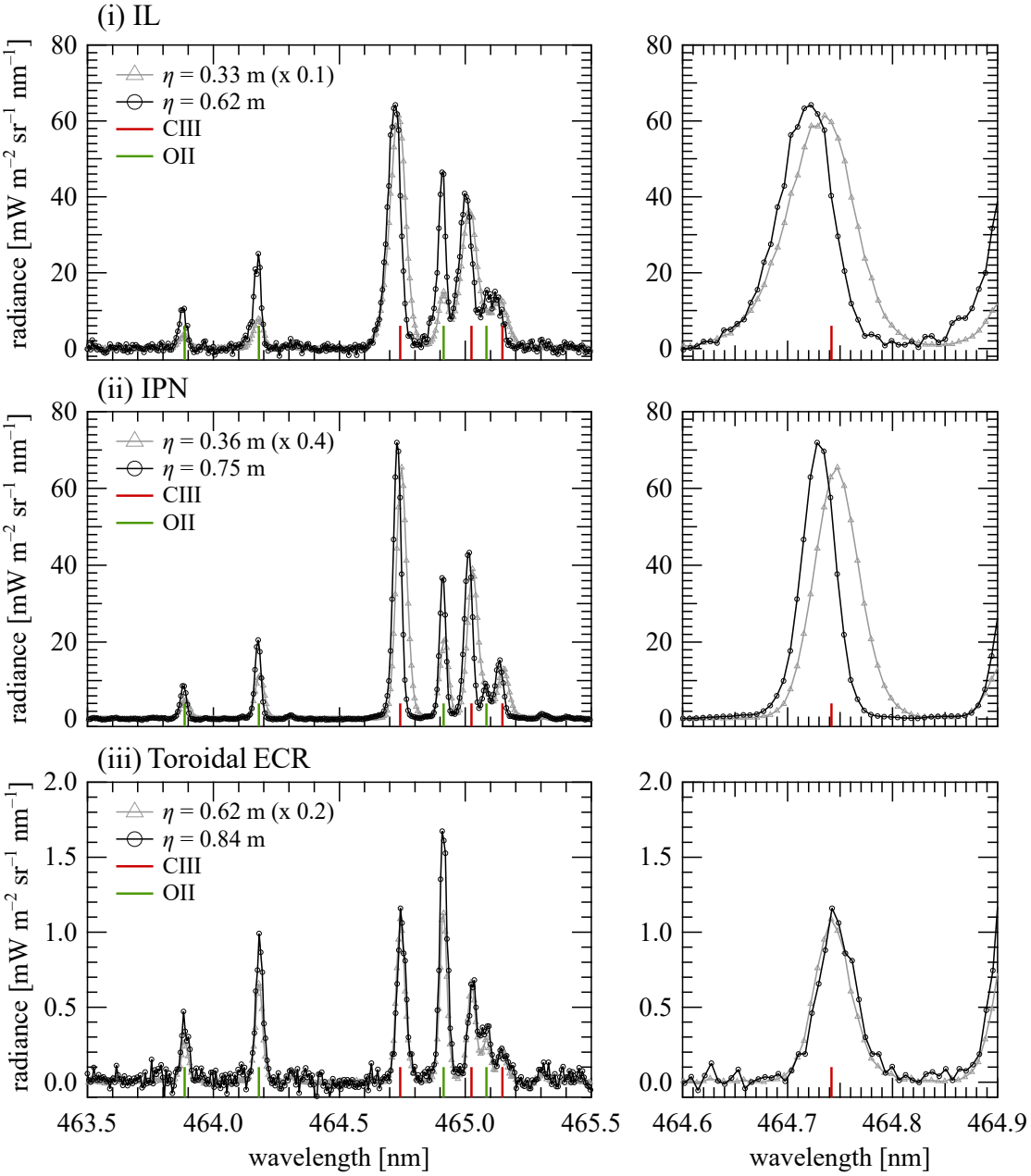

Fig. 5-10. Measured spectra for (i) IL, (ii) IPN, (iii) and toroidal ECR discharges. Gray and black markers show the spectra measured on different viewing chords. Red and green lines indicate the central wavelength of CIII and OII emission lines, respectively. The figures in the right column are enlarged views of the spectra on the left.

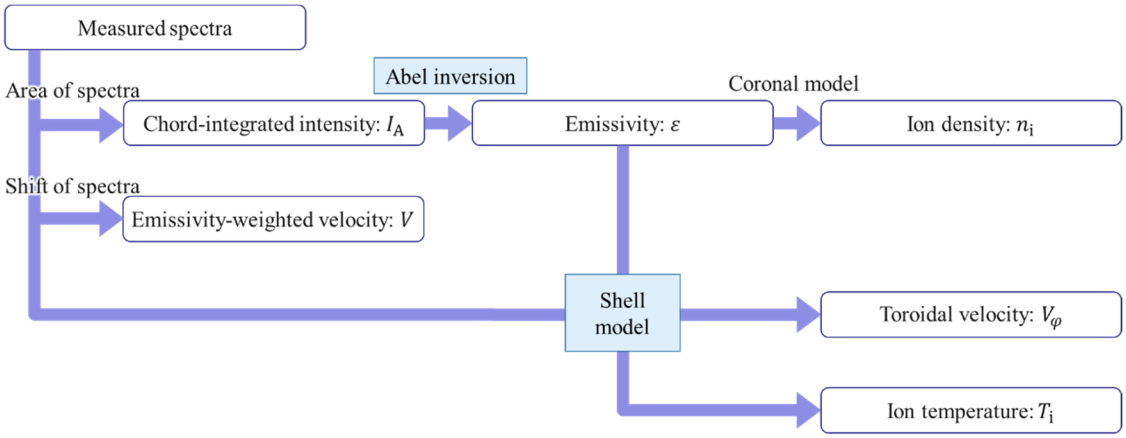

Fig. 5-11. Flowchart of analysis. First, chord-integrated radiance I_A and emissivity-weighted velocity V were derived from the measured spectra. Emissivity ε was estimated from I_A using Abel inversion. Ion density n_i was derived from ε using a coronal model. Toroidal velocity V_φ and temperature of the ion T_i were estimated from ε and the measured spectra using a shell model.

5.4.1 Chord Integral of Spectra

An axis along the viewing chord, the s-axis, was introduced as shown in Fig. 5-12. The line spectrum for the emission at position s can be expressed as

$$e(\lambda, s) = \frac{\varepsilon(s)}{\sqrt{2\pi}w(s)} \exp\left\{-\frac{\left[\lambda - \lambda_0 - \left(\vec{s}\cdot\overrightarrow{V_\varphi}(s)\right)\frac{\lambda_0}{c}\right]^2}{2w(s)^2}\right\}. \tag{5-5}$$

where $\vec{s}$ is the unit vector along the viewing chord and $\overrightarrow{V_\varphi}(s)$ is the toroidal velocity vector at s. The inner product of $\vec{s}$ and $\overrightarrow{V_\varphi}(s)$ represents the velocity along the viewing chord. The chord-integrated spectrum $I(\lambda)$ is expressed as the integral of $e(\lambda, s)$,

$$\begin{aligned} I(\lambda) &= \int_{s_{\min}}^{s_{\max}} e(\lambda, s)ds \\ &= 2\int_0^{s_{\max}} e(\lambda, s)ds \\ &= 2\int_0^{s_{\max}} \frac{\varepsilon(s)}{\sqrt{2\pi}w(s)} \exp\left\{-\frac{\left[\lambda - \lambda_0 - \left(\vec{s}\cdot\overrightarrow{V_\varphi}(s)\right)\frac{\lambda_0}{c}\right]^2}{2w(s)^2}\right\} ds, \end{aligned} \tag{5-6}$$

where $s_{\min}$ and $s_{\max}$ are the intersection points of the viewing chord and the outer boundary of

emitting region, and $s_{\max} = -s_{\min}$.

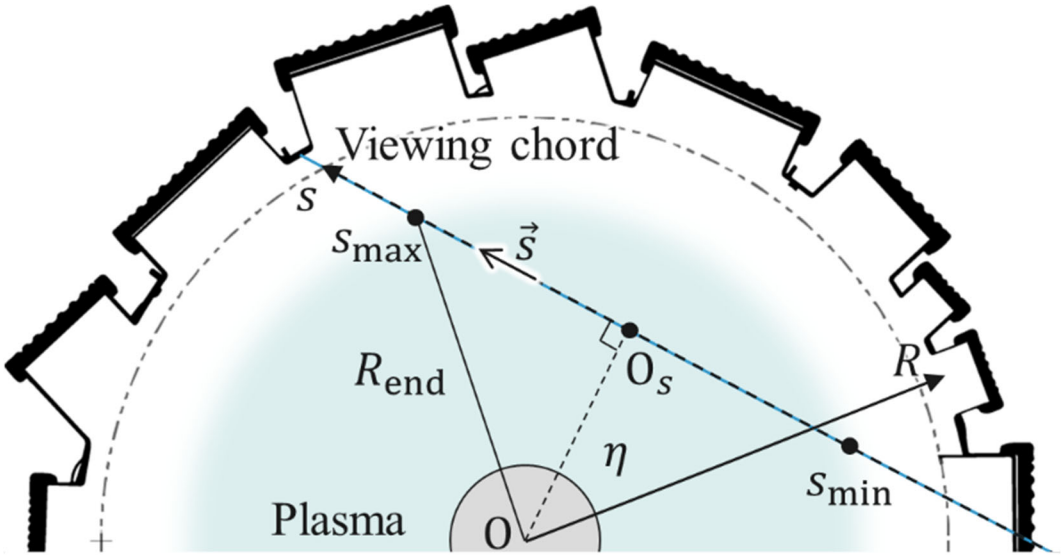

Fig. 5-12. Axis along the viewing chord, s-axis, used for chord integral of spectra. O_s is the origin of the s-axis.

5.4.2 Abel Inversion

Abel inversion is an inversion method used to derive the radial profile from chord-integrated values under the assumption of axisymmetry. The chord-integrated radiance I_{A} was derived from the area of the measured emission line spectrum. The radial profile of the emissivity $\varepsilon(R)$ was derived from I_{A} using Abel inversion:

$$\varepsilon(R) = -\frac{1}{\pi}\int_{R}^{R_{\mathrm{end}}} \frac{1}{\sqrt{\eta^2 - R^2}} \frac{dI_{\mathrm{A}}(\eta)}{d\eta} d\eta, \qquad (4\text{-}3)$$

where R_{end} is the outer boundary of the emission. Since Eq. (4-3) requires a continuous distribution of $I_{\mathrm{A}}(\eta)$, the measured I_{A} was interpolated and extrapolated with a single or double sigmoid function, as shown in Fig. 5-15 with solid lines. The outer boundary of the emission R_{end} was determined as the position where the extrapolated I_A is zero.

The error of ε was estimated by the following six steps: (I) calculate the 68.3% confidence interval when I_{A} is interpolated, (II) estimate the standard deviation of I_{A} considering the

confidence interval as the standard deviation, (III) generate 500 datasets by adding Gaussian noise with the estimated standard deviation to the measured I_{A}, (IV) interpolate the datasets, (V) apply Abel inversion to the dataset, and (VI) calculate the mean and standard deviation of the derived ε for each radial position (R). The mean and standard deviation were respectively plotted as the value and standard deviation of ε.

5.4.3 Shell Model

For the estimation of the V_φ and T_{i} profiles, concentric regions ("shells") are introduced as shown in Fig. 5-13. The radial profiles of V_φ and T_{i} were derived assuming that these parameters are constant in each concentric region.

The viewing chords and shells are denoted as chords 1, 2, 3, … and shells 1, 2, 3, …, respectively, from the outboard side (see Fig. 5-13). The radii of shell boundaries were determined as the average of η for the two adjacent viewing chords. The radius of the outermost shell boundary was set to R_{end}. Since chord k intersects with shells 1, 2, …, and k, the spectrum integrated along chord k ($I_k(\lambda)$) is expressed by the sum of the spectra from the intersecting shells as

$$I_k(\lambda) = \sum_{j=1}^{k} I_{kj}(\lambda), \tag{5-7}$$

where $I_{kj}(\lambda)$ is the emission line spectrum from shell j integrated along chord k. The chord-integrated spectrum $I_{kj}(\lambda)$ is expressed as

$$I_{kj}(\lambda) = 2\gamma_k \int_{s_{k(j+1)}}^{s_{kj}} \frac{\varepsilon(s_k)}{\sqrt{2\pi} w_j} \exp\left\{ -\frac{\left[\lambda - \lambda_0 - \left(\overrightarrow{s_k} \cdot \overrightarrow{V_{\varphi,j}}\right)\frac{\lambda_0}{c}\right]^2}{2w_j^2} \right\} ds_k \tag{5-8}$$

by analogy with Eq. (5-6), where subscript j designates the parameters for shell j, s_k is the axis along chord k, and s_{kj} is the intersection between chord k and the outer boundary of shell j. Note that $s_{k(k+1)} = 0$. Since the measured I_{A} was different from the chord integral of the emissivity profile derived by Abel inversion $\varepsilon(R)$, a compensation factor γ_k was introduced to satisfy

$$I_{\mathrm{A}}(\eta_k) = 2\gamma_k \int_0^{s_{k1}} \varepsilon(s)ds, \tag{5-9}$$

where η_k is the tangency radius of chord k. The spectrum measured on chord k, $M_k(\lambda)$, is expressed as the convolution of $I_k(\lambda)$ and the instrumental function for chord k, $F_k(\lambda)$.

The radial profiles of V_φ and T_i were determined by fitting the spectra measured for chords from the outboard side. By fitting $M_1(\lambda)$ to the measured spectrum on chord 1, T_i and $\overrightarrow{V_\varphi}$ in shell 1, *i.e.*, $T_{\mathrm{i},1}$ and $\overrightarrow{V_{\varphi,1}}$, respectively, were determined. Then, $T_{\mathrm{i},1}$ and $\overrightarrow{V_{\varphi,1}}$ were used for the fitting of $M_2(\lambda)$ to the spectrum measured on chord 2 to determine $T_{\mathrm{i},2}$ and $\overrightarrow{V_{\varphi,2}}$, the parameters for shell 2. The parameters for the inner shells were determined by similar procedures. The uncertainties in the obtained parameters were estimated from the standard deviations of the weighted fitting. Random and systematic errors were considered as the weight. Random errors mainly originate from the plasma, detector, and shot noise and were estimated from the standard deviations of signals without any emission lines. Systematic errors include errors that originate from wavelength calibration and approximations of the instrumental function, the radial profile of ε, and the parameters in the outer shells except for shell 1.

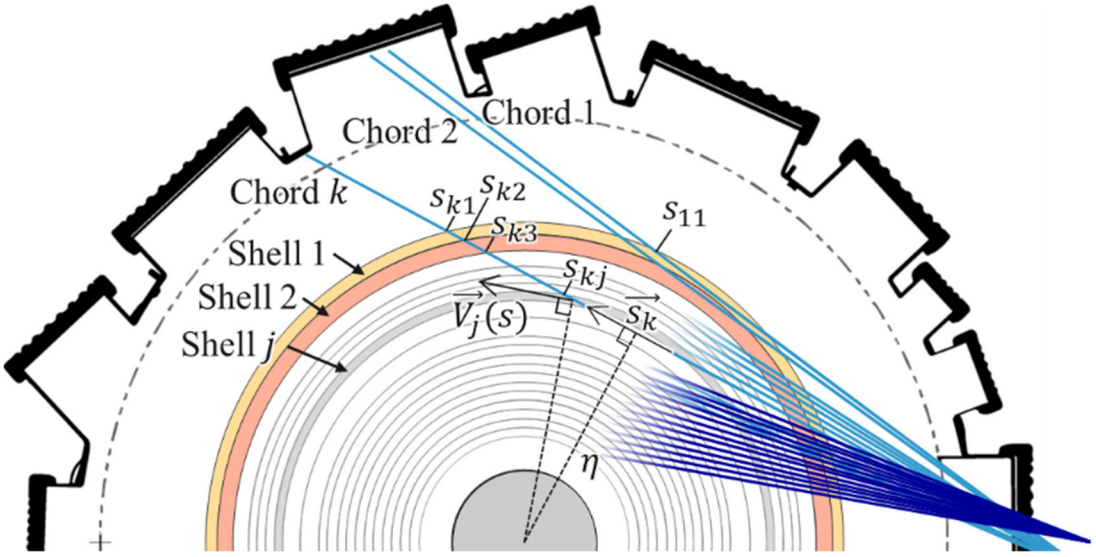

Fig. 5-13. Schematic illustration of regions in the midplane used for shell model. The light blue and blue lines show the viewing chords used for the measurement of (ii) IPN discharge. Gray concentric circles show the boundaries of shells, and shells 1, 2, and j are colored yellow, orange, and gray, respectively.

5.4.4 Verification of the Inversion Methods using Model Data

The errors due to the inversion methods were verified using model data. Three types of model data were produced with radial profiles similar to those measured in discharges (i)–(iii). The generated profiles of ε, V_φ, and T_i are shown by dashed lines in Figs. 5-14(c)–(e), respectively. Chord-integrated spectra were calculated for each viewing chord. The widths of the viewing chords were ignored in the calculation. Gaussian noise was added with standard deviation of comparable magnitude to the one in the experiments.

The inversion methods were applied to the synthesized spectra. The derived profiles are shown by markers in Figs. 5-14(a), (b), (d), and (e), and by solid lines in Fig. 5-14(c). The solid and dotted curves in Fig. 5-14(a) describe the curve calculated from the model profile and the interpolated curve used for Abel inversion, respectively. The short vertical dotted lines in Figs. 5-14(d) and (e) indicate the boundaries of shells used for the shell model for each set of data. The differences between the assumed model data and the inversion results for ε, V_φ, and T_i are less than 3.8 pW m^{-2} sr^{-1} nm^{-1}, 1.4 km/s, and 5.6 eV for model (i), 0.58 pW m^{-2} sr^{-1} nm^{-1}, 5.0 km/s, and 10.0 eV for model (ii), and 25 pW m^{-2} sr^{-1} nm^{-1}, 8.1 km/s, and 15 eV for model (iii), respectively. A large difference in V_φ was observed on the inboard side of models (ii) and (iii), where the emissivity is small. The difference in V_φ was also large on the outboard side of model (ii) owing to the overestimation of R_end. Except for these regions, the differences in V_φ were found to be less than 4 km/s. The results also indicate that the effect of the chord integral on V_φ is large for model (ii) but small for models (i) and (iii).

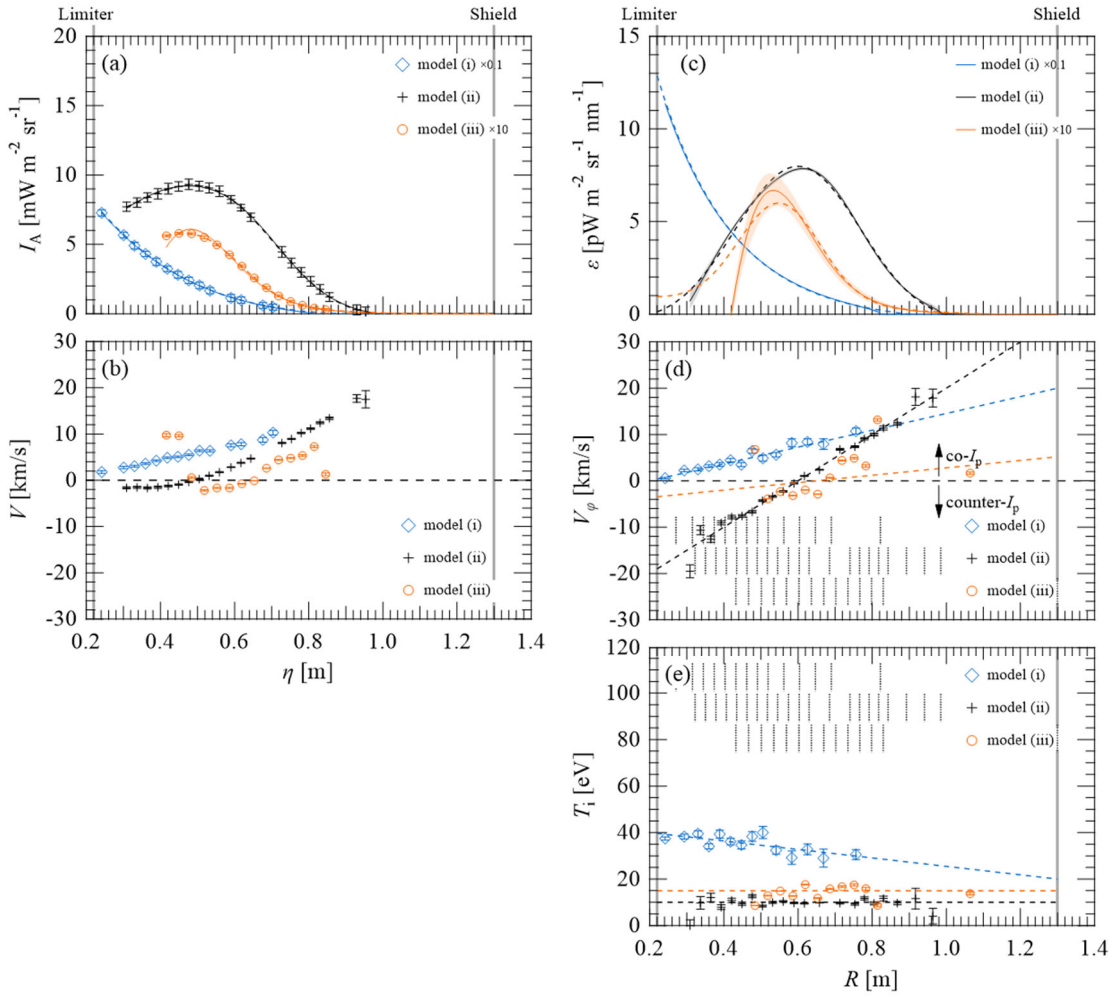

Fig. 5-14. Verification of the inversion method. Dashed lines in (c)–(e) show the values of models used for the verification. Dashed lines in (a) are calculated from the model profile of ε shown in (c). Markers and solid lines in (a) are the chord-integrated radiance I_A calculated from the area of the synthesized spectra and the interpolated curve of I_A, respectively. Markers in (b), (d), and (e), and solid lines in (c) are values reconstructed by the inversion method.

5.5 Results

The η-direction profiles of I_A and V, and the radial profiles of ε, V_φ, and T_i were derived for the three types of discharge: (i) the inboard limiter configuration (IL), (ii) the inboard poloidal null configuration (IPN), (iii) the open field configuration (toroidal ECR). The derived profiles are shown in Figs. 5-15(a)–(e), respectively. The results obtained by fitting the measured spectra to $M_k(\lambda)$ are shown in Fig. 5-16. For discharge (i), the spectra measured on ten viewing chords were removed because of the low S/N ratio or the superposition of the signal originating from X-rays. Three pairs of spectra measured for adjacent viewing chords were averaged for discharge (ii) before applying the inversion methods, because the differences in η of the viewing chords were smaller than the widths of the chords (~30 mm). The number of spatial points in Figs. 5-15(d) and (e) is smaller than that in Figs. 5-15(a) and (b), since the measured spectra could not be expressed as $M_k(\lambda)$ (see Fig. 5-16).

A co-I_p toroidal velocity V_φ was observed in the outer SOLs of discharges (i) ($R > 0.4$ m) and (ii) ($R > 0.7$ m), and on the outboard side of the resonance layer of discharge (iii) ($R > 0.55$ m), as expected from the Pfirsch–Schlüter flow. The toroidal velocity V_φ in the counter-I_p direction was measured on the inboard side of the X-point of discharge (ii) ($R < 0.55$ m). The Pfirsch–Schlüter flow driven by $B \times \nabla B$ drift is in the co-I_p direction on both the inboard and outboard sides of the X-point. The reversal of the direction of V_φ shows that the flow for $R < 0.55$ m is driven by the electric field antiparallel to R. In discharge (iii), the direction of V_φ also reversed at the resonance layer, $R = 0.55$ m. This is because the electric fields in discharge (iii) are in the direction away from the resonance layer, which drives the co- and counter-I_p flows on the outboard and inboard sides of the resonance layer, respectively.

The emissivity ε had a peak near the peak position of n_e for all the discharges. T_i was largest in discharge (i) owing to the largest T_e and the shortest ion temperature relaxation time with electrons, which is caused by the largest n_e.

The radial profile of C^{2+} ion density n_i was estimated from that of ε using the coronal model. The estimated profiles are shown in Fig. 5-17. The measured radial profiles of n_e and T_e

were interpolated by a smoothing spline [65], and the derived continuous profiles were used for the estimation of n_{i}. For discharge (iii), the data of $C_{\mathrm{e}}(1,q)$ at T_{e} = 5 eV was used, which is the data available for the smallest T_{e} [66]. The n_{i} profiles for discharges (ii) and (iii) increased sharply on the outboard side because of the small $C(1,q)$ originating from the small T_{e}. The estimated n_{i} sometimes became larger than n_{e}, this is physically impossible and probably due to the inappropriate assumption of the coronal model. The obtained n_{i} had a peak on the inboard side for all the discharges, suggesting that the source of carbon was the inboard limiter.

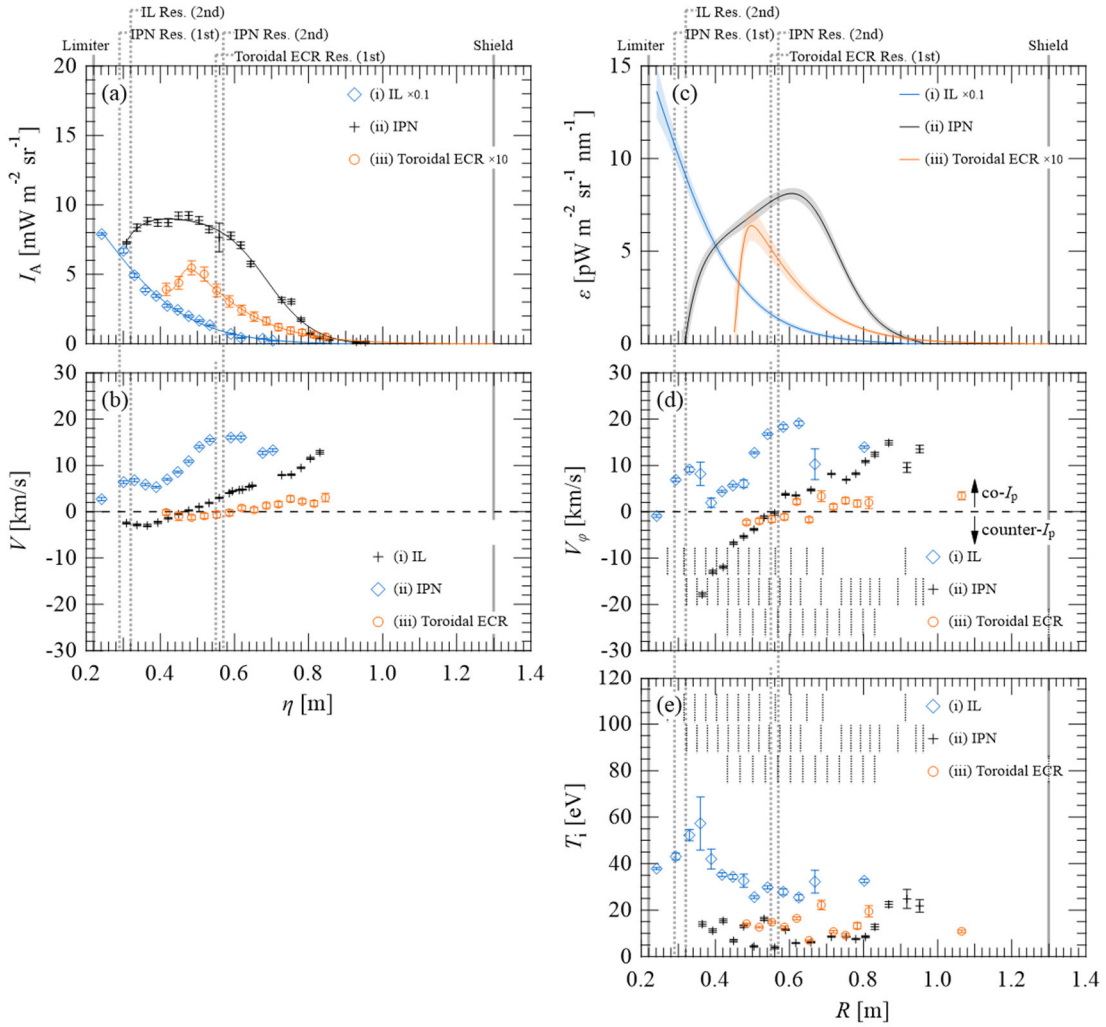

Fig. 5-15. η-direction profiles of (a) chord-integrated radiance I_A and (b) emissivity-weighted velocity V, and radial profiles of (c) emissivity ε, (d) toroidal velocity V_φ, and (e) ion temperature T_i. Solid lines in (a) are interpolated curves of I_A. Long solid vertical lines show the positions of the inboard limiter and radiation shield. Dotted vertical lines show the position of the resonance layer for 28 GHz ECH in discharge (i) (IL Res. (2nd)), that for 8.2 GHz ECH in discharge (ii) (IPN Res. (1st) and (2nd)), and that for 8.2 GHz ECH in discharge (iii) (Toroidal ECR Res. (1st)). Short vertical dotted lines in (d) and (e) indicate the boundaries of the shells used for the inversion method, which are different for different types of discharge.

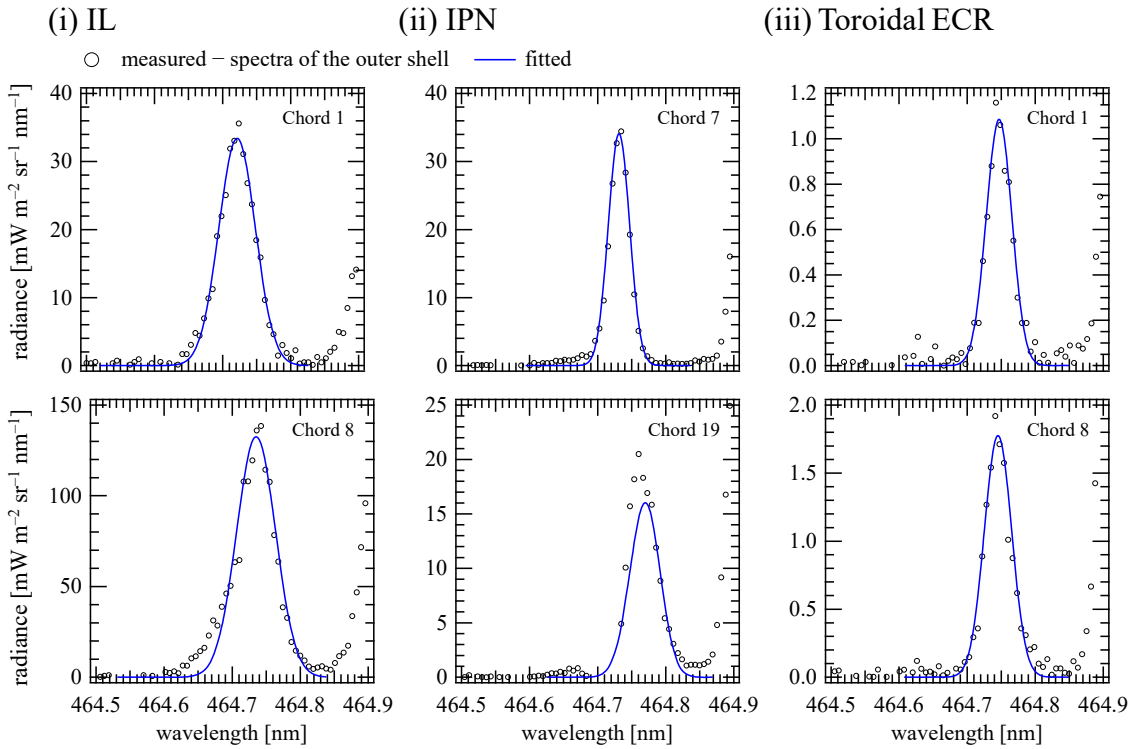

Fig. 5-16. Measured and fitted spectra for (i) IL, (ii) IPN, and (iii) toroidal ECR plasmas. Black markers show the subtraction of the spectra of the outer shell from the measured spectra, and blue lines show the fitted lines.

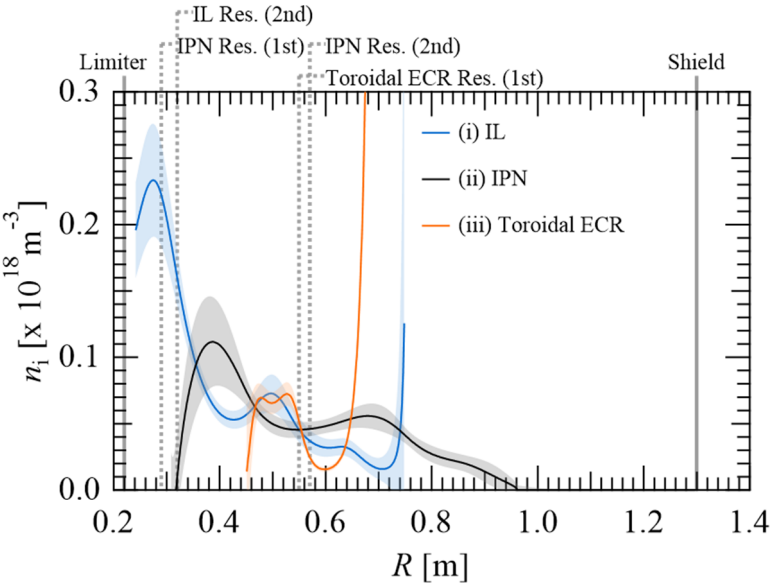

Fig. 5-17. Radial profiles of C^{2+} ion density n_i. Solid vertical lines show the positions of the inboard limiter (Limiter) and radiation shield (Shield). Dotted vertical lines show the position of the resonance layer for 28 GHz ECH in discharge (i) (IL Res. (2nd)), that for 8.2 GHz ECH in discharge (ii) (IPN Res. (1st) and (2nd)), and that for 8.2 GHz ECH in discharge (iii) (Toroidal ECR Res. (1st)).

5.6 Conclusion

For the understanding of impurity transport, the radial profiles of impurity ion flow were measured for three types of discharge in QUEST, used to experimentally simulate different regions of edge plasma. Multiple viewing chords were aligned at the midplane, and the emission of C^{2+} ions was measured by a spectroscopic system. The velocity of C^{2+} ions was evaluated from the Doppler shift of the measured CIII line spectra. For the accurate evaluation of the velocity, emission lines from the reference lamp were measured immediately after every discharge, and the wavelength shift caused by the change in room temperature was subtracted. An inversion method was developed and applied to the chord-integrated spectra measured for the three types of discharge, (i) the inboard limiter configuration (IL), (ii) the inboard poloidal null configuration (IPN), (iii) the open field configuration (toroidal ECR), and the radial profiles of ε, V_φ, and T_i were derived. Abel inversion and the shell model were applied to derive the ε profile and the V_φ and T_i profiles, respectively. The combination of these two inversion methods enabled the profiles to be estimated from spectra with a low signal-to-noise ratio. The C^{2+} ion density profile was also estimated using a coronal model. The errors due to the inversion method were verified using synthesized data, and the error of V_φ was less than 8.1 km/s. The profiles of V_φ measured in discharge (i) are in the co-I_p direction, in agreement with the direction of Pfirsch–Schlüter flow. In discharge (ii), the direction of V_φ reverses at the X-point owing to the electric field on the inboard side of the X-point. The reversal of V_φ was also observed at the resonance layer in discharge (iii), which is consistent with the reversal of the radial electric field at the resonance layer. These results show the applicability of the method to the three regions of the edge plasmas in a larger device.

6 Conclusion

The emission spectroscopy of hydrogen molecules and impurity ions in tokamak edge plasmas was conducted to evaluate the surface temperature of plasma-facing walls and the impurity ion flow, respectively, to control impurity generation and transport.

Chapter 3 depicted the construction of the model used to evaluate the increase in rotational temperature for the ground-state hydrogen molecules. Previous research of plasma-facing surface thermometry using the rotational temperature of hydrogen molecules was introduced, and the mechanism of surface thermometry was described. The translational, vibrational, and rotational temperatures of hydrogen molecules were defined, and the rovibrational population distributions previously measured in low-pressure plasmas are shown. The dynamics of hydrogen molecules near the plasma-facing walls were described, and the three factors that can affect the rotational temperature were explained: surface temperature, excitation due to recombination on the surface, and collisional-radiative processes in the plasma. Among these factors, collisional-radiative processes that can be affect the rotational temperature were explained. The increase in rotational temperature was modeled considering the processes. The calculation code of the model was benchmarked by using conditions of thermal equilibrium and by comparison with the results derived from a coronal model developed in earlier research. The effects of electron and proton densities and temperatures, distance from the surface, and surface temperature on the rotational temperature were individually evaluated in a uniform plasma. The results showed the high sensitivity of the rotational temperature to the densities and the distance from the surface. The effects of the rotational, rovibrational, and rovibronic transitions were also evaluated. The results suggest that the rovibrational and rovibronic transitions only affect the rotational temperature when the densities are higher than 10^{19} m^{-3}.

Chapter 4 described the thermometry of plasma-facing surfaces using the rotational temperature of hydrogen molecules in three tokamaks. The rotational temperature was measured by the spectroscopic approach in three tokamaks: QUEST (Q-shu University Experiment with Steady-State Spherical Tokamak), LTX-β (Lithium Tokamak Experiment Beta), and DIII-D (Doublet III-D). For the three tokamaks, the measured plasma discharges, the distributions of electron density and

temperature, and the surface temperatures measured with a conventional method were described. The spectroscopic systems used for the measurement of hydrogen molecular emission line spectra were shown with their wavelength and intensity calibrations and the evaluation of the instrumental functions. The rotational temperature of the ground-state hydrogen molecules $T_{\mathrm{rot}}^{X v=0}$ was evaluated from the measured spectra using the coronal model. The measurements in the three tokamaks show that the increases in $T_{\mathrm{rot}}^{X v=0}$ match the calculated increases due to collisional-radiative processes within a factor of three. In QUEST and LTX-β, the measured $T_{\mathrm{rot}}^{X v=0}$ increased with T_{wall} and was higher than the calculation results by ≈ 450 K. The latter implies the little dependence of $T_{\mathrm{rot}}^{X v=0}$ on the surface material, and this can be confirmed by improving the evaluation of the increase due to the collisional-radiative processes in DIII-D.

Chapter 5 showed the measurement of the C^{2+} ion flow in the edge plasmas by optical emission spectroscopy. The flow distributions and their driving mechanism were explained for the three regions of the edge plasmas: SOL, X-point, and divertor leg. The factors affecting the spectral profiles of C^{2+} emission lines were described. The ion velocity was evaluated from the Doppler shift. The three regions of the edge plasmas were simulated using the three types of plasma generated in QUEST, and the magnetic equilibria and profiles of electron density and temperature were illustrated. The spectroscopic system used for the measurements of C^{2+} emission line spectra was explained with its wavelength and intensity calibrations and the evaluation of the instrumental functions. Emission lines from the reference lamp were measured immediately after every discharge, which reduced the error of the velocity by 0.9 km/s. An inversion method was developed to derive the radial profiles of emissivity, toroidal ion velocity, and ion temperature. Abel inversion and the shell model were applied to derive the emissivity profile and the velocity and temperature profiles, respectively. The combination of these two inversion methods enabled to estimate the profiles from spectra with a low signal-to-noise ratio. The radial profiles of ion density were also evaluated from the emissivity profiles using the coronal model. The structure in the flow was derived for the three simulated regions of the edge plasma, which suggests the applicability of the method for the edge plasmas in a larger device.

Reference

[1] International Energy Agency (IEA), "Key World Energy Statistics 2021" (2021). https://www.iea.org/reports/key-world-energy-statistics-2021.

[2] United Nations Development Programme (UNDP), "Sustainable Development Goals". https://www.undp.org/sustainable-development-goals.

[3] ITER Organization, "ITER - the way to new energy". https://www.iter.org/ (Accessed 7 Dec. 2021).

[4] International Atomic Energy Agency (IAEA), "What is Fusion, and Why Is It So Difficult to Achieve? | IAEA". https://www.iaea.org/fusion-energy/what-is-fusion-and-why-is-it-so-difficult-to-achieve.

[5] National Institutes for Quantum Science and Technology (QST), "Japanese Domestic Agency of Experimental Fusion Reactor ITER, QST | What is ITER?". https://www.fusion.qst.go.jp/ITER/iter/page1_7.html (Accessed 12 Jan. 2022).

[6] A. C. C. Sips, for the Steady State Operation and the Transport Physics topical groups of the International Tokamak Physics Activity, *Plasma Phys. Control. Fusion,* **47**, A19 (2005). doi:10.1088/0741-3335/47/5a/003.

[7] A. S. Kukushkin, H. D. Pacher, G. W. Pacher, G. Janeschitz, D. Coster, A. Loarte and D. Reiter, *Nucl. Fusion,* **43**, 716 (2003). doi:10.1088/0029-5515/43/8/312.

[8] J. P. Gunn, S. Carpentier-chouchana, F. Escourbiac, T. Hirai, S. Panayotis, R. A. Pitts, Y. Corre, R. Dejarnac, M. Firdaouss, M. Kočan *et al.*, *Nucl. Fusion,* **57**, 046025 (2017). doi:10.1088/1741-4326/aa5e2a.

[9] ITER Organization, "Divertor | Far more than a fancy ashtray", 30 Mar. 2020. https://www.iter.org/newsline/-/3422 (Accessed 7 Dec. 2021).

[10] R. A. Pitts, S. Bardin, B. Bazylev, M. A. van den Berg, P. Bunting, S. Carpentier-chouchana, J. W. Coenen, Y. Corre, R. Dejarnac, F. Escourbiac *et al.*, *Nucl. Mater. Energy,* **12**, 60 (2017). doi:10.1016/j.nme.2017.03.005.

[11] R. A. Pitts, A. Kukushkin, A. Loarte, A. Martin, M. Merola, C. E. Kessel, V. Komarov and M. Shimada, *Phys. Scr.,* **T138**, 014001 (2009). doi:10.1088/0031-8949/2009/t138/014001.

[12] ITER Organization, "Blanket". https://www.iter.org/mach/blanket (Accessed 7 Dec. 2021).

[13] R. A. Pitts, S. Carpentier, F. Escourbiac, T. Hirai, V. Komarov, S. Lisgo, A. S. Kukushkin, A. Loarte, M. Merola, A. Sashala Naik *et al.*, *J. Nucl. Mater.,* **438**, S48 (2013). doi:10.1016/j.jnucmat.2013.01.008.

[14] G. Janeschitz, ITER JCT and HTs, *J. Nucl. Mater.,* Vols. 290-293, 1 (2001). doi:10.1016/S0022-3115(00)00623-1.

[15] O. E. Garcia, *Plasma Fusion Res.,* **4**, 019 (2009). doi:10.1585/pfr.4.019.

[16] C. E. Carlston, A. Comeaux and P. Mahadevan, *Phys. Rev.,* **138**, A759 (1965). doi:10.1103/PhysRev.138.A759.

[17] Y. Wu, W. Ni, H. Fan, L. Liu, Q. Yang, B. Cao and D. Liu, *J. Nucl. Mater.,* **470**, 164 (2016). doi:10.1016/j.jnucmat.2015.12.022.

[18] G. De Temmerman, T. Hirai and R. A. Pitts, *Plasma Phys. Control. Fusion,* **60**, 044018 (2018). doi:10.1088/1361-6587/aaaf62.

[19] J. P. Allain, M. D. Coventry and D. N. Ruzic, *Phys. Rev. B,* **76**, 205434 (2007). doi:10.1103/PhysRevB.76.205434.

[20] C. García-Rosales, *J. Nucl. Mater.,* **211**, 202 (1994). doi:10.1016/0022-3115(94)90348-4.

[21] A. E. Costley, T. Sugie, G. Vayakis and C. I. Walker, *Fusion Eng. Des.,* **74**, 109 (2005). doi:10.1016/j.fusengdes.2005.08.026.

[22] NIST, "Atomic Spectra Database". https://www.nist.gov/pml/atomic-spectra-database.

[23] H. Nakashima and H. Nakatsuji, *J. Chem. Phys.,* **149**, 244116 (2018). doi:10.1063/1.5060659.

[24] U. Fantz and D. Wünderlich, *At. Data Nucl. Data Tables,* **92**, 853 (2006). doi:10.1016/j.adt.2006.05.001.

[25] L. Wolniewicz, *J. Chem. Phys.,* **99**, 1851 (1993). doi:10.1063/1.465303.

[26] T. E. Sharp, *At. Data Nucl. Data Tables,* **2**, 119 (1970). doi:10.1016/S0092-640X(70)80007-9.

[27] V. Riccardo, W. Fundamenski and G. F. Matthews, *Plasma Phys. Control. Fusion,* **43**, 881 (2001). doi:10.1088/0741-3335/43/7/304.

[28] T. Ushiki, R. Imazawa, H. Murakami, K. Shimizu, T. Sugie and T. Hatae, *Fusion Eng. Des.,* **168**, 112665 (2021). doi:10.1016/j.fusengdes.2021.112665.

[29] L. del Campo, R. B. Pérez-Sáez and M. J. Tello, *Corros. Sci.,* **50**, 194 (2008). doi:10.1016/j.corsci.2007.05.029.

[30] S. Brezinsek, P. Mertens, A. Pospieszczyk, G. Sergienko and P. T. Greenland, *Contrib. Plasma Phys.,* **42**, 668 (2002). doi:10.1002/1521-3986(200211)42:6/7<668::AID-CTPP668>3.0.CO;2-Z.

[31] E. M. Hollmann, S. Brezinsek, N. H. Brooks, M. Groth, A. G. Mclean, A. Y. Pigarov and D. L. Rudakov, *Plasma Phys. Control. Fusion,* **48**, 1165 (2006). doi:10.1088/0741-3335/48/8/009.

[32] K. P. Huber and G. Herzbarg, *Molecular Spectra and Molecular Structure: IV. Constants of diatomic molecules* (Van Nostrand Reinhold Company, 1979), p. x.

[33] NIST, "NIST Chemistry WebBook". https://webbook.nist.gov/chemistry/.

[34] S. Briefi, D. Rauner and U. Fantz, *J. Quant. Spectrosc. Radiat. Transfer,* **187**, 135 (2017). doi:10.1016/j.jqsrt.2016.09.015.

[35] R. A. Causey, *J. Nucl. Mater.,* **300**, 91 (2002). doi:10.1016/S0022-3115(01)00732-2.

[36] S. Markelj and I. Čadež, *J. Chem. Phys.,* **134**, 124707 (2011). doi:10.1063/1.3569562.

[37] D. Wünderlich, M. Giacomin, R. Ritz and U. Fantz, *J. Quant. Spectrosc. Radiat. Transfer,* **240**, 106695 (2020). doi:10.1016/j.jqsrt.2019.106695.

[38] K. Sawada and M. Goto, *Atoms,* **4**, 29 (2016). doi:10.3390/atoms4040029.

[39] International Atomic Energy Agency (IAEA), "IAEA AMDIS ALADDIN Database". https://www-amdis.iaea.org/ALADDIN/collision.html (Accessed 5 Jan. 2022).

[40] M. A. Morrison, R. Crompton, B. C. Saha and Z. Lj. Petrovic, *Aust. J. Phys.,* **40**, 239 (1987). doi:10.1071/PH870239.

[41] N. F. Lane and S. Geltman, *Phys. Rev.,* **160**, 53 (1967). doi:10.1103/PhysRev.160.53.

[42] M. Čížek, J. Horáček and W. Domcke, *J. Phys. B,* **31**, 2571 (1998). doi:10.1088/0953-4075/31/11/018.

[43] T. Fujimoto, *Plasma Spectroscopy* (Clarendon Press, 2004), pp. 56-58. doi:10.1093/acprof:oso/9780198530282.001.0001.

[44] A. V. Phelps, *J. Phys. Chem. Ref. Data,* **19**, 653 (1990). doi:10.1063/1.555858.

[45] J. Horáček, M. Čížek, K. Houfek and P. Kolorenč, *Phys. Rev. A,* **73**, 022701 (2006). doi:10.1103/PhysRevA.73.022701.

[46] R. K. Janev, D. Reiter and U. Samm, "Collision Processes in Low-Temperature Hydrogen Plasmas" (2003). http://www.eirene.de/report_4105.pdf.

[47] Observatoire de Paris, "Atomic and Molecular Data, l'Observatoire de Paris". https://molat.obspm.fr/.

[48] J. K. G. Watson, *J. Mol. Spectrosc.,* **252**, 5 (2008). doi:10.1016/j.jms.2008.04.014.

[49] E. E. Whiting, A. Schadee, J. B. Tatum, J. T. Hougen and R. W. Nicholls, *J. Mol. Spectrosc.,* **80**, 249 (1980). doi:10.1016/0022-2852(80)90137-X.

[50] K. Hanada, N. Yoshida, M. Hasegawa, A. Hatayama, K. Okamoto, I. Takagi, T. Hirata, Y. Oya, M. Miyamoto, M. Oya *et al.*, *Nucl. Fusion,* **59**, 076007 (2019). doi:10.1088/1741-4326/ab1858.

[51] L. F. Berzak, "Plasma Start-up in a Spherical Tokamak with Close-fitting Conducting Walls," PhD thesis, 2010.

[52] J. L. Luxon, *Nucl. Fusion,* **42**, 614 (2002). doi:10.1088/0029-5515/42/5/313.

[53] General Atomics, "diii-d:home [MFE: DIII-D and Theory]". https://fusion.gat.com/global/diii-d/home (Accessed 13 Jan 2022).

[54] C. M. Samuell, S. L. Allen, W. H. Meyer, R. C. Isler, A. Briesemeister, R. S. Wilcox, C. J. Lasnier, A. G. Mclean and J. Howard, *Rev. Sci. Instrum.,* **89**, 093502 (2018). doi:10.1063/1.5039367.

[55] T. Maekawa, T. Yoshinaga, M. Uchida, F. Watanabe and H. Tanaka, *Nucl. Fusion,* **52**, 083008 (2012). doi:10.1088/0029-5515/52/8/083008.

[56] T. Yamaguchi, A. Ejiri, J. Hiratsuka, Y. Takase, Y. Nagashima, O. Watanabe, T. Sakamoto, T. Ohsako, B. I. An, H. Kurashina *et al.*, *Plasma Fusion Res.,* **5**, S2092 (2010). doi:10.1585/pfr.5.S2092.

[57] M. Groth, E. M. Hollmann, A. E. Jaervinen, A. W. Leonard, A. G. Mclean, C. M. Samuell, D. Reiter, S. L. Allen, P. Boerner, S. Brezinsek *et al.*, *Nucl. Mater. Energy,* **19**, 211 (2019). doi:10.1016/j.nme.2019.02.035.

[58] C. F. Sang, P. C. Stangeby, H. Y. Guo, A. W. Leonard, B. Covele, L. L. Lao, A. L. Moser and D. M. Thomas, *Plasma Phys. Control. Fusion,* **59**, 025009 (2016). doi:10.1088/1361-6587/59/2/025009.

[59] R. E. Bell, *Rev. Sci. Instrum.,* **85**, 11E404 (2014). doi:10.1063/1.4884612.

[60] N. H. Brooks, A. Howald, K. Klepper and P. West, *Rev. Sci. Instrum.,* **63**, 5167 (1992). doi:10.1063/1.1143469.

[61] H. M. Crosswhite, *Hydrogen Molecule Wavelength Tables of Gerhard Heinrich Dieke*, second ed., (Wiley-Interscience, 1968).

[62] B. P. Larnov and D. Otorbaev, *Sov. Tech. Phys. Lett.,* **4**, 574 (1978).

[63] H. R. Griem, *Plasma Spectroscopy* (McGraw-Hill Book Company, 1964), pp. 74, 91, 95–100, 363–421.

[64] H. R. Griem, *Spectral Line Broadening by Plasmas* (Academic Press, 1974), pp. 214, 279.

[65] C. H. Reinsch, *Numer. Math,* **10**, 17 (1967).

[66] Y. Itikawa, S. Hara, T. Kato, S. Nakazaki, M. S. Pindzola and D. H. Crandall, *At. Data Nucl. Data Tables,* **33**, 149 (1985). doi:10.1016/0092-640X(85)90025-7.

List of Publication

International Journal Papers

1) Nao Yoneda, Taiichi Shikama, Hideki Zushi, Kazuaki Hanada, Akinobu Fujikawa, Takumi Onchi, Kengoh Kuroda, Kuniaki Nii, Masahiro Hasuo *et al.*, "Spectroscopic Measurements of Impurity Ion Toroidal and Poloidal Flow Velocities and Their Dependence on Vertical Magnetic Field in QUEST Toroidal ECR Plasmas", *Plasma Fusion Res.* **13**, 3402087 (2018).
2) N. Yoneda, T. Shikama, K. Hanada, S. Mori, T. Onchi, K. Kuroda, M. Hasuo, A. Ejiri, K. Matsuzaki, Y. Osawa *et al.*, "Toroidal flow measurements of impurity ions in QUEST ECH plasmas using multiple viewing chords emission spectroscopy", *Nucl. Mater. Energy* **26**, 100905 (2021).

International Conferences

1) N. Yoneda, T. Shikama, K. Hanada, S. Mori, T. Onchi, K. Kuroda, M. Hasuo, A. Ejiri, K. Matsuzaki, Y. Osawa *et al.*, "Toroidal Flow Measurements of Impurity Ions in QUEST ECH Plasmas using Multiple Viewing Chords Emission Spectroscopy", The 24th International Conference on Plasma Surface Interactions in Controlled Fusion Devices (PSI-24), Jan. 25–29, 2020, Korea (online), FP4-023(E).
2) Nao Yoneda, Filippo Scotti, Ronald Bell, Taiichi Shikama, Paul Hughes, Anurag Maan, Vlad Soukhanovskii, Dennis Boyle, Richard Majeski, Kazuaki Hanada, Masayuki Ono, Masahiro Hasuo, "Measurement of Hydrogen Molecular Rotational Temperatures in LTX-β for the Thermometry of Plasma-Facing Lithium Surfaces", 62nd Annual Meeting of the APS Division of Plasma Physics (APS-DPP62), the USA (online), Nov. 9–13, 2020, ZP06.00022.

Domestic Conferences

1) 米田奈生，四竈泰一，花田和明，森暁，恩地拓己，黒田賢剛，江尻晶，川又裕也，坂本将，松崎亨平 他，「QUEST 内側ポロイダルヌル配位のスクレイプオフ層における高速イオン流れの観測」, 日本物理学会 2019 年秋季大会, 岐阜大学, 2020 年 9 月 10–13 日, 11pK21-9.
2) 米田奈生，四竈泰一，花田和明，森暁，井口拓己，恩地拓己，蓮尾昌裕，出射浩，井戸毅，中村一男 他，「QUEST 内側ポロイダルヌル配位における不純物イオン発光線サブピークの起源についての検討」, 日本物理学会 第 75 回年次大会, 2020 年 3 月 16–19 日, 16pD11-5.
3) 米田奈生，F. Scotti，R. E. Bell，四竈泰一，P. E. Hughes，A. Maan，V. A. Soukhanovskii, D. P. Boyle，R. P. Majeski，花田和明，小野雅之，蓮尾昌裕，「LTX-β におけるリチウム壁表面温度推定のための水素分子回転温度計測」，日本物理学会 2020 年秋季大会，オンライン，2020 年 9 月 8–11 日，8pB2-11.
4) 米田奈生，四竈泰一，F. Scotti，花田和明，井口拓己，出射浩，恩地拓己，江尻晶，井戸毅，河野香 他，「QUEST における水素分子 $d^3\Pi$ 準位回転温度を利用したタングステン表面温度計測」，日本物理学会 第 76 回年次大会，オンライン，2021 年 3 月 12–15 日, 12pB2-6.
5) 米田奈生，四竈泰一，F. Scotti，花田和明，R. E. Bell，A. Maan，P. E. Hughes，井口拓己，出射浩，恩地拓己 他，「プラズマ対向壁近傍の水素分子 $d^3\Pi$ 準位回転温度に影響を与える素過程の検討」，日本物理学会 2021 年秋季大会，オンライン，2020 年 9 月 20–23 日，23pB2-6.